Subsurface Charge Accumulation Imaging of the Quantum Hall Liquid

by

Paul Ioannis Glicofridis

Submitted to the Department of Physics
in partial fulfillment of the requirements for the degree of

Doctor of Philosophy

at the

MASSACHUSETTS INSTITUTE OF TECHNOLOGY

September 2001

Author .....
Department of Physics
September 6, 2001

Certified by .....
Raymond C. Ashoori
Associate Professor
Thesis Supervisor

Accepted by .....
Thomas C. Greytak
Professor, Associate Department Head for Education

Subsurface Charge Accumulation Imaging of the Quantum Hall Liquid

by

Paul Ioannis Glicofridis

Submitted to the Department of Physics
on September 6, 2001, in partial fulfillment of the
requirements for the degree of
Doctor of Philosophy

Abstract

We describe results obtained by a novel scanning technique, called Subsurface Charge Accumulation (SCA) Imaging, that enables the direct imaging of electronic systems buried inside semiconductor materials. Using SCA Imaging, we image and measure properties of a two-dimensional electron system (2DES) in a GaAs/AlGaAs heterostructure, in the regime of the integer quantum Hall effect.

We observe general charging features in a plain 2DES near quantum Hall integer filling factors. We proceed by imaging low compressibility strips in the presence of an artificially created density gradient in the 2DES. We study them in detail at Landau level filling factors $\nu = 2, 4$. The strips appear significantly wider than predicted by theory and we account for the discrepancy by presenting a model that considers the disorder-induced nonzero density of states in the cyclotron gap. We also measure the charging properties of incompressible strips that form parallel to the edges of a metal gate deposited on the surface of our sample. An RC model considering charging of the 2DES across the strip, closely fits the data. This allows us to determine the longitudinal resistivity of the incompressible part of the edge state that runs parallel to the gate, for a range of filling factors. Surprisingly, the strip becomes more resistive in regions of high electronic density gradient, where its width is expected to decrease.

By sensing charge from the motion of single electrons inside the 2DES we produce a topographic map of the random potential inside the integer quantum Hall liquid. We achieve this by creating a mobile quantum dot inside the 2DES. By scanning the dot, single electrons enter or leave it, in response to the local potential. Detection of this motion leads to the creation of a potential contour map. We find that the 2D electron screening of the random potential induced by external impurities, changes little between quantum Hall plateaus and within each plateau.

We finally present preliminary results from a 2DES sample with a built-in backgate. The backgate enables us to deplete the 2DES and perform measurements in the regime of low electronic densities.

Thesis Supervisor: Raymond C. Ashoori
Title: Associate Professor

Acknowledgments

This thesis represents the culmination of several years of work, in what came to be one of the most exciting projects in our research group: scanning capacitance microscopy of quantum Hall liquids.

First of all, I would like to extend my thanks to my thesis and research advisor, Ray Ashoori. Apart from providing the material means and the infrastructure necessary for conducting our experimental work, he has been a source of unlimited support and encouragement throughout my years as a graduate student. Ray's active presence in the lab coupled with his desire to teach his students, and me personally, numerous essential experimental skills, acted as a catalyst that led to the success of the project. At the same time he taught me the importance of trying new approaches and putting my ideas to practice even if the outcome is not always certain. Ray was right. Despite the occasional problems and frustrations related to the experiment, it turned out that the reward stemming from our results, was enough to outweigh all the difficult times that are bound to be present in novel research work. Ray's hard work and original ideas about exciting research projects, remain a source of inspiration for all members of our group.

It was a great pleasure working closely with Gleb Finkelstein during the time he was here at MIT. Gleb contributed significantly to the success of this thesis project, and I wish to thank him for his help and input that continues to this day. The discussions I had with Gleb about physics, experimental techniques, as well as subjects of more general interest, have greatly enriched my knowledge. His physical arguments and explanations being particularly clear, it is not surprising that some of the figures in this thesis are based on them.

I would also like to acknowledge the help and contribution of Stuart Tessmer who designed the microscope and taught me a great deal about scanning microscopy techniques and their principles. Without this fundamental knowledge, it would have been difficult to uncover the full potential of the instrument. Prof. Melloch and Prof. Shayegan contributed in a fundamental manner to this project by providing the

semiconductor samples used in our investigations.

I am grateful to Prof. Leonid Levitov for his interest in our experimental work as well as for the time he devoted in helping us explain and better understand several aspects of our results.

I had the pleasure to be a part of a research group where both previous and current members have shaped a very friendly environment to work in. Ho-Bun Chan, Misha Brodsky, David Berman, Nikolai Zhitenev, Predrag Nikolic, Dima Pouchine, Gary Steele, Oliver Dial and Aleem Siddiqui were an invaluable source of knowledge in our laboratory. I would particularly like to thank Ho-Bun Chan who provided me with a lot of help and guidance during my first year as a graduate student. Gary Steele and Oliver Dial took the responsibility of our local computer network and did an excellent job in maintaining and constantly improving it. Steven Moss, member of the spin polarized hydrogen group, was responsible for running the helium liquefier with me. He contributed significantly to this task by devoting time and assuming significant responsibilities. His office being opposite to my lab, I had the opportunity to discuss with him about a variety of topics that included, but were not limited to our research interests. I thank him for his good company.

My family has always been a source of help, support and optimism. I thank my parents and my brother in Greece for their love and continuous moral support during the years of my studies.

ἄγει εἰς φῶς τήν ἀλήθεια ὁ χρόνος

time brings truth to light

Aristotle, 4th century B.C.

Contents

List of Figures

List of Tables

Chapter 1

Introduction

The behavior of a large collection of particles in a macroscopic system is of fundamental importance in physics. Advances in semiconductor materials science and devices in the recent decades, have lead to the realization of one of the simplest many particle systems that one can imagine, the 2-dimensional electron gas (2DEG). Despite its apparent simplicity, this system opened Pandora's box for condensed matter physics and generated a vast wealth of unexpected and fascinating results.

The discovery of the integer quantum Hall effect in 1980 and of the fractional quantum Hall effect in 1982 are considered to be among the most important developments in physics in the second half of the 20th century. In turn, systems of reduced dimensionality (such as the 2DEG) in which these effects were observed, have proven to be ideal for the study of fundamental electron interactions.

Until recently, transport experiments measuring the electrical properties of 2-dimensional electron gases, were the primary sources of information for systems of freely moving electrons. In this thesis we present results that we obtained using a novel measurement technique, called Subsurface Charge Accumulation (SCA) Imaging. The technique was developed in our laboratory and enables direct imaging of electronic systems underneath the surface of semiconductor materials. SCA imaging has been successful in probing a 2DEG and measuring its properties in the regime of the integer quantum Hall effect. In addition, we applied it to obtain for the first time, high resolution images of the quantum Hall electron liquid and the underlying disorder

potential.

The thesis is organized as follows. In Chapter 2 we describe in detail the experimental technique of SCA imaging and its different modes of operation. We also present sample results that prove its ability to probe mesoscopic systems in cryogenic temperatures and high magnetic fields. Chapter 3 contains some of our earliest data on imaging the quantum Hall liquid. Chapter 4 presents measurements of the width and compressibility of the so-called incompressible strips. These strips constitute an important element in the edge state picture that describes key properties of the integer quantum Hall effect. In Chapter 5 we study how a 2DEG charges through an incompressible strip. With the help of an RC charging model we extract the strip resistance for a number of integer quantum Hall filling factors. Chapter 6 moves in a different direction and demonstrates the use of a mobile quantum dot in order to obtain a topographic map of the random potential as seen by the electrons inside the 2DEG. Chapter 7 concludes this work by presenting preliminary results in the low electronic density regime and by examining future research prospects.

1.1 Two-Dimensional Electron Systems

The highest mobility two-dimensional electronic systems are formed by quantum confinement at the interface between GaAs and $Al_xGa_{1-x}As$. The corresponding samples and devices are known as heterostructures - semiconductors composed by at least two different materials. $Al_xGa_{1-x}As$ is a semiconducting alloy with a lattice constant very similar to that of GaAs when $x \approx 0.3$. The technique of molecular beam epitaxy (MBE) thus allows the production of GaAs/AlGaAs junctions that are nearly perfectly matched at their interface.

Moreover, one has direct control over the behaviour of electrons and holes through band engineering and modulation doping. The resulting structures contain quantum wells with the desired properties (e.g. shape, depth) for electron confinement. In addition, dopant atoms can be physically separated from the active sample region where the mobile charges are located. Scattering between carriers and dopants is

significantly reduced and the mobility of the sample is dramatically increased. A 2DEG is created at the interface between n-AlGaAs and GaAs by electrons that fall into the quantum well that is formed at the heterojunction. The electronic energy level spacing is of the order of 10^2 Kelvin, which is much greater than the cryogenic temperatures ($\sim$ 1 Kelvin) required for QHE measurements. As a result, electrons all occupy the lowest sub-band in the well but are free to move in the x-y plane of the crystal. Consequently, the well may have finite width ($\approx$ 10 nm) but the resulting system is 2-dimensional.

A treatise on two-dimensional systems can be found in [1]. Its emphasis is on Si MOSFET 2D systems which are now outdated, but the basic theory is still valid.

1.2 The Quantum Hall Effect

The integer quantum Hall effect was discovered by von Klitzing, Dorda and Pepper in 1980. Its experimental manifestation is the quantization of the Hall conductance σ_{xy}, accompanied by vanishing dissipation ($\sigma_{xx} \to 0$), in a 2-dimensional electron system in the presence of a strong magnetic field. Figure 1-1 demonstrates these properties with measurements taken from one of our 2DEG samples at a temperature of 350 mK. We will return to the study of this particular sample in Chapter 3. Going back to the figure, the quantization of σ_{xy} (or equivalently of the Hall resistance R_H defined as σ_{xy}^{-1}) manifests itself as a series of plateaus that occur precisely when:

$$\sigma_{xy} = \nu \frac{e^2}{h} \tag{1.1}$$

Here, e is the electron charge, h is Planck's constant and the quantum number ν is a positive integer. This result has been shown to be accurate to at least one part in 10^8 and it is independent of sample specific properties, such as physical dimensions, sample material or degree of inhomogeneity. The IQHE is thus a universal and fundamental physical phenomenon.

Most of the features of the IQHE can be described by considering free electrons in a 2-dimensional plane subjected to a perpendicular magnetic field. It is easy then to

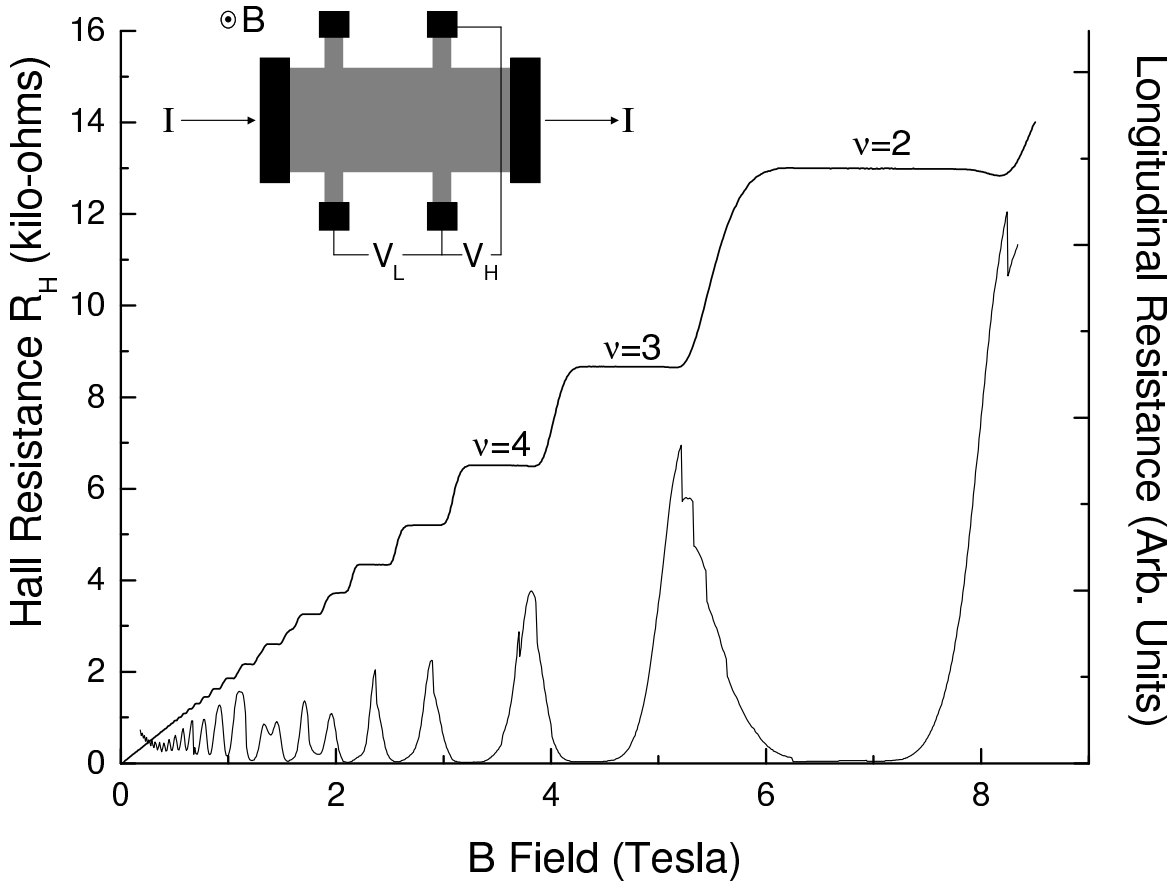

Figure 1-1: Integer quantum Hall transport data showing the plateau regions of quantized transverse (Hall) resistance R_H. The sample used is a GaAs/AlGaAs heterostructure, cooled to a temperature of 350 mK. When the Hall resistance is flat, the longitudinal resistance drops to practically zero, indicating the absence of dissipation in the system. The plateau centered around 7 Tesla corresponds to integer filling factor $\nu = 2$. Notice that the transition from one plateau to the next is smeared out due to the finite temperature. Inset: Schematic of the measurement setup. Black regions correspond to ohmic contacts to the 2DEG (grey region). The longitudinal and Hall voltage, V_L and V_H respectively, are measured while current I flows through the 2DEG in the presence of a perpendicular magnetic field.

show that in the absence of scattering, the off-diagonal elements of the conductivity tensor are given by:

$$\sigma_{xy} = \frac{nec}{B} \tag{1.2}$$

Under these conditions, the continuous density of states for free electrons is replaced by a series of highly degenerate and equally spaced δ-functions (Figure 1.4(a)). These resulting energy levels are highly degenerate and are called Landau levels. Both the degeneracy per unit area N and the energy spacing ΔE of these levels, change linearly with field. More precisely, one has that

$$\Delta E = \hbar\omega_c \tag{1.3}$$

where $\omega_c = \frac{eB}{mc}$ is the cyclotron frequency, and

$$N = \frac{eB}{hc} \tag{1.4}$$

With n denoting the density of the 2DEG, the quantity $\nu = \frac{n}{N}$ is known as the Landau level filling factor. It follows that if the Fermi energy resides between the ν and $\nu + 1$ Landau level, then the νth level is completely full, with ν being an exact integer i. As a result, using Equation 1.2, we obtain the quantized conductivity values that characterize the quantum Hall plateaus.

The discussion so far has assumed that there is no disorder present in the system. However, it turns out that impurities in a real electron system play a crucial role in the explanation of the QHE. Disorder, resulting from imperfections in the 2DEG, effectively creates a new set of states that lie in-between the exact Landau levels described above. These states are localized and thus unable to carry current at zero temperature. As long as the Fermi energy lies within a band of localized states (also known as a mobility gap), the occupation of the extended states (the ones responsible for electronic transport) does not change. As a result, the conductance σ_{xy} remains constant and a plateau at the value given by Equation 1.1, is observed for a range

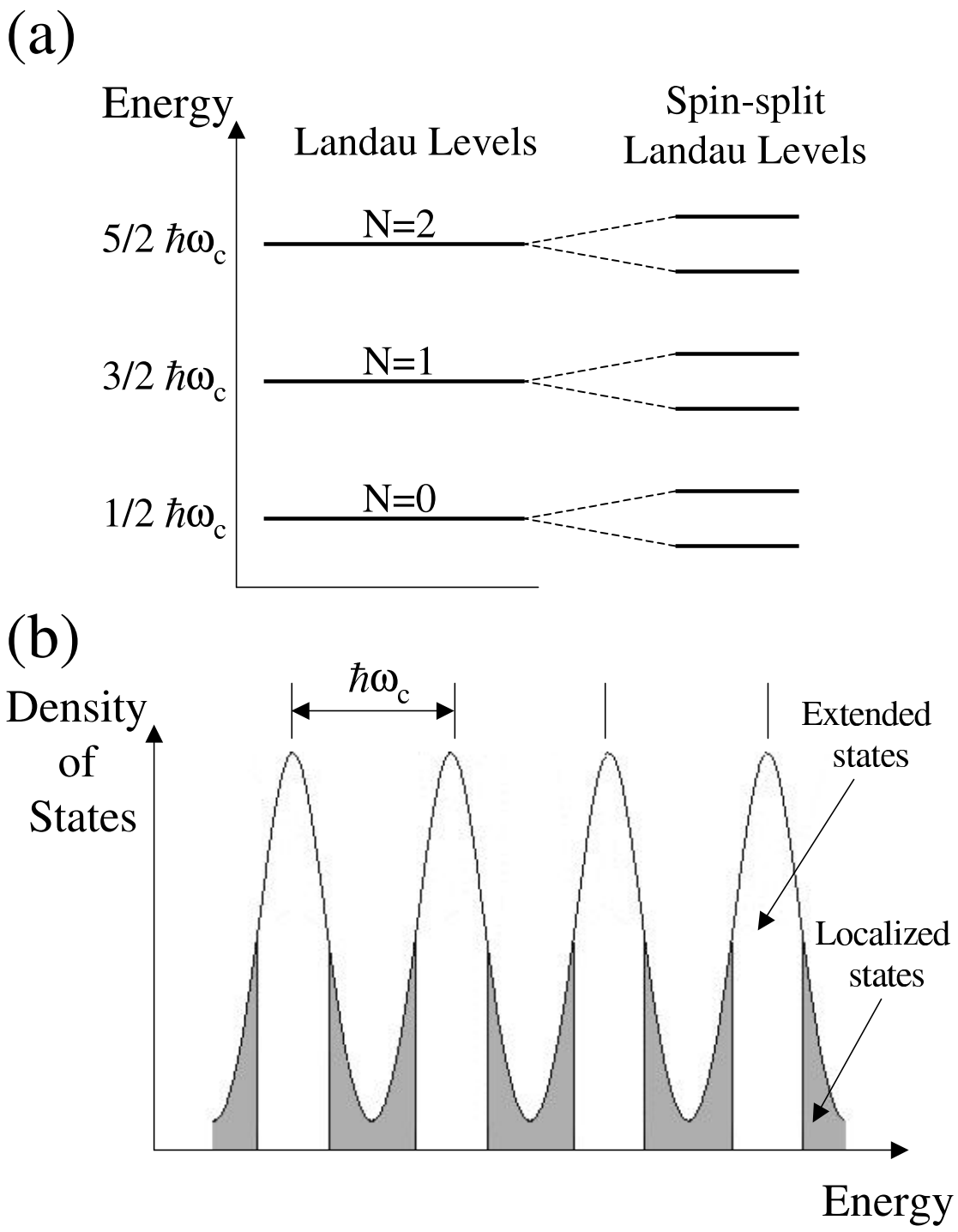

Figure 1-2: (a) The density of states for non-interacting 2D electrons in the presence of a perpendicular magnetic field consists of a series of equally spaced delta-functions, called Landau levels. At high magnetic fields, spin (Zeeman) splitting of the electronic levels becomes important and needs to be taken into account. (b) Landau levels broaden in the presence of disorder. Note that this particular illustration neglects spin splitting.

of magnetic fields at the corresponding Landau level filling factor. A powerful gauge argument on the role of localized states has been put forward by Laughlin and refined by Halperin. It can be found in [2, 3]. In Chapter 6 we shall see how the technique of SCA imaging can be used to map the background impurity potential that effectively gives rise to these states.

The IQHE was only the first surprise for condense matter physicists. Two years after its discovery, fractional Hall plateaus were observed by Tsui, Stormer and Gossard [4]. These plateaus indicated that there is a family of excitation gaps that the simple single electron quantum theory could not account for. After considerable theoretical and experimental effort, we know today that the fractional QHE arises from the correlated behavior of electrons and the Coulomb interaction between them. In samples of high purity subjected to strong magnetic fields very near absolute zero, the 2DEG condenses into a fluid whose elementary excitations carry a fraction of an electron charge [5].

The above discussion is just a brief summary of some of the key issues relating to the QHE. A more thorough explanation is beyond our scope, but reviews covering both the integer and fractional case can be found in References [6] and [7].

We shall now proceed to describe our technique that allows one to literally look inside the fascinating world of the QHE.

Chapter 2

Charge Accumulation Imaging Microscopy

The invention of the scanning tunneling microscope (STM) in 1982 by Binnig and Rohrer [8, 9, 10, 11] has had a tremendous impact on the study of materials surfaces. The instrument evolved rapidly and has become a powerful tool for many disciplines ranging from physics to biology and chemistry. Tunneling microscopy and its extension, atomic force microscopy (AFM), can resolve the local atomic structure of both conducting and insulating materials. In addition, room-temperature scanning capacitance microscopy (SCM) [12, 13] has provided a means to characterize a surface by probing the local capacitance between the sample and tip. Because the electrostatic interaction is long-range, SCM is sensitive to the electronic behavior inside insulators. A review of scanned probe microscopy techniques can be found in [14].

In semiconductors, most of the physically interesting phenomena occur in electronic systems that exist beneath the sample surface. We have thus developed in our laboratory the technique of Subsurface Charge Accumulation (SCA) imaging. The technique is based on methods of ultrasensitive charge sensing that were originally put forward in connection with Single Electron Capacitance Spectroscopy, invented by Ashoori [15, 16].

SCA imaging allows the detailed study of electronic systems buried underneath the surface of semiconductor materials. In our experiments we use it to probe a 2-

dimensional electron system (2DES) at a temperature of 0.35 Kelvin in the regime of the integer quantum Hall effect (see section 1.2). A sharp metallic tip is positioned very close to the surface of a GaAs/AlGaAs semiconductor heterostructure with the aid of piezoelectric actuators. Unlike a conventional STM, no tunneling current flows between the probe and the sample. A periodic a.c. excitation is applied to the 2DES and causes the 2D layer to charge and discharge in response to the applied signal. By using synchronous lock-in detection we measure the charge that is induced on the tip as it is scanned 10 nm above the sample surface. This enables us to construct a charging map of the 2D electron layer buried inside the semiconductor.

In what follows, we discuss our typical sample design and provide a detailed description of the microscope and measurement apparatus. We then describe its distinct modes of operation. We also present preliminary results that confirm the instrument's ability to obtain high resolution images of mesoscopic systems in the IQHE.

2.1 Semiconductor Samples

The typical structure of our samples is shown in Figure 2-1. The wafer is a GaAs/AlGaAs heterostructure grown by molecular beam epitaxy (MBE). Its substrate consists of a thick layer of intrinsic GaAs. This is followed by 80 nm of AlGaAs, of which the uppermost 60 nm is doped with Silicon. The sample is capped with a 10 nm layer of intrinsic GaAs which forms the exposed surface. The 2-dimensional electron system is formed by electrons from ionized Si donor atoms. These electrons become trapped inside an approximately triangular quantum well in the GaAs/AlGaAs interface, 90 nm below the surface. A considerable distance of 20 nm separates the Si donors from the well so as to minimize electron scattering and improve the characteristics of the sample.

It must be added here that GaAs has a high density of surface states both on a free surface and at interfaces with a metal. They occupy a narrow band of energies near the middle of the bandgap, at $V_s \approx 0.7$ eV below the conduction band. The

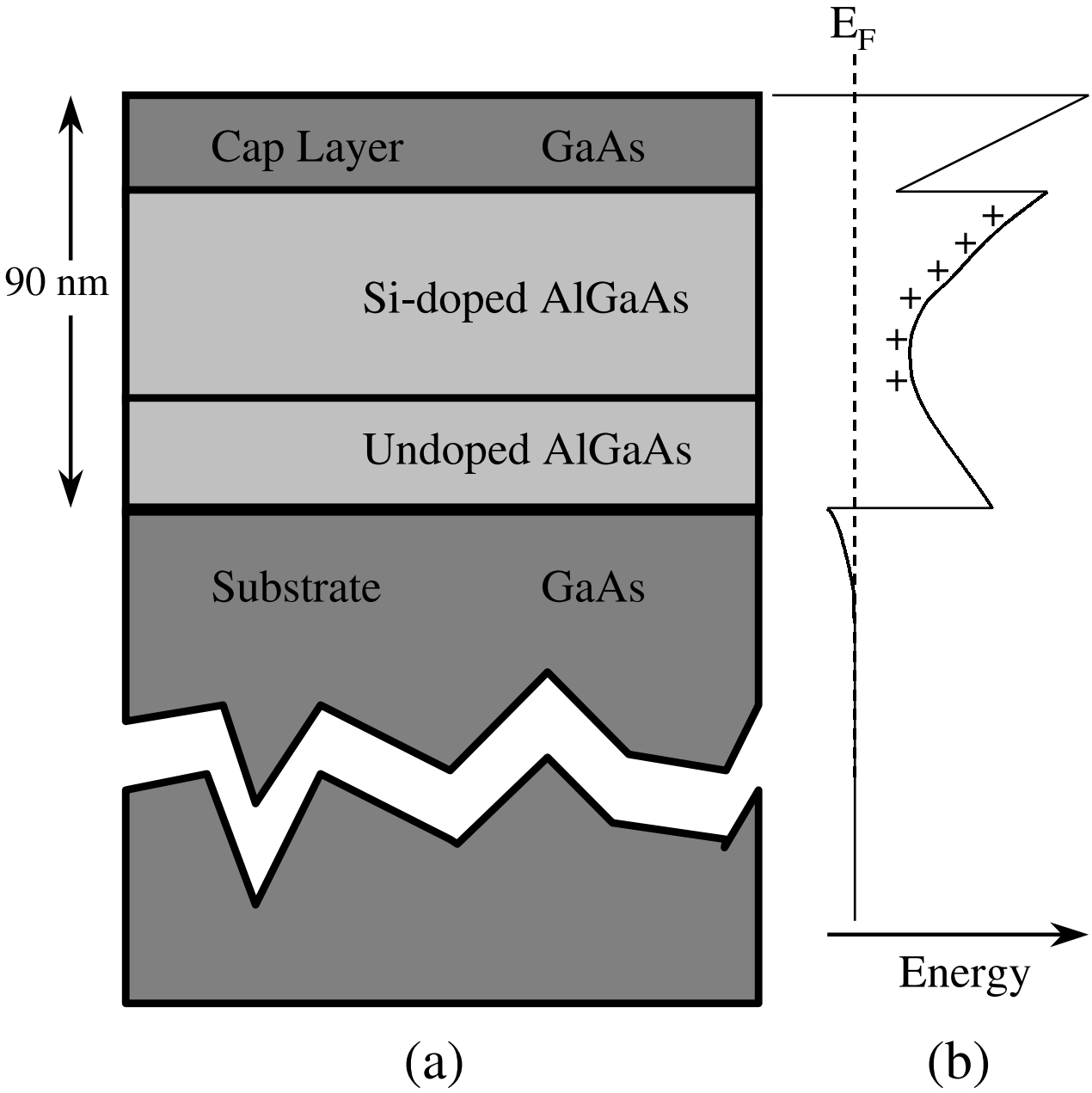

Figure 2-1: (a) Layer structure of the modulation doped heterostructure used for our measurements. Si donors are located 20 nm away from the AlGaAs/GaAs interface. (b) Conduction band diagram of the device. The dashed line shows the position of the Fermi level E_F.

Fermi energy is thus pinned by these states at that level. The resulting charge in these states must be balanced by that from the donors. It turns out that only a small fraction of donors ends up contributing electrons to the 2DES.

A final issue of great practical importance concerns the ways and methods that one uses to form an electrical contact with the buried electronic layer. These are discussed in detail in Appendix A.

2.2 The Cryogenic Scanning Capacitance Microscope

Our microscope is designed for operation inside a standard Helium-3 refrigerator, manufactured by Oxford Instruments. The microscope body is machined from brass metal and attaches to the end of a probe suitable for insertion in the He-3 cryostat. Samples are placed on a sample holder which is located $\sim$ 3 cm from the bottom of the apparatus. This allows for sample immersion in a shallow pool of pumped liquid Helium-3 and placement at the center of the field generated by a solenoid superconducting magnet which is included in the cryostat.

Coarse positioning and lateral manipulation of the sample is achieved using an inertial stepper [17, 18] based on the Besocke design [19]. Slanted ramps are machined at the bottom of the cylindrical sample holder which rests on top of three carrier piezoelectric (PZT-5A) tubes (see Figure 2-2). By applying a sawtooth wave to the appropriate quadrants of the tubes, the interplay between inertia and friction causes the holder to follow the motion of the carriers and translate either in the horizontal or vertical direction. The amplitude and frequency of the sawtooth, control the step size of the sample motion from a few nm to almost a μm per step in our setup. This design allows "walking" to regions of the sample as far as 1 mm away horizontally, and provides a 0.5 mm vertical range of motion.

However, in contrast to the original Besocke requirements [19], the scanning piezo tube is situated above the sample holder as shown in Figure 2-2(b). This tube is

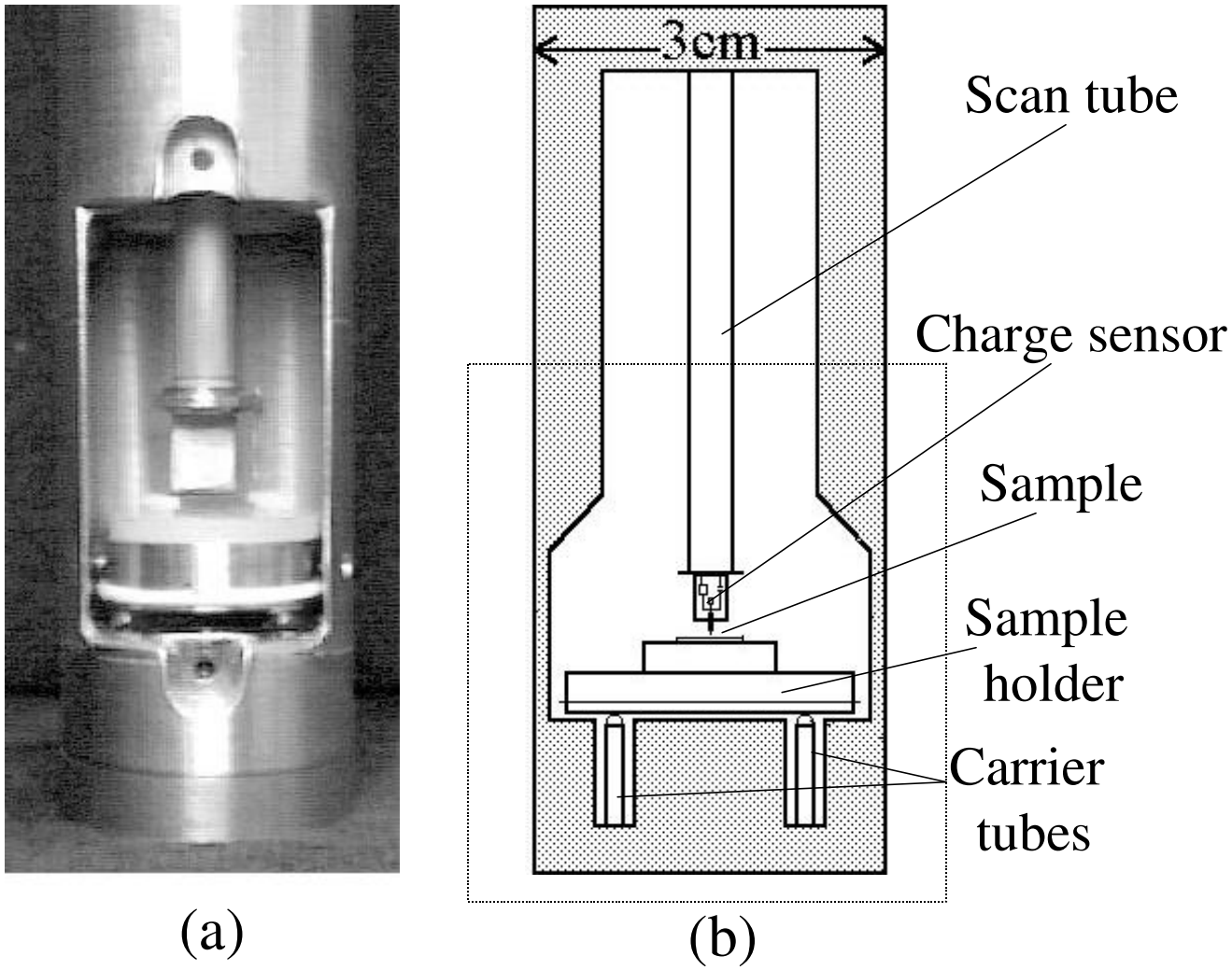

Figure 2-2: Scanning Capacitance Microscope Schematic. (a) Photograph showing lower microscope body. The scan tube and sample holder can be clearly seen. The sensor chip is attached to the brass piece at the bottom of the scan tube. After the sample holder is inserted in the microscope space and electrical connections are made to the sample, a door closes the front opening. (b) Schematic identifying different parts of the apparatus. The microscope body is bolted to the end of a cryogenic probe and is then inserted inside a top-loading He-3 cryostat. During operation, components inside the dotted line are fully immersed in a pool of pumped liquid He-3. A maximum area of $18\mu m^2$ can be scanned by the long (3 in.) scan tube at 0.35 Kelvin.

3 inches long and thus able to provide a large scanning range of $\approx 18\mu m$ at 350 mK (the base temperature provided by the refrigerator). The microscope is operated using a commercial scanning control and data acquisition system from RHK Technology. We should note here that the scan tube is not thermally compensated[1]. As a result, its operation at room temperature suffers from thermal drift of ≈ 10 nm/hour. However, this ratio is greatly reduced when the microscope is cooled to 0.35 Kelvin. A drift of ≤ 0.1 nm/hour is observed at this temperature and this provides extremely stable and reproducible operation for extended periods of time. All data presented in this thesis have been measured at that low temperature.

The scanning probes used in our studies are Pt-Ir metallic tips manufactured by electrochemical etching. The tips have a high aspect ratio and the radius of curvature at their apex is ~ 100 nm when new. They are mounted at the edge of a GaAs chip that contains the ultra-sensitive charge sensor arrangement (see Figure 2-5). The description and operation of that sensor is the subject of the following section.

2.3 Measurement Sensor. Design and Operation

The key innovation in our microscope is the design and implementation of a cryogenic sensor capable to detect minute changes in the tip-sample capacitance C_{tip} as the tip is scanned above the sample surface.

Our samples are GaAs/AlGaAs heterostructures with a 2-dimensional electron system buried beneath the surface as discussed in section 2.1. An electrical contact to the 2DES pumps charge in and out of the system, in response to an externally applied a.c. excitation V_{exc}. At zero magnetic field the 2D electron layer is highly conductive and hence the resistance between the electrical contact and the region under the tip is negligible. We may then simplify the tip-2DES system and represent it as a single capacitor with capacitance C_{sample}. The a.c. excitation is applied to one plate (the 2DES), and the signal from the opposite plate (the tip), is fed to a

[1] An example of a thermally compensated microscope that is based on principles deriving from our design, can be found in [20].

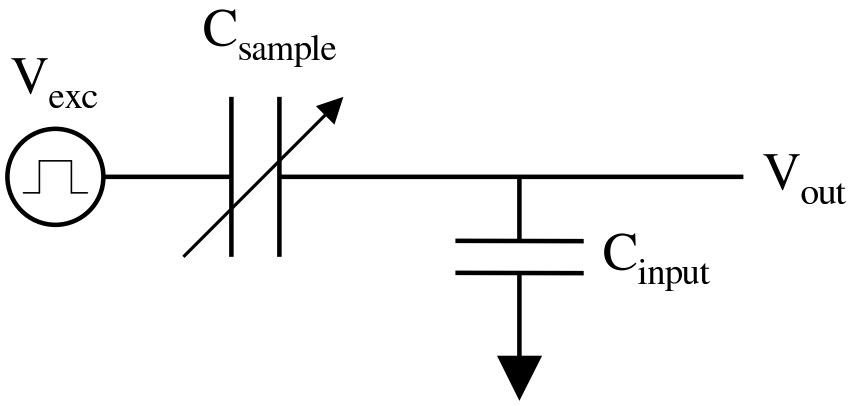

Figure 2-3: Simplified diagram of our capacitance measurement. The sample capacitance is C_{sample}. C_{input} corresponds to the input capacitance of the measurement apparatus.

measurement apparatus.

The excitation voltage is thus divided between C_{sample} and the input capacitance of the apparatus C_{input} as shown in Figure 2-3. One then has:

$$V_{out} = \frac{C_{sample}}{C_{sample} + C_{input}} \times V_{exc} \tag{2.1}$$

The signal V_{out} is measured with the aid of a lock-in amplifier. This is effectively a two terminal measurement. The excitation voltage is applied across the tip-sample impedance (a capacitor in this case) and the resulting current is recorded by reading the voltage across the input impedance of the measurement apparatus. This current is given by the charge induced on the tip during one period of the excitation, which is in turn directly proportional to the local charge in the 2DES below.

In order to increase our output signal, we can increase the excitation voltage while trying to minimize the input capacitance, as Equation 2.1 suggests. However, there is an upper boundary for the value of V_{exc} that is set by the voltage range within which the system under study is in the linear response regime. In addition, it is important that the excitation is such that does not perturb the observed structure in the data. Our measurements are typically performed with V_{exc} having an amplitude of 4 to 6 mV rms, at a frequency of 100 kHz. Although this voltage range may seem large[2], it

[2]For Quantum Hall measurements in GaAs, the relevant energy scale is given by $1.73\frac{meV}{Tesla}$, the

is important to remember that the sample has no direct electrical contacts to sources other than the excitation. This voltage is applied over large distances as the sample is several millimeters long. As a result, miniscule currents enter the 2DES and the voltage "drop" across the region of a scanned image ($\approx 10\mu m^2$) is very small. The second method that can be employed to increase V_{out}, namely minimizing the input capacitance, turns out to be a difficult task. Our experiments are performed at very low temperatures inside bulky cryostats. The coaxial cable connecting the lock-in amplifier to the sample is over 3 meters long with a capacitance to ground of about 300 pF. This large capacitance shunts the lock-in input impedance, effectively making $C_{input} \approx 300$ pF. The resulting $V_{out} \sim 10\ nV$ is a very small signal and it is extremely hard to measure it accurately in an experiment.

In order to address these problems we have developed a two-stage amplifier that is based on the original work by Ashoori [15]. The critical element of the first stage amplifier is a cryogenic high electron mobility transistor (HEMT) located very close to the microscope tip (and hence to the sample). This transistor is designated as TR1 in the circuit diagram in Figure 2-4 and is often referred to as the "measurement transistor". TR1 practically serves as an impedance matcher. With a low capacitance input, it drives high capacitance lines. Its gate is electrically connected to the scanning tip and it is biased through a nearby HEMT (TR2) whose source-drain channel acts effectively as a $\approx 10\ M\Omega$ resistor. This of course happens when TR2 operates itself near its saturation regime. The transistors used are commercially available, and the ones chosen have the lowest possible input capacitance. We further reduce this to half its original value by cleaving the transistors in the middle. We thus end up with $C_{input} \approx 0.5$ pF.

The second amplification stage consists of yet another HEMT, TR3. This transistor is physically located at the region where the top loading probe - at the end of which the microscope body is attached - makes thermal contact with the 1 K pot inside the cryostat. A 100 pF capacitor C_{13} is employed to separate the d.c. voltages between the TR1 and TR3 circuits. The amplified output of TR3 is then connected

separation of Landau levels. See section 1.2

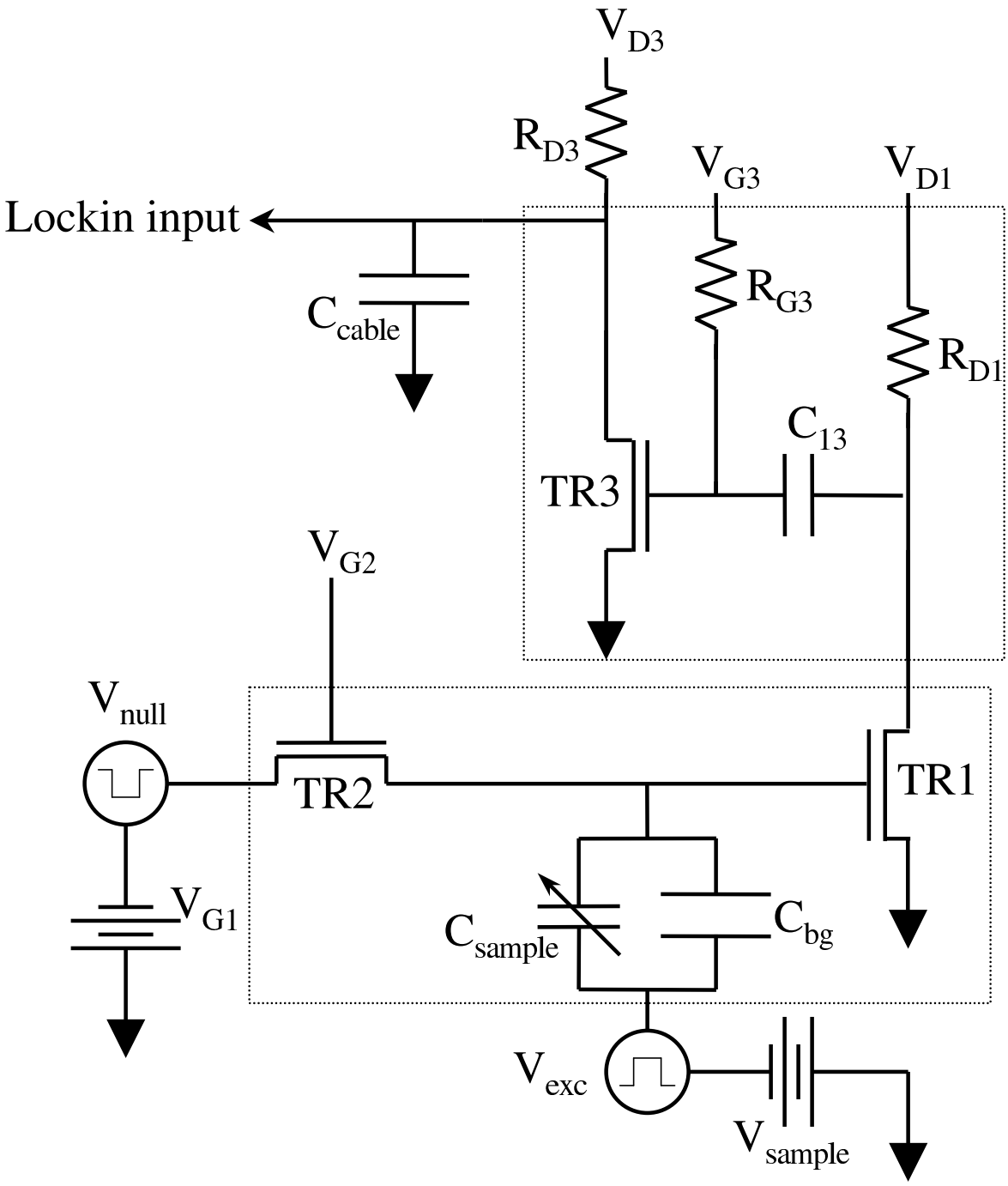

Figure 2-4: Low-temperature charge amplifier circuit. Components inside the dotted line at the bottom are held at a temperature of 0.35 K during operation. The upper dotted line contains components located very near the so-called "1 K pot" region of the top-loading probe. These are correspondingly held at 1.1 K.

The tip can be biased with respect to the 2DES by changing V_{sample} which is a variable d.c. source coupled to the a.c. excitation V_{exc}. TR2 performs the dual task of biasing TR1 *and* nulling away the background signal by acting as a standard capacitor in the balancing bridge.

via a long coaxial cable to the input of a lock-in amplifier. Thus, TR3 serves as an impedance matcher (cf. TR1) that actually drives the load of the line. All three transistors are mounted in a fashion that leaves their characteristics unaffected in the presence of magnetic fields.

Another complication is added by a factor that has so far been tacitly ignored: the background capacitance C_{bg} between macroscopic parts of the tip and its surrounding environment. Its value of ≈ 0.1 pF is 3 orders of magnitude greater than the quantities we are trying to measure, but luckily, it remains constant throughout the experiment. As a result, we subtract it away using a balancing bridge technique [15]: A second a.c. voltage differing in phase by 180° from the excitation, is applied to a standard capacitor C_s. The detector (i.e. TR1) measures the signal at the balancing point of the bridge. We note here that instead of using a separate capacitor as the standard one, we let the bias transistor TR2 assume this role by taking into advantage the capacitance C_{ds} between its source and drain. So, effectively, $C_{ds} \equiv C_s$ when TR2 is fully closed. The out-of-phase nulling voltage is applied to the source of TR2 which is also used to d.c. bias the measurement transistor. The setup is depicted in Figure 2-4. By properly tuning V_{null}, the large signal due to C_{bg} becomes effectively zero and one is ready to resolve capacitance changes from the 2DES to the nanometer sized tip.

The measurement technique described in this section has also been used and described in relation to another class of experiments performed in our research group. These experiments are an extension of Single Electron Capacitance Spectroscopy [15, 16] and measure the ground state energies of quantum dots containing a variable number of electrons. A full discussion regarding that work can be found in Reference [21].

2.4 Modes of Operation

Our microscope can operate in three totally independent imaging modes. This ability greatly enhances semiconductor sample characterization and in some cases also helps for precise tip or sample positioning.

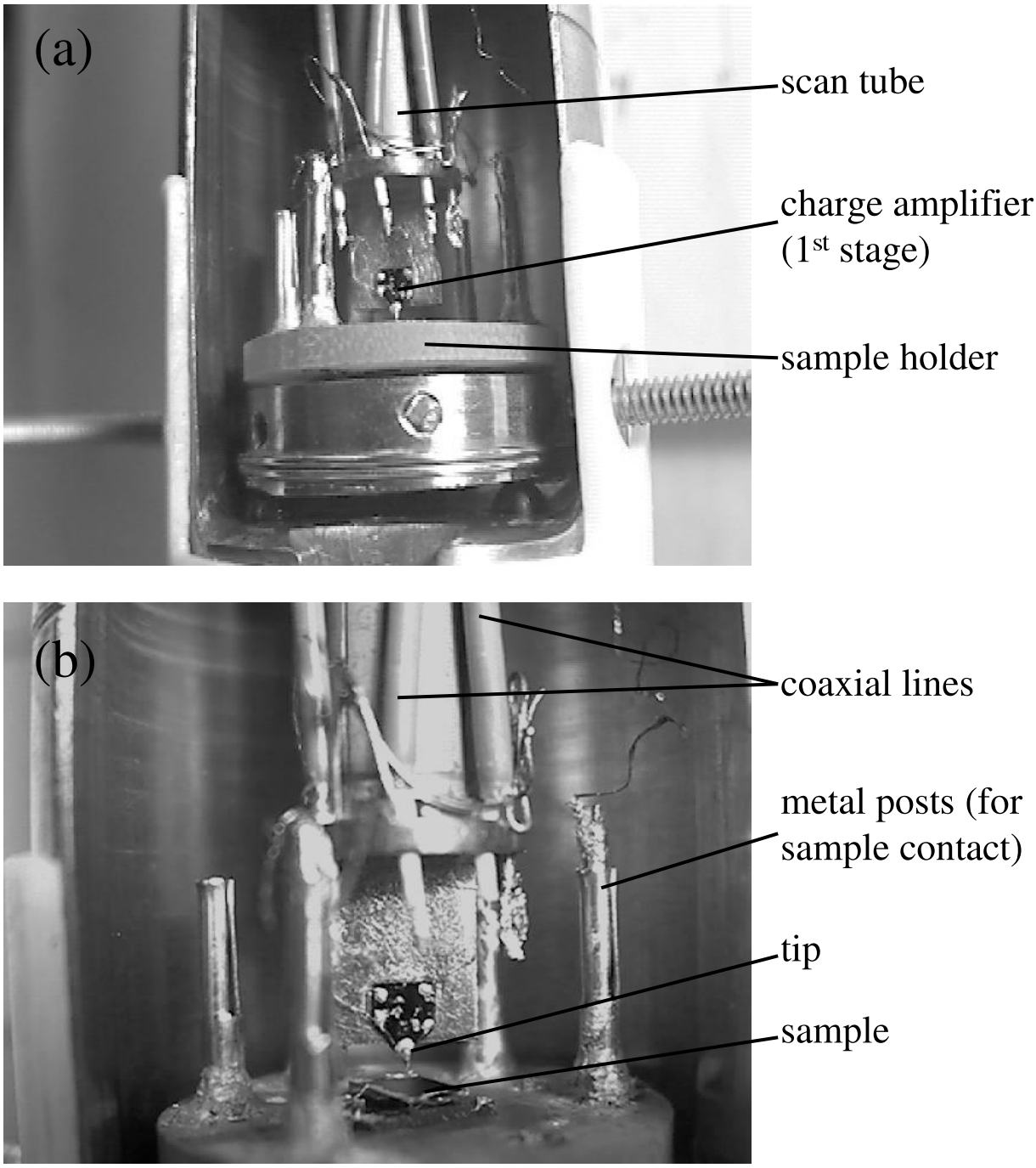

Figure 2-5: Capacitance microscope pictures taken just after warming the instrument to room temperature from 4 K. (a) Sample holder and "bridge on a chip" sensor mounted at the bottom of the scanning piezo tube. (b) Zoom-in picture. TR1 and TR2 are mounted on the GaAs chip along with the metallic tip. The sample is positioned directly underneath and connections to it are made using the posts on the sample holder.

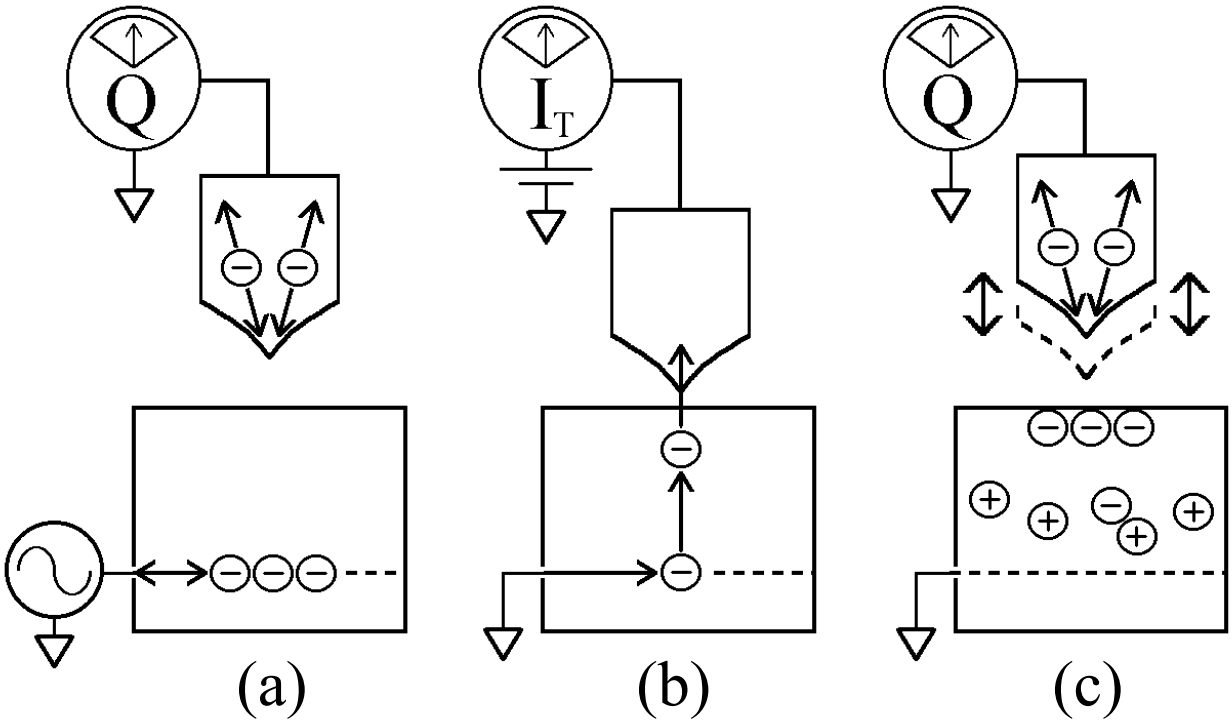

Figure 2-6: Microscope operation modes. (a) Capacitance (b) Tunneling (c) Kelvin probe. The Kelvin probe mode is depicted from the sample's frame of reference. In the actual experiment, the tip is held constant and the sample undergoes the oscillatory motion.

2.4.1 Capacitance (Charge Accumulation) Mode

With the sample cooled to 0.35 K, measurements can begin as soon as the HEMTs in the amplifier array described in the previous section, are powered up and properly biased. The gain of the amplifier increases as one pinches-off the transistors. However, their output impedance also increases with the pinch-off. The load on the amplifier is determined by the cable capacitance and the frequency, so a sample excitation frequency of 100 kHz gives [22]:

$$Z_{out} \leq Z_{load} = \frac{1}{j\omega C_{cable}} \approx 5k\Omega \tag{2.2}$$

We can thus bias the measurement transistor hard and obtain higher gain because TR1 does not drive a large load. At the same time, we can leave TR3 in a more "open" state and increase its source-drain current. Thus, TR3 serves as an impedance matcher, while operating around unity voltage gain. The gate biasing resistors R_{G3} and TR2 (which, as mentioned previously, is practically used as both a resistor and a standard capacitor) are then chosen so that their resistance $R_{bias} \gg 1/\omega_{exc}C_{in} \approx 3\ M\Omega$. In our setup $R_{G3} = 10\ M\Omega$ and TR2 is tuned so that its source-drain resistance is at least 10 $M\Omega$. The RC time constant at their inputs then becomes $\approx 10\ \mu s$. This is longer than $1/\omega_{exc} = 1.6\ \mu s$ and ensures that the amplifier circuit can detect charge motion within the 2DEG, in synchrony with the applied a.c. excitation. Finally, we arrange the biasing parameters so that the power dissipated in TR1 does not exceed 3 μW, while the power dissipated in TR3 is kept at around 10 μW.

We find that by using the two-stage amplifier and taking into account the issues discussed above, we obtain a gain of ≈ 10 in signal and a minimum noise level at the tip of 6 $\frac{nV}{\sqrt{Hz}}$. The resulting sensitivity is 0.02 electrons/$\sqrt{Hz}$ [15]. Charge Accumulation Imaging proceeds by recording the signal in phase with the a.c. excitation and the signal lagging 90° from it, with the aid of a lock-in amplifier connected to the drain of TR3 (Figure 2-4). If the measurement is performed while the microscope tip is scanned close to the sample surface, one obtains a detailed charging map of the 2DEG layer within the semiconductor. Such an image appears in Figure 2-7. This

image is taken at a field of 3.013 Tesla, corresponding to the $\nu = 2$ filling factor for the bulk of the 2DEG in that particular sample. One clearly identifies areas of high and low charge accumulation in the "in-phase" scan, as bright and dark regions respectively. The exact meaning of such images will be addressed in the chapters that follow.

We may carry out a different type of measurement by keeping the tip at a fixed position above the surface while the magnitude of the magnetic field, applied perpendicularly to the plane of the electron gas, is varied. The lock-in records the capacitance changes in the tip-2DEG system and the resulting trace is shown in Figure 2-8. We make this measurement on a sample that comes from the same wafer as the one employed in connection with the data in Figure 1-1. The capacitance is constant at low magnetic fields but develops strong oscillations at high fields. This result is a direct manifestation of the Shubnikov-de Haas effect. Its behaviour mirrors the changes of the longitudinal conductance σ_{xx} of the electron layer as dictated by the quantum Hall effect. For example, field values at which the tip-2DEG capacitance is low, correspond to low values for σ_{xx} that in turn characterize an almost insulating 2DEG. To understand why this is the case, we should remember that minima in σ_{xx} occur at fields when an exact number of Landau levels is filled. The Fermi energy then lies in a region where the 2DEG density of states goes to zero (or more precisely a region of localized states), and longitudinal conduction disappears. The connection with Figure 1-1 is made through the fact that $\rho_{xx} \propto \sigma_{xx}$ and so when $\sigma_{xx} \to 0$, $\rho_{xx} \to 0$ as well.

Combining Equation 1.4 with $\nu = \frac{n}{N}$ (the definition for the filling factor ν from section 1.2), we get that:

$$B = \frac{hcn}{e\nu} \tag{2.3}$$

As we have already discussed, the Shubnikov-de Haas minima in the capacitance signal, occur at fields B_i corresponding to $\nu = i$ where i is an integer. A plot of $1/B_i$ versus $\nu \equiv i$ should thus give a straight line with a slope of e/hcn. Such a line is shown in Figure 2-8 and can be used to accurately determine the 2DEG density n.

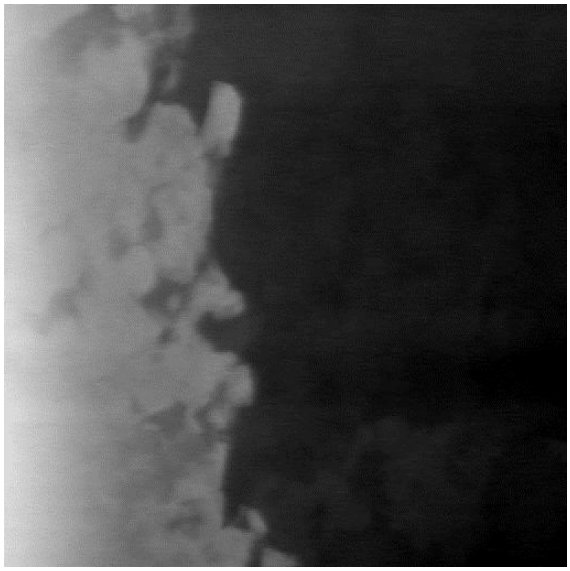

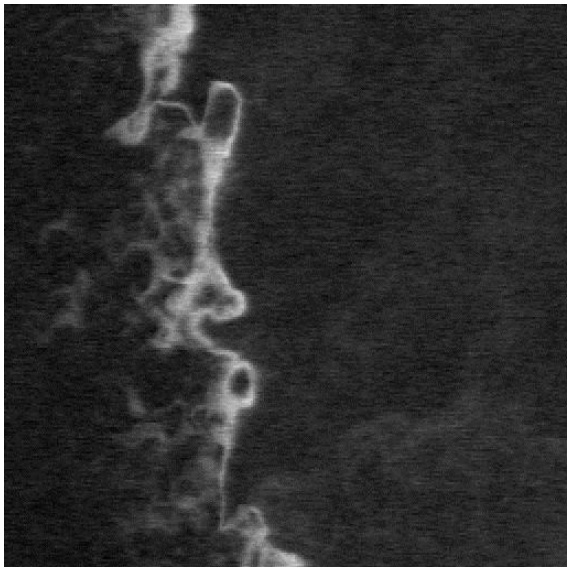

Figure 2-7: $5 \times 5 \mu m$ in-phase and out-of-phase images of a 2D electron gas, acquired with the microscope operating in charge accumulation mode. The in-phase image shows regions of high and low charge accumulation near the $\nu = 2$ Landau level. The high signal in the out-of-phase image lags the applied a.c. excitation by exactly 90°, and delineates the boundary between charging and non-charging regions of the 2DEG. Both images are recorded concurrently with the aid of a two-channel lock-in amplifier.

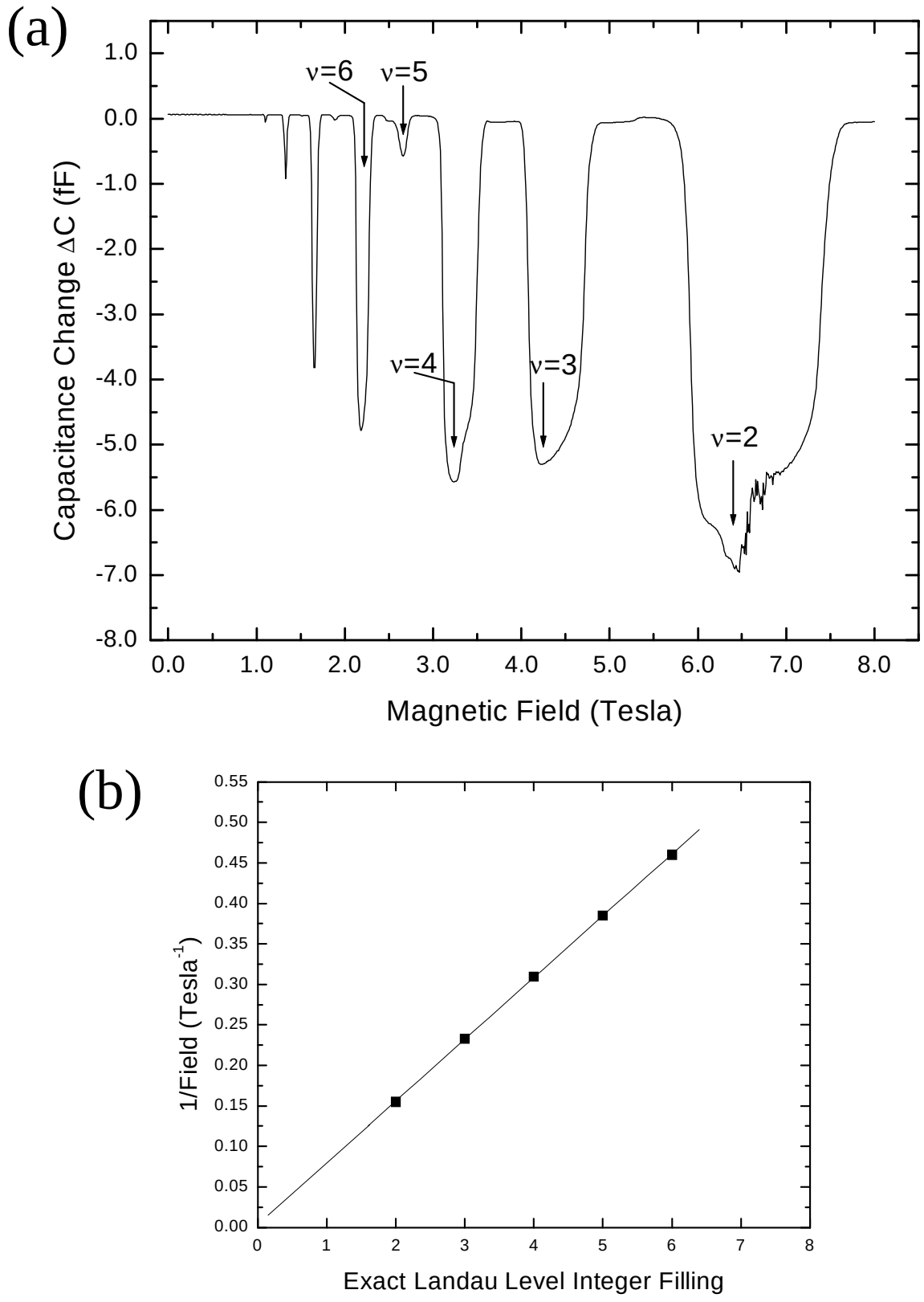

Figure 2-8: (a) Change in tip-2DEG capacitance as a function of magnetic field. The minimum at 6.47 T corresponds to the $\nu = 2$ filling factor. $\nu = 1$ occurs at 12.94 T which is beyond our superconducting magnet range. (b) Density calibration of the 2-D electron layer.

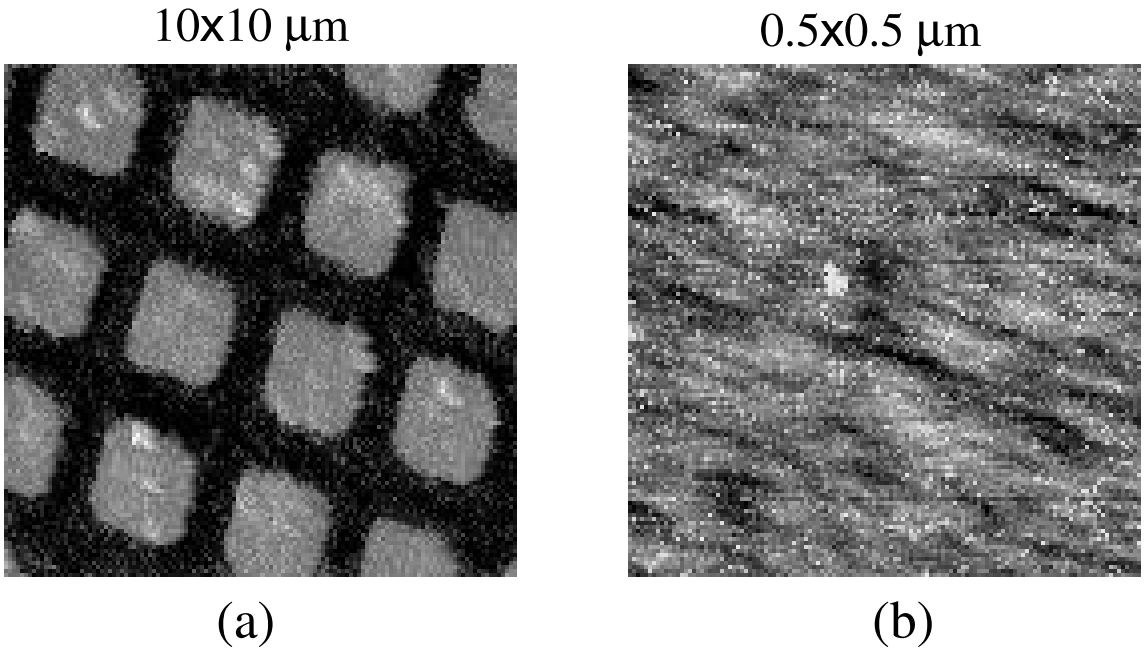

Figure 2-9: Scans taken while operating the microscope in conventional tunneling mode. (a) 10×10 μm scan of an array of Au squares. The height of the square mesas is 500 Å. (b) GaAs surface of the sample depicted in Figure 2-1. The scan window is 0.5×0.5 μm large.

We routinely apply this procedure in order to measure n in our samples, which in this case turns out to be 3.17×10^{11} cm^{-2}.

2.4.2 Tunneling Mode

Our microscope can be operated as a conventional STM simply by suspending all a.c. voltages and connecting the gate bias lead to a current-to-voltage amplifier. The tip voltage is then set to a value of 4 Volts relative to the 2-D electron system. More precisely, a d.c. voltage of -4 V with respect to the tip is applied to the 2DES. A region of electron accumulation then forms directly underneath the tip, and the bending of the conduction band in our semiconductor sample yields a tunneling resistance between the 2DES and the surface of ≤ 40 $G\Omega$. Electrons can subsequently tunnel to the metal tip with the tunneling rate determined by the vacuum barrier thickness (i.e. the distance between the tip and the surface). Consequently, measurement of the tunneling current I_{tun} is sensitive to the topography of the surface, just as in conventional STM. A simple schematic of the measurement is given in Figure 2-6.

We use a feedback loop, provided by the microscope control electronics, to set the z-position of the scan piezo tube (and hence the tip) so that I_{tun} is kept constant. The topography is imaged by monitoring the feedback magnitude as the tip is scanned above the surface. We typically maintain $I_{tun} \approx 100$ pA which results in a tip sample separation of about 5 Å.

The tunneling mode proves useful for finding the exact position of the sample surface, e.g. when the initial tip-sample approach is performed after cooldown to 0.35 K. It can also accurately determine the tilt of the sample plane relative to the horizontal one, so that one may apply the appropriate plane compensation parameters to the scan tube to correct for this effect. This is particularly convenient when we wish to operate the instrument in charge accumulation or Kelvin probe mode, since in these modes the microscope scans at constant tip height with the feedback loop turned off. We describe Kelvin mode in the next section.

Figure 2-9 shows a tunneling image of a microfabricated Au sample that we use to calibrate our piezoelectric tubes. The constant I_{tun} image brings out an array of square mesas 500 Å tall. Since in this case the sample surface is fully conductive, application of a 0.25 Volts bias to the tip with respect to the sample, is enough to cause electron tunneling.

A topographical image of the GaAs surface of one of our 2DEG samples appears in the same Figure. The elongated islands are consistent with STM measurements on homoepitaxially grown GaAs, indicating the $[\bar{1}10]$ direction [23]. However, in the case of this sample, the resulting tunneling current locally disturbs the charge distribution in the AlGaAs layer, thereby permanently modifying the density of electrons in the 2DEG. As we shall see in Chapter 4 , we may use this effect to our advantage in order to create and study artificially created density gradients in the electron layer. In our later work though (Chapters 5 and 6), we avoid tunneling altogether and employ alternative techniques (to e.g. pinpoint the exact location of the sample), that leave the 2DEG totally unperturbed.

2.4.3 Kelvin Probe Mode

The discussion in previous sections, clearly shows that the charge accumulation imaging mode is sensitive only to charge movements inside the 2-D electron system. In contrast, it is also possible to operate the microscope in a way that makes the measurement sensitive to the static charges in the insulating layer above the 2DEG as well as to the work function difference between the tip and the GaAs sample surface [24]. We thus arrive to the Kelvin probe operation mode, whose principles date back to 1898 [25]. Kelvin probe is noninvasive and is based on a vibrating capacitor technique. It has so far found a number of applications concerning studies on metal [26], semiconductor [27], polymer surfaces and interfaces [28], catalysis [29] as well as surface charge imaging [30, 31].

In our implementation, we measure oscillating charge on the metal tip using the amplifier setup described in section 2.3. Unlike capacitance mode, the signal does not originate as a response to an a.c. voltage. Instead, the sample itself is vibrated in the vertical direction at a frequency of 2 kHz (see schematic in Figure 2-6). We achieve this by applying a sinusoidal voltage (500 mV rms) to all quadrants of the carrier piezo tubes, leading to a sample vibration amplitude of ~ 10 nm. The charge induced on the tip will oscillate at this frequency if the tip is above a region where the electric field changes with distance from the surface[3]. Such a region above the 2DES may arise because of variations in the concentration of ionized donors, or from excessive electrons trapped in surface states. This situation is depicted in Figure 2-10 that shows Kelvin probe data from a 15×15 μm scan window on the GaAs surface of our heterostructure. Prior to the Kelvin measurement we have performed tunneling scans in a 1×1 μm area at the center. The image clearly shows the perturbation in the central region that extends beyond the original 1 μm^2 area. The tunneling current has permanently redistributed charge in a small region of the AlGaAs donor layer and/or the GaAs surface (see Figure 2-1) and this is the source of contrast in the Kelvin probe image.

[3]The difference in contact potential (also known as work function) between the metal tip and the semiconductor, is another source of Kelvin signal, and will be examined below.

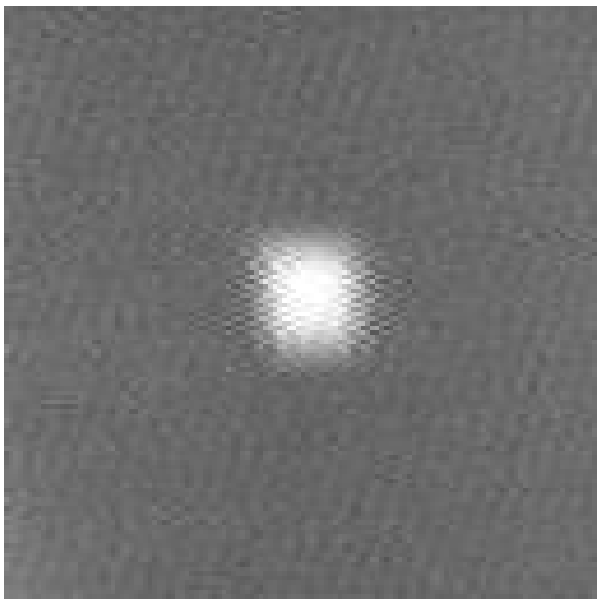

Figure 2-10: Scan in Kelvin probe mode. The high signal in the central region reveals the charge perturbation in the sample donor layer that has been caused by tunneling.

The Kelvin signal is usually superimposed on a relatively uniform background electric field arising from the work function difference between the Pt-Ir metal tip and GaAs. From the discussion in Appendix C, this signal varies as:

$$\frac{dV}{dt} \propto (V - V_k)\frac{dC}{dz} \tag{2.4}$$

where C and V_k are the tip-sample capacitance and contact potential respectively.

This field can thus be nulled by placing the tip well outside any perturbed region and balancing the signal by applying a d.c. voltage between the tip and the 2DEG. Figure 2-11 plots the Kelvin signal as a function of tip-2DEG bias, with the tip positioned at different heights z above the surface. The voltage corresponding to zero signal is the one required for nulling. As expected, curves for different values of z, all intersect at this point, since the work function difference, and hence $V_{null} = V_k$, are unique.

The measurement depicted in Figure 2-12 provides an alternative way to determine V_k and eliminate d.c. fields between the probe and the 2DEG. Here, the variable

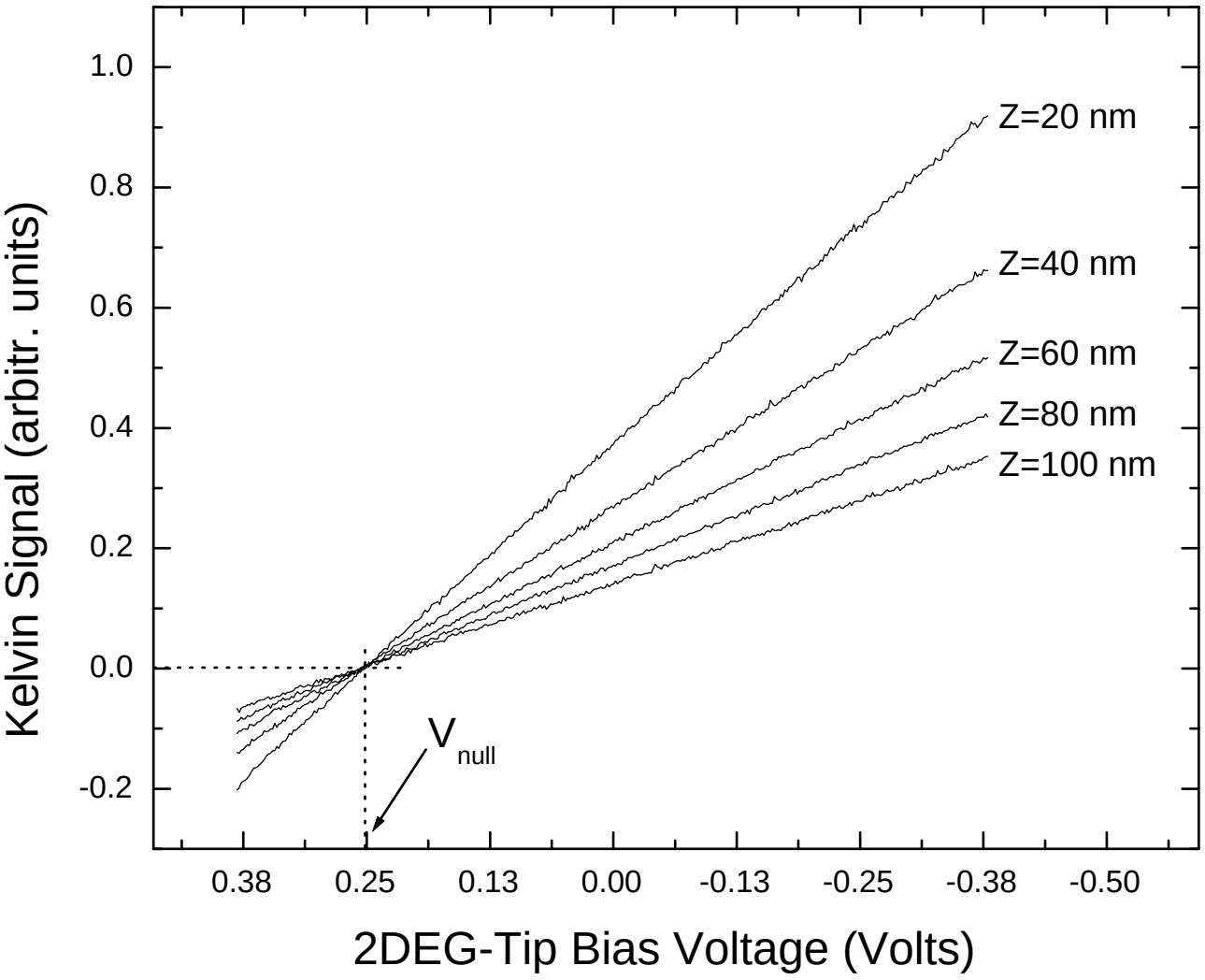

Figure 2-11: Kelvin signal measured for different tip-sample separations. Application of 0.255 V to the tip with respect to the 2DEG, eliminates the electric field created by the tip-GaAs work function difference.

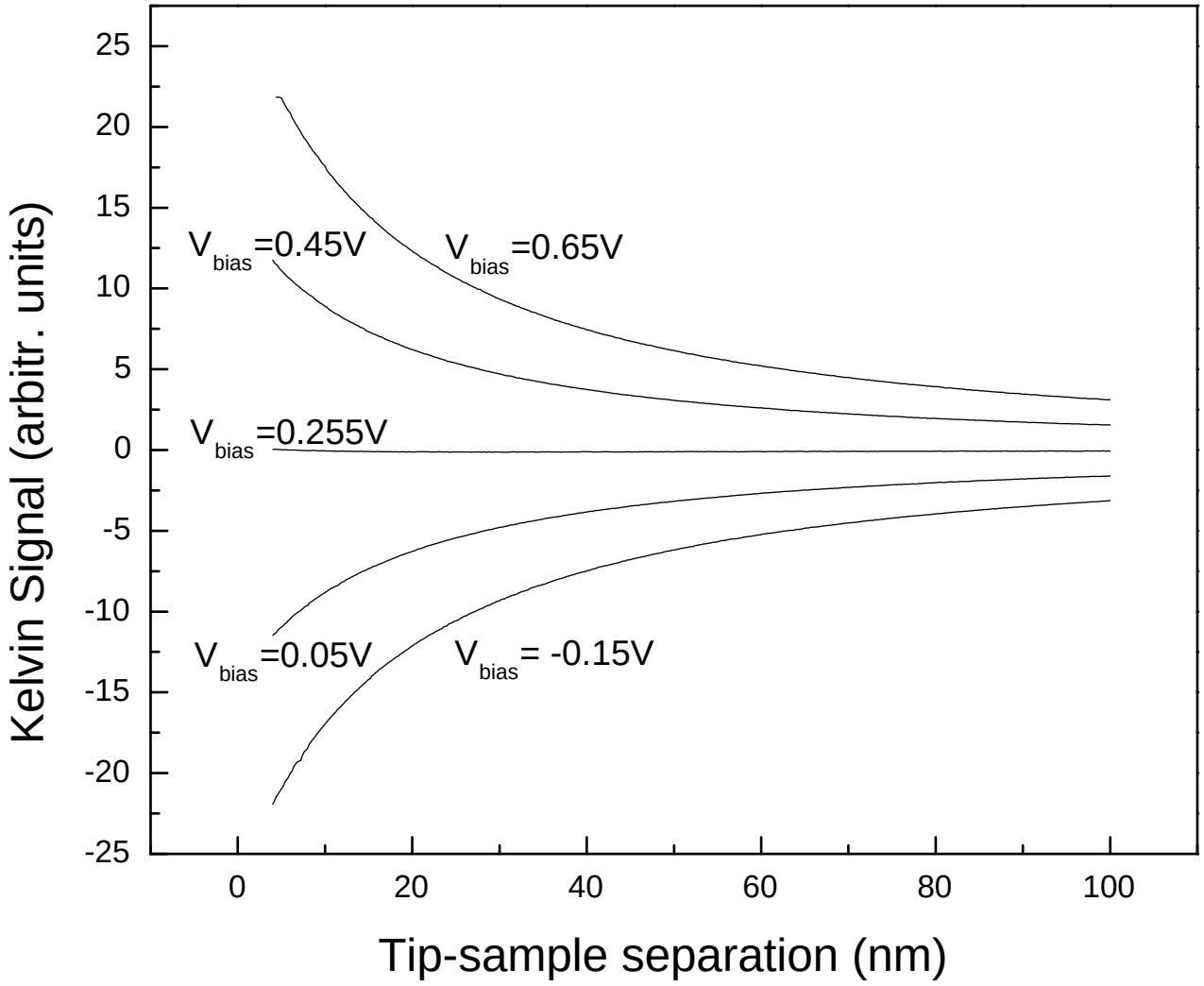

Figure 2-12: Kelvin signal as a function of tip-sample separation z, measured for different tip-sample bias voltages. Curves away from nulling voltage diverge as z is decreased, while the curve at $V_{null} = 0.255V$ remains constant (at 0) for all z.

parameter is the tip height z while V_{bias} is held constant. Curves diverge as z is diminished due to the $\frac{dC}{dz}$ term in Equation 2.4. As it turns out, our method is capable of determining the value for the contact potential V_k with a 2 mV accuracy.

2.5 Summary

This chapter described the design and operation of our Scanning Capacitance Microscope. During measurements, we primarily operate the instrument in charge accumulation imaging mode. However, complementary information on the arrangement of static charges in the sample as well as on surface topography, can be obtained with the use of Kelvin probe and tunneling modes. This chapter also explained how the Kelvin signal can be used to null the electric field between the tip and the GaAs due to the mismatch in their work functions. Measurements can then take place without the tip affecting the electronic density in the 2D layer.

In the following chapters, we employ our techniques to image a 2DES and measure several of its properties in the QHE regime.

Chapter 3

Imaging the Quantum Hall Liquid: Filamentary structures and Concentric Compressibility Ripples

The unusual properties of two-dimensional electron systems (2DES) that give rise to the quantum Hall effect have prompted the development of new microscopic models for electrical conduction. The bulk properties of the QHE have been studied experimentally with a variety of probes including transport [5, 32], photoluminescence [33, 34], magnetization [35] and capacitance [36, 37] measurements. However, until recently, the microscopic electronic structure in the quantum Hall regime had remained inaccessible to more direct measurements. This was due to the fact that the 2D systems typically exist some distance (about 100 nm) below the surface of a semiconductor material.

Our cryogenic scanning-probe technique introduced in Chapter 2, permits high resolution examination of mobile electrons inside materials and it is here employed to image directly nanometer scale structures that exist in the quantum Hall regime [38]. The advent of our technique, occurred at a time of heightened interest on the microscopic aspects of 2D electron systems. A number of research groups have also developed their own experiments that use scanning methods to probe properties of 2DEG systems and the QHE [39, 24, 40, 41].

3.1 Samples and Measurement method

Subsurface charge accumulation (SCA) imaging, measures the local accumulation of charge in a 2DES in response to an applied a.c. excitation. Since it is an a.c. method, it has significant advantages for the study of the QHE over measurements which image the distribution of static charges. Samples contain static charges from both the surface and dopant layers underneath, which can mask charging features in the 2D layer. We have described the technique in detail in Chapter 2 and in this section, we will only summarize its principles for completeness. We perform SCA imaging at a temperature of 0.35 Kelvin. A sharp conducting tip is connected to a highly sensitive charge detector and is scanned 10 nm above the sample surface as shown in Figure 3-1. A 4 mV, 100 kHz a.c. excitation is applied through indium ohmic contacts to the 2DES, causing charge to flow in and out of the system. A lock-in records the charge induced on the tip and we obtain two images, one for charge accumulating in-phase, and another for charge accumulating out-of-phase (90° lagging) with the excitation. We may also map the sample's surface topography and local distribution of static charges, by respectively operating the microscope in tunneling and Kelvin probe mode (see section 2.4).

The sample is a standard MBE GaAs/AlGaAs heterostructure grown by Prof. Melloch in Purdue University. The 2DES is located 90 nm beneath the surface. Its density is $3.17 \times 10^{11}\ cm^{-2}$ and it has a transport mobility of 450,000 $cm^2V^{-1}s^{-1}$. Its structure appears in Figure 2-1.

3.2 Experimental results, Part I

SCA images taken at zero magnetic field display no contrast, since the 2DES has a constant density of states and charges uniformly. As the field is adjusted towards the centre of the Hall plateau, the charge accumulation seems to diminish and detailed spatial patterns of charging appear. In our images presented throughout this thesis, bright and dark shades of gray correspond to higher and lower levels of sig-

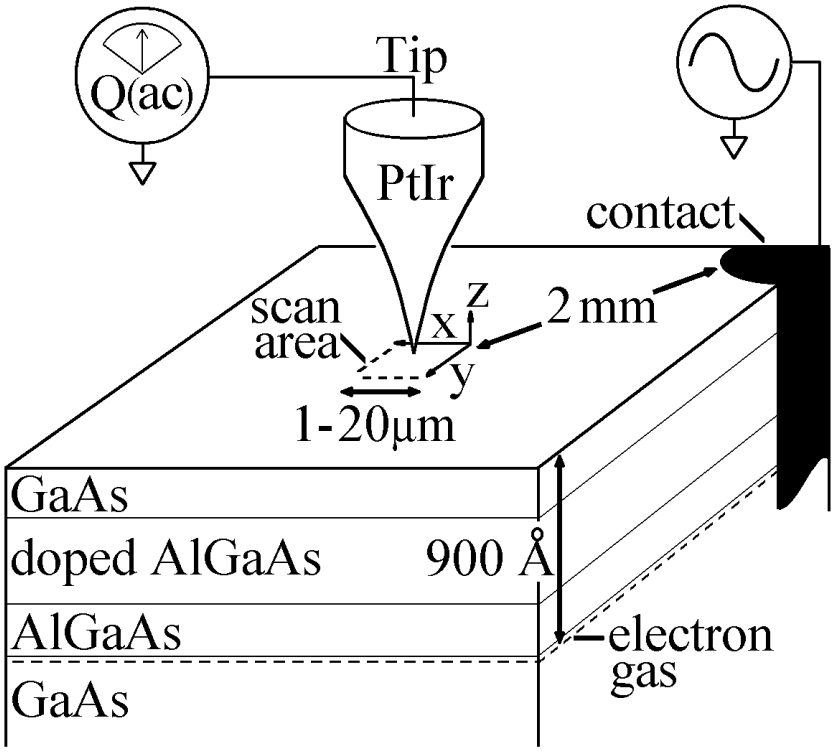

Figure 3-1: Sample and measurement configuration diagram. The microscope operates with the sample immersed in liquid He-3 at a temperature of 0.35 K.

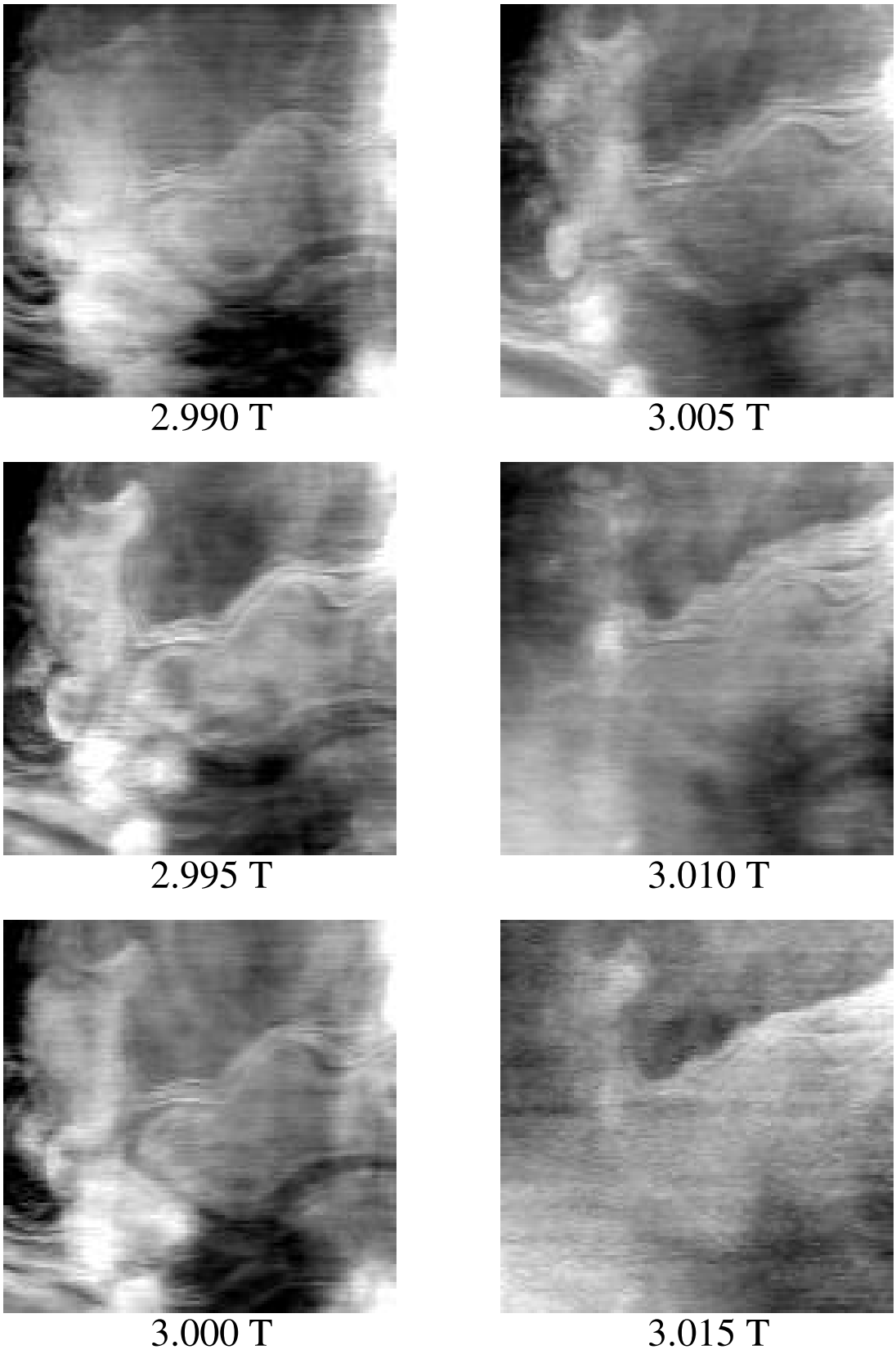

Figure 3-2: Sequence of in-phase SCA images around $\nu = 4$. The scans are 3.3×3.3 μm large. The smallest features displayed are consistent with the expected spatial resolution of the probe ($\approx 100nm$).

nal respectively. The upper boundary for the spatial resolution in our scans is given approximately by the depth of the 2DES below the sample surface (90 nm) [42]. We concentrate our measurements on the $\nu = 4$ Hall plateau which is centered around 3.04 T for the bulk of the sample. Images taken at fields of more than 0.15 T away from the centre of the plateau do not display any features. In contrast, from Figure 3-2, one sees that clear charging features are observed for fields near the plateau centre. The features remain completely unchanged with time but their evolution is very sensitive to magnetic field. There is little correlation between images differing by 0.020 T.

3.3 Experimental results, Part II

We again use SCA imaging and study a two-dimensional electron gas in another GaAs/AlGaAs sample. The electron density n is now such that $\nu = 4$ in the bulk occurs at 3.5 T. We focus on a region of the 2DEG with n slightly above average. The area has most likely been created by releasing some electrons that were trapped in the DX centres in the donor layer. Again, the SCA measurement performed at zero magnetic field does not reveal any significant structure because of the constant 2D density of states. The situation however changes in the presence of a magnetic field. Figure 3-3 presents SCA images at three field values around 4.00 Tesla. The images are dominated by an irregularly shaped spot whose origin may be understood as follows: Regions of the 2DEG with different densities reach an integer Landau level filling factor at different values of the magnetic field. Since the 2DEG density in the region of study is higher, most locations reach $\nu = 4$ at a field higher than 3.5 Tesla. These locations form an effective boundary that separates the bulk of the sample where $\nu < 4$, from the interior of the dark spot with $\nu > 4$. The bulk charges through the Ohmic contacts but the $\nu > 4$ area has effectively become disconnected from the rest of the 2DEG and hence it appears dark in our scans. With increasing magnetic field the spot shrinks and its perimeter marks the position where the 2DEG density exactly satisfies the condition for $\nu = 4$ integer filling.

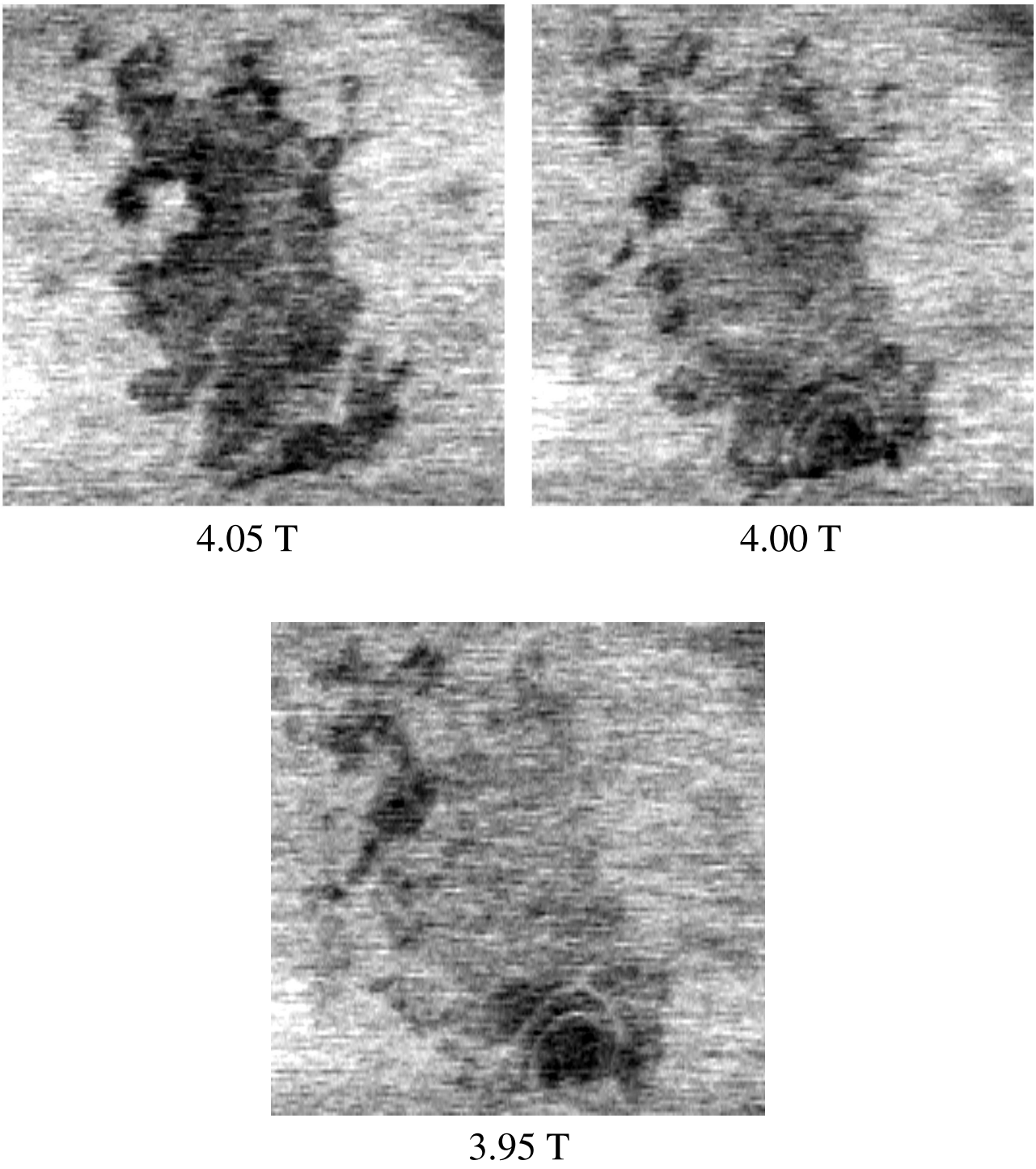

Figure 3-3: In-Phase SCA measurements of a 6×6 μm region at three different magnetic fields. Areas of high charge accumulation are bright whereas areas excluding charge are darker.

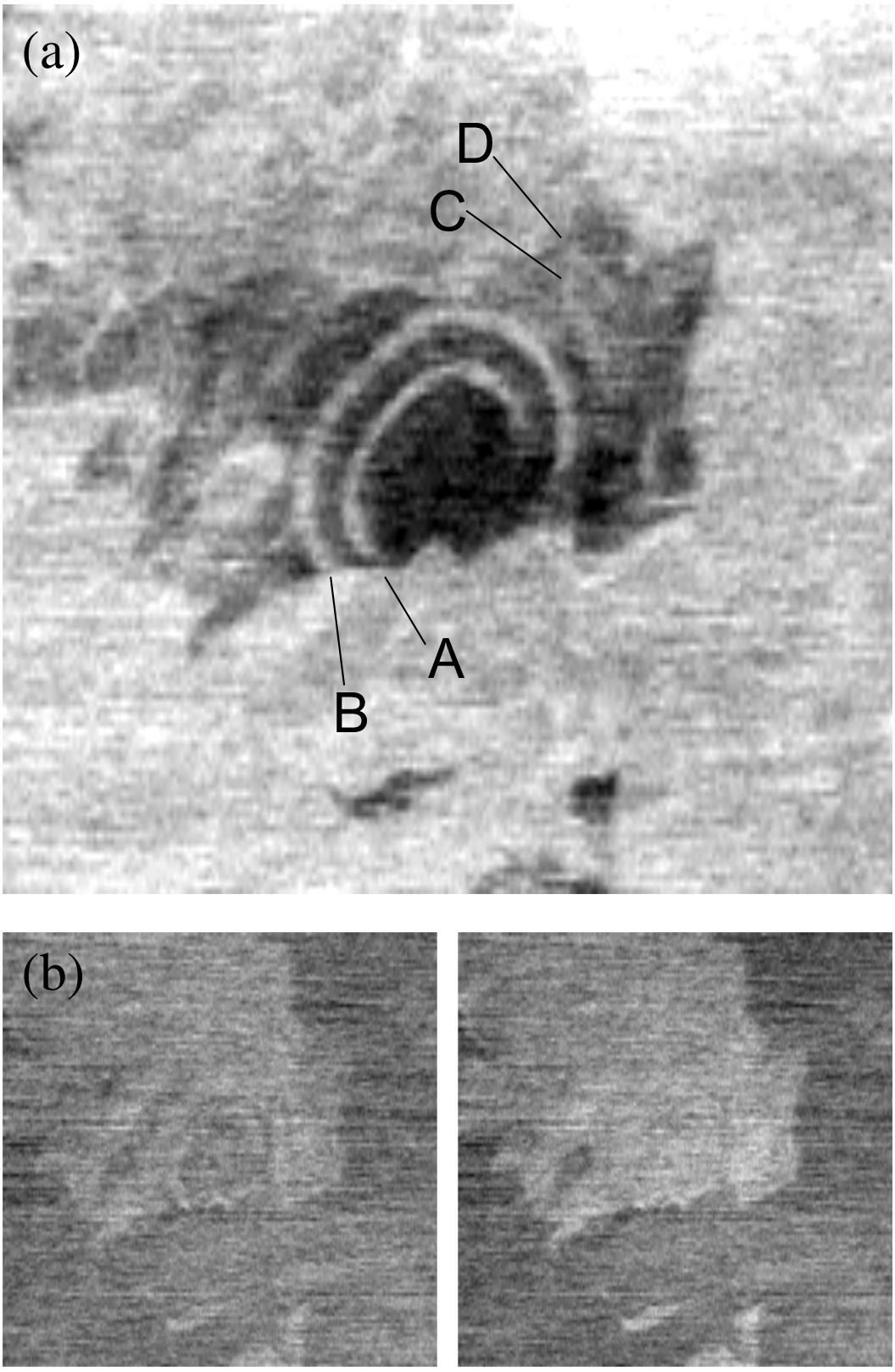

Figure 3-4: (a) Measurement in-phase with the excitation of a 4×4 μm region centered around the structures observed at 3.96 Tesla. (b) Signals lagging from the excitation by 90 (left panel) and 105 (right panel) degrees respectively.

We now shift our attention to the small scale features that are clearly visible on the lower part of the 3.95 Tesla scan in Figure 3-3. Figure 3-4 shows a 4×4 μm zoomed-in SCA image of this lower region. The feature consists of two narrow concentric arcs of high SCA signal marked A and B. They are separated by a wide dark band and one can also discern traces of two additional concentric arcs C and D. The boundary that separates these structures from the $\nu < 4$ exterior is also well-defined.

The evolution of the SCA signal in the central 2×2 μm region as a function of magnetic field, appears in Figure 3-5. Arcs A and B increase in size with decreasing field while keeping approximately the same aspect ratio. One may also identify other features evolving with field but we will ignore them for now since it is hard to quantify their description.

3.4 Origin of Contrast in Charge Accumulation Imaging

Before focusing on the specific features in the images, we discuss about the origin of contrast in our scans.

The observed changes in the recorded SCA signal may be caused from spatial variations in the compressibility of the 2DES (some regions of the 2DES can absorb more charge than others) or they may be due to differences in local charging rates (thus reflecting local resistivity features of the system). In the first case, the sample charges in phase with the excitation according to its self-capacitance and local compressibility. In the latter one, the 2DES does not have enough time to fully charge during the period of the excitation and this manifests itself in a phase lagged measured signal. Due to the importance of these mechanisms in understanding our data, we will examine each one of them in some more detail.

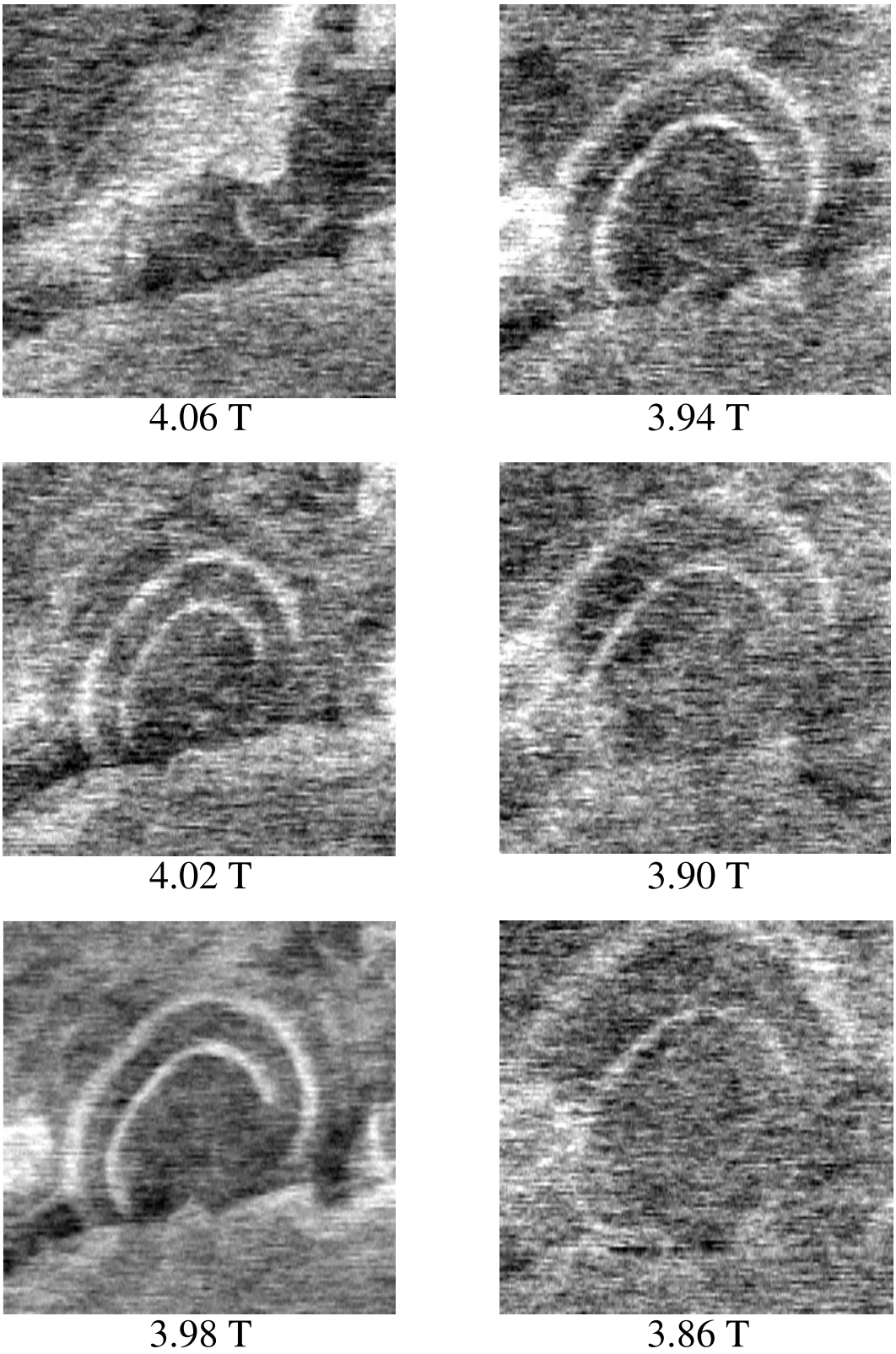

Figure 3-5: Sequence of 2×2 μm in-phase SCA images taken in the central region of Figure 3-4. The scan at 3.98 Tesla has been signal averaged for a longer time than the others, and its signal-to-noise ratio is thus higher.

3.4.1 Compressibility contribution

In our earlier introduction of the quantum Hall effect (section 1.2), we saw that the position of the Fermi level, has a direct effect on the properties of a 2D electron gas. If E_F lies within the central region of a disorder-broadened Landau level (i.e. within the region characterized by extended states), the density of states at the Fermi level is high and a small change in energy induces a large change in density. The electron system is then called compressible. When the Fermi level lies within a gap (region characterized by localized states), then a small change in energy has no effect since the DOS of current carrying states at E_F is zero. By analogy the system is then called incompressible.

The thermodynamic compressibility K is given by,

$$K = -\frac{1}{V}\frac{1}{\frac{\partial P}{\partial V}} \tag{3.1}$$

where P is the pressure and V the volume of the system under consideration. We may introduce the energy E using the relation $F = E - TS$ and the equation of state $P = -\left(\frac{\partial F}{\partial V}\right)_T$. The quantity F is the Helmholtz free energy. At $T = 0$, the equation of state is $P = -\frac{\partial E}{\partial V}$, and Equation 3.1 becomes:

$$K^{-1} = V\frac{\partial^2 E}{\partial V^2} \Rightarrow K^{-1} = n^2 \left.\frac{\partial^2 E}{\partial n^2}\right|_{T=0} \tag{3.2}$$

The quantity n denotes the density of the system. In our case, it is the areal density of the two-dimensional electron gas. We then use the definition of the chemical potential μ, $\mu = \left(\frac{\partial E}{\partial n}\right)_{T,V}$, to get:

$$K^{-1} = n^2\frac{\partial \mu}{\partial n} \tag{3.3}$$

There is thus a close connection between K and the underlying thermodynamic properties of the system, expressed through its density of states. So it is not surprising that the compressibility plays a fundamental role in theories of both the integer and fractional QHE [6, 7].

As it turns out, the SCA measurement technique is mostly sensitive to low values of K. Considering a parallel plate capacitor model, the finite compressibility of one plate modifies the geometrical capacitance $\frac{\epsilon A}{4\pi d}$ to give $C = \frac{\epsilon A}{4\pi d + \frac{\epsilon}{e^2}\frac{d\mu}{dn}}$ [37]. It immediately follows that low compressibilities (high $\frac{d\mu}{dn}$) have a strong influence on C. For high compressibilities, when $\frac{4\pi de^2}{\epsilon} >> \frac{d\mu}{dn}$, the signal ceases to be sensitive to variations of $\frac{d\mu}{dn}$. As a result, our data may provide information about the 2DES that is not readily available from transport studies. A wide range of experimental methods has already demonstrated the advantages of thermodynamic over transport measurements [43, 44, 36, 45, 46, 37].

3.4.2 Resistivity contribution

Differences in local conductivity and pathways for charging in the 2DES may lead to different local charging times. As a consequence, certain regions may charge and discharge fully during the a.c. excitation period, whereas others may do so only partially.

A simple approach to the 2DES is to consider it as a lumped RC system, where R is the resistance of the layer and C_{self} is its self-capacitance. The tip senses the charge at the junction of R and C_{self} through a coupling capacitance as depicted in Figure 3-6(a). For our "plain" 2DEG of area $\approx 5\ mm^2$, C_{self} completely dominates over $C_{coupling}$. In Chapter 5 however, we shall see that the situation reverses: $C_{coupling}$ becomes the relevant quantity since we are then probing smaller 2DEG areas with much lower self-capacitance. So, for now, let $C_{self} \equiv C$ for simplicity. It is easy to show that the in-phase and 90° phase lagging components of the measured voltage V_{out} are given by:

$$V_{out,X} \sim \frac{1}{1 + (\omega RC)^2} \tag{3.4}$$

$$V_{out,Y} \sim \frac{\omega RC}{1 + (\omega RC)^2} \tag{3.5}$$

Figure 3-6 plots the frequency dependence of these signals. In our experiment, the

resistivity of the sample varies as a function of magnetic field and becomes extremely large at integer filling. At these fields, the roll-off frequency $f_0 = \frac{\omega_0}{2\pi} = \frac{1}{2\pi RC}$, may approach the excitation frequency of 100 kHz. As a result, we detect both $V_{out,X}$ and $V_{out,Y}$ components; the signal displays a non-zero phase shift. The behavior is qualitatively simple to understand. At low frequencies, charging occurs rapidly compared with the period of the excitation; the measured signal is in-phase with the excitation V_{in} and $V_{out,Y}$ is small. At intermediate frequencies, the charge lags V_{in} and $V_{out,Y}$ is large. At high frequencies, little charge enters the sample, so both the in and out-of-phase signals are strongly diminished.

A more elaborate model treats the 2DES as a distributed RC system with spatially varying compressibility and in-plane conductivity (σ_{xx} and σ_{xy}) as Figure 3-8 shows. Numerical simulations may then be used in an effort to extract values for the relevant parameters of the system. In this case, unlike the lumped RC model, there is no unique roll-off frequency. To understand this qualitatively, consider a region of size L ranging from the size of the sample (several millimeters) to the resolution limit given $L_{min} \approx 100nm$. Given a sheet of uniform resistivity in two-dimensions, the effective resistance of this region does not depend on its size, but its self-capacitance increases linearly with L. Consequently, the roll-off frequency depends on the size of the region in question as $f_0(L) = \frac{1}{2\pi RL}$. $f_0(L)$ increases as L diminishes. Therefore, when the roll-off frequency $f_0(L_{max})$ becomes of the order of the measurement frequency, the charging of smaller length scales still behaves as in the low frequency limit, and features charge in phase with their surroundings. As a result, only compressibility features appear at small length scales.

The data presented in section 3.2 are most likely related to the onset of the quantum Hall regime in the 2DES. The structures are only seen when the magnetic field is tuned near the Hall plateau, and most importantly, features redevelop when the field increases by a factor of 2, corresponding to the $\nu = 2$ plateau. Although the similarity between 3.00 T and 6.00 T is not exact, one may identify structures (especially the narrow "filaments" near the top of the image) that reproduce. The data for these fields is shown in Figure 3-7.

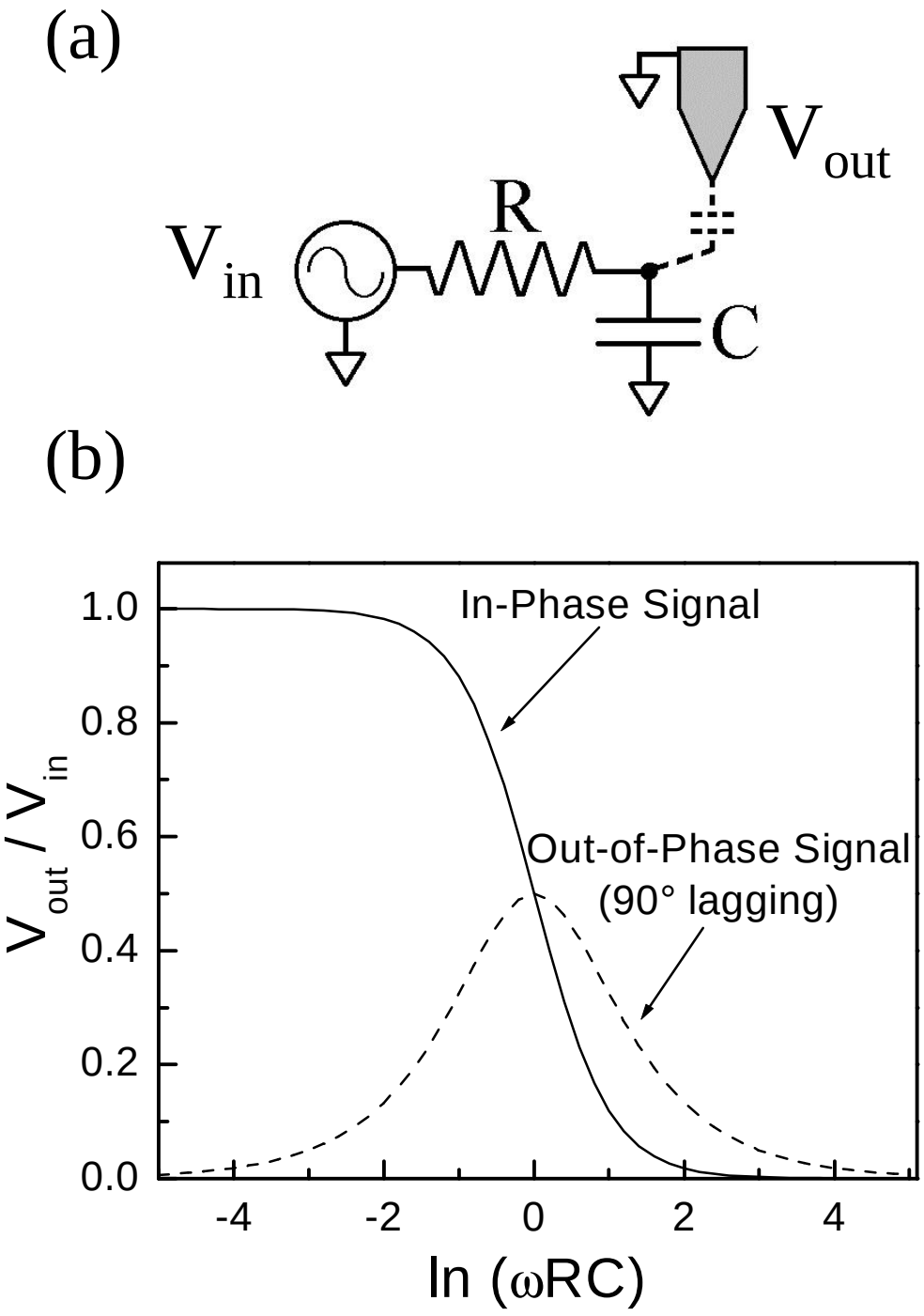

Figure 3-6: Simplified RC charging model for our 2DES. (a) Schematic of the circuit. (b) Dependence of the in-phase and out-of-phase measured signal on the model parameters.

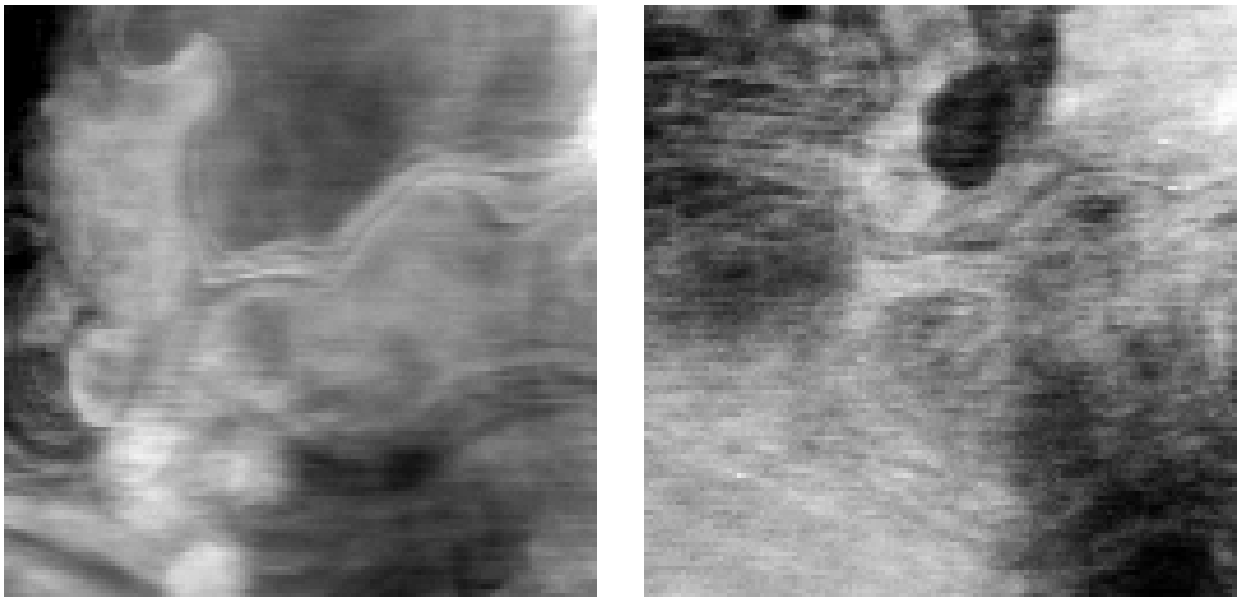

Figure 3-7: In-Phase SCA images ($3.3 \times 3.3\ \mu m$) at 3.000 T corresponding to $\nu = 4$, and 6.000 T corresponding to $\nu = 2$ filling factor. Images at fields away from integer Landau level filling (not shown), display no contrast.

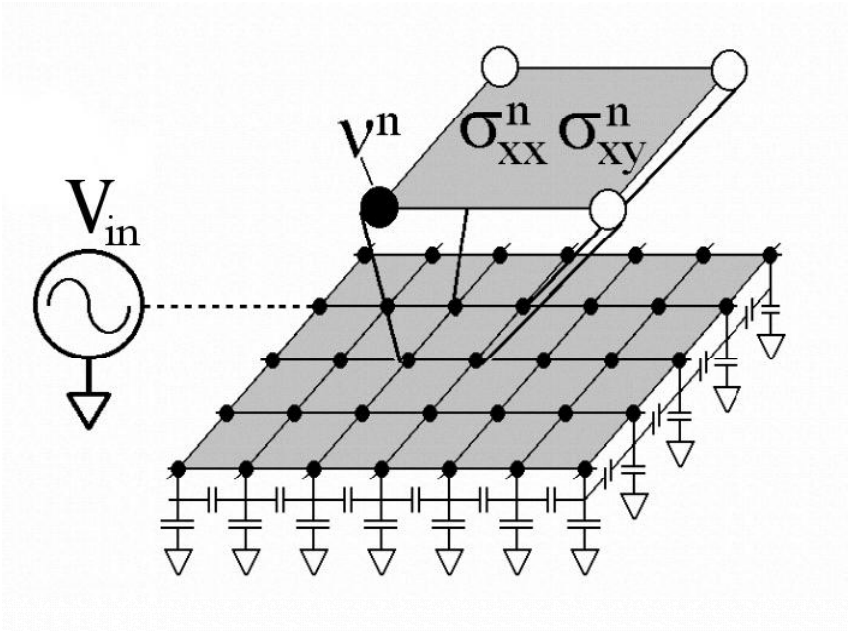

Figure 3-8: Schematic of distributed RC charging model for our 2DES.

It is particularly difficult to deduce the nature of the observed features with certainty and allow for precise predictions that may relate to a particular theoretical model. The data in section 3.2 constitute some of our first measurements with the newly-built microscope. It is possible that the tip-sample electric field was not completely eliminated and debris on the tip resulted in a non-uniform work function difference between different regions of the apex of the tip and the sample. Therefore, based on more recent knowledge and experience about these effects (see section 6.3.3), some of the features (particularly the ones resembling arcs and filaments) observed in Figure 3-2 may be artifacts resulting from the tip locally perturbing the sample. Larger "zoom-out" scans of the region containing these features could have probably shed some more light on their origin, but such data were not obtained at the time of the measurement.

However, care has been taken so that the above-mentioned shortcomings are not present in the experimental data described in section 3.3. We have already seen that variations in the SCA measured signal may be due to underlying resistivity or compressibility features in the 2DEG. The out-of-phase image shown in the left panel of Figure 3-4(b), contains all the main features as the in-phase image in panel (a). By properly changing the reference phase of the signal, we can leave all the arc-shaped features in the in-phase image while eliminating them from the phase-lagged image. The only exception is the $\nu = 4$ boundary delineating the original dark spot. This boundary cannot be eliminated by the 15° phase shift performed in the right panel of Figure 3-4(b) and is thus quite resistive. In contrast, the arcs themselves reflect mostly local variations of compressibility.

In order to examine the possible microscopic origin of these structures, one has to explain clumping of the electron density in a 2DES where the main interaction between electrons is Coulomb repulsion. In some cases the exchange interaction between electrons can overcome the direct density-density interaction and change the effective force from repulsion to attraction. There are several models that predict a non-monotonic density profile at the edge of the 2DEG in the QHE. Chamon and Wen [47] and MacDonald [48] have described such a charge structure forming at the

presence of a density gradient. For a range of the confining potential strengths, the edge undergoes a reconstruction similar to a situation that occurs in quantum dots [49]. A redistribution of electrons between Landau levels leads to the creation of alternating conducting and insulating regions in the electron layer. The length scale of this formation is of the order of the magnetic length $\ell_B = \sqrt{\frac{\hbar c}{eB}}$ which is the typical width of the electron's wavefunction in its orbit. At 4 Tesla, $\ell_B = 130$ Å which is significantly different than the separation between arcs ($\sim 2000 - 4000$ Å) observed in our experiment.

Koulakov, Fogler and Shklovskii [50, 51] have studied the ground state of a 2DEG with partially filled higher Landau levels. Using the Hartree-Fock approximation, they predicted that electrons in these levels should form a unidirectional charge density wave with a period of the order of the classical cyclotron radius, $\lambda \approx 3R_c$. Again, it is difficult to relate the observed spacing of our features in Figure 3-5 with the expected value of ~ 1000 Å for λ. As a result, although it is tempting to describe the data as a pinned CDW according to ideas presented in [50, 52], one requires more experimental measurements in order to prove or disprove this connection. In closing, let us also note that recent transport measurements [53, 54, 55] have revealed a surprising anisotropy of the longitudinal conductivity of the 2DEG at filling factors above $\nu = 4$. The complete interpetation of these results is still uncertain but most likely involves the formation of a CDW similar to the situation described above.

3.5 Conclusion

The results presented in this chapter have showcased the SCA microscope's ability to probe 2-dimensional electron systems and image quantum Hall features with a resolution of ≈ 100 nm. We have also seen how the measured signal arises from the interplay between compressibility and conductance variations in a 2DEG. This fact will prove very important in understanding and interpreting the results presented in the following chapters. Armed with this knowledge and experience concerning the specifics of the instrument's operation, we proceed to present data that quantitatively

probe 2D electron systems under a wide range of experimental conditions.

Chapter 4

Low-Compressibility Strips in the Quantum Hall Liquid

The edge state picture of transport in a 2-dimensional electron gas in a strong magnetic field, can explain several key properties of the 2DEG in the quantum Hall regime [7, 56]. The intersection between the constant Fermi energy and the Landau-level energy near the edge of the electron system determines the spatial location of the edge states. In a self-consistent electrostatic picture, edge channels are separated by incompressible strips of integer Landau level filling. Resulting models involving alternating compressible and incompressible strips have received considerable theoretical [57, 58, 59, 60] and experimental attention [61, 62, 63, 64].

Most conventional experiments that involve transport and optical measurements of 2D systems, probe the relevant quantities averaged over the entire macroscopic sample. They thus provide little information about the underlying microscopic behavior which remains controversial. Local imaging scanning techniques can directly probe semiconductor systems and reveal the microscopic structure of compressible and incompressible strips [65, 40, 66]. The use of Charge Accumulation Imaging for such investigations [64] is the subject of the present and the following chapter.

We begin this chapter by giving an introduction to the edge states and incompressible strips in the QHE, and then proceed to describe our method and experimental results.

4.1 Edge States in the Quantum Hall Liquid

As we have seen in previous chapters, a perpendicular magnetic field quantizes the energy levels of a 2-dimensional electron gas into the so-called Landau levels. In what follows, we shall examine the role of the system edges in the energy spectrum and the form of the resulting electronic states.

4.1.1 Single-electron picture

Near the edge of a sample, electrons are subject to a confining potential that is assumed to be smooth on the length scale of the magnetic length $\ell_B = \sqrt{\frac{\hbar c}{eB}}$ (a measure of the electronic wavefunction spatial extent). In a simplified non-interacting electron picture, the confining potential bends the Landau levels near the edge, and states in this region have higher energy than those in the middle of the sample as drawn in Figure 4-1(a). The states at the constant Fermi level are precisely what one refers to as edge states, with their location given by the intersection between E_F and the corresponding Landau level energy.

From the solution of Schrödinger equation in the presence of a magnetic field using the Landau gauge $\mathbf{A} = (0, -By, 0)$, one gets that 2D-electronic wavefunctions are centered around positions x where $x = -k\ell_B^2$. These are exactly the centers of the circular cyclotron orbits, around which electrons move according to a semi-classical treatment of the problem. The x-coordinate in Figure 4-1(a) may thus be equivalently replaced by the wavevector k. The electronic group velocity is given by:

$$v = \frac{1}{\hbar}\frac{\partial E_k}{\partial k} \tag{4.1}$$

It follows that the quantity $\frac{\partial E_k}{\partial k}$ and hence the velocity v, both carry different signs at the two edges. As a result, edge states on opposite sides of the sample move in opposite directions.

Semi-classically, electrons are subject to the Lorentz force and their orbits in the bulk of the 2DEG are closed circles as shown in Figure 4-1(c). This circular motion is

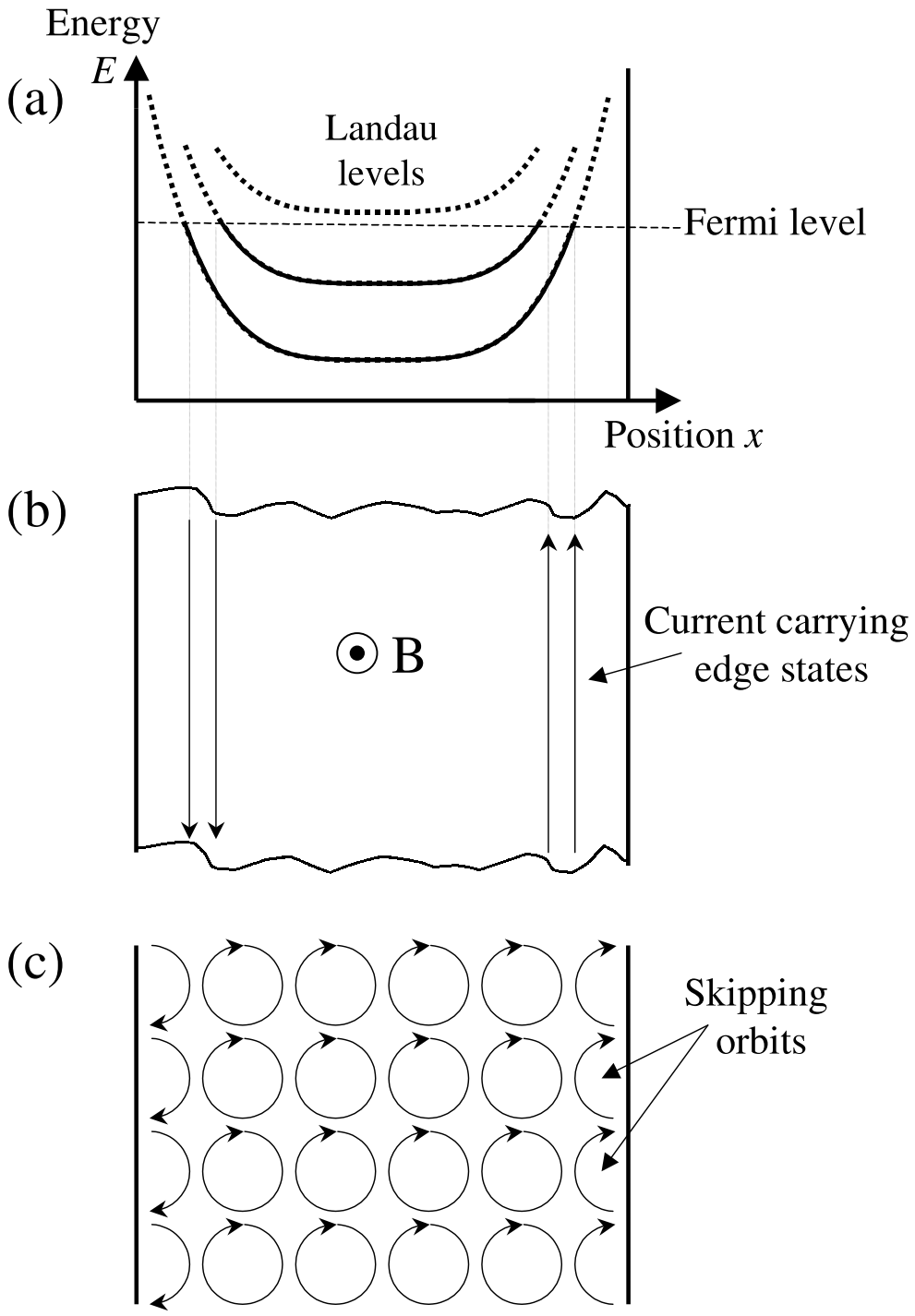

Figure 4-1: (a) Energy versus position of a 2D electron gas in the presence of a perpendicular magnetic field. Electronic states in Landau levels are filled up to the Fermi level. (b) Edge states formed near the sample edges carry currents in opposite directions. (c) Semi-classically, current is carried by skipping orbits near the edge.

interrupted when an electron hits the boundary and the result is the skipping orbits near the edge. In contrast to "full" orbits in the middle, skipping orbits carry a net drift current along each edge. As we saw earlier, this current flows on opposite directions along opposite sides. So, in the absence of any externally applied potential, the overall current through the system is zero.

The situation changes when a finite chemical potential difference is set up between the two edges. Assuming that there are ν edge states originating from ν occupied Landau levels in the bulk, we have for the net Hall current:

$$I = \nu \frac{e}{h}(\mu_R - \mu_L) = \nu \frac{e^2}{h} V_H \tag{4.2}$$

where $V_H = \frac{\mu_R - \mu_L}{e}$. The transverse (Hall) resistance thus assumes the well-known values $R_H = \frac{h}{\nu e^2}$. If the Fermi level lies in the gap between Landau levels, states on the two edges are well separated and scattering between them is negligible due to vanishing bulk conductivity [67, 68]. This fact helps maintain the quantization in R_H. Moreover, the presence of localized states (due to disorder) in the gap, gives rise to the respective quantum Hall plateau (Figure 1-1). From the above discussion we see the strength of the edge state picture in providing a natural explanation of the QHE [3, 69, 70]. This general picture is now widely accepted as a basic ingredient for the understanding of the quantum Hall effect.

4.1.2 Self-consistent electrostatic treatment

The series of Landau levels in the density of states leads to a periodic variation in the screening properties of the 2DEG, from no screening at integer filling factors $\nu \equiv n$ to very strong screening at non-integer ν. The result is a series of compressible (conducting) and incompressible (insulating) regions near the edge of the sample, where the presence of a density gradient causes spatial differences of the filling factor.

The positions and widths of these strips in the presence of a density gradient, have been determined electrostatically by Chklovskii, Shklovskii and Glazman [60]. They suggested that due to the cyclotron gap between neighboring Landau levels, it

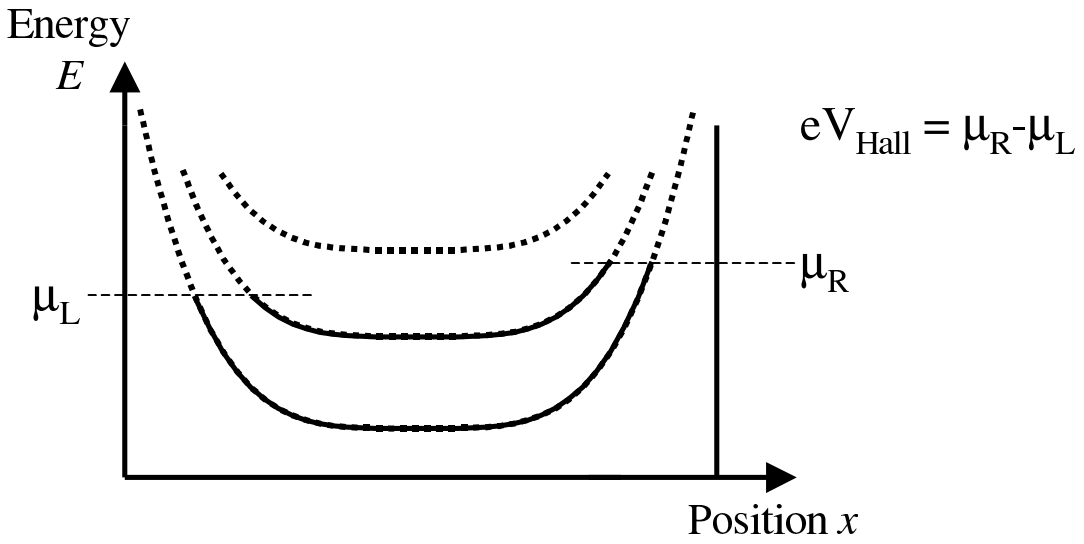

Figure 4-2: Finite potential difference between the two edges in a 2DEG. Edge states on the right carry more current than the ones on the left. The result is a net longitudinal current in the sample.

is energetically favorable to move electrons from level $n+1$ to level n as depicted in Figure 4-3(a). The result is a flat region in density that exactly satisfies the condition for the $\nu = n$ integer filling. The lower schematic in Figure 4-3(a), shows the corresponding potential energy in the vicinity of this region. The system moves from a low-density region where $\nu < n$ (i.e. the n Landau level is partly full), to a high-density region where $\nu < n+1$ (i.e. the n level is filled and the $n+1$ level is partly full). Both these areas are compressible. The potential energy step between them, is the cyclotron energy $\hbar\omega_c$. The overall profile is similar to that of a p-n junction whose depletion region corresponds to an incompressible strip at filling factor ν. The width of that strip can be approximately determined by equating the potential drop $\frac{\hbar\omega_c}{e}$ across it, to the product of the electric field $e\frac{dn}{dx}\frac{w}{\epsilon}$ inside it times its width w. A more exact calculation gives [60]:

$$w^2 = \frac{2\epsilon\hbar\omega_c}{\pi^2 e^2 dn/dx} \tag{4.3}$$

The requirement for a density gradient is naturally satisfied near the edge of the 2DEG where the electronic density varies from zero to its bulk value inside the sample. The resulting incompressible and compressible strips are shown schematically in

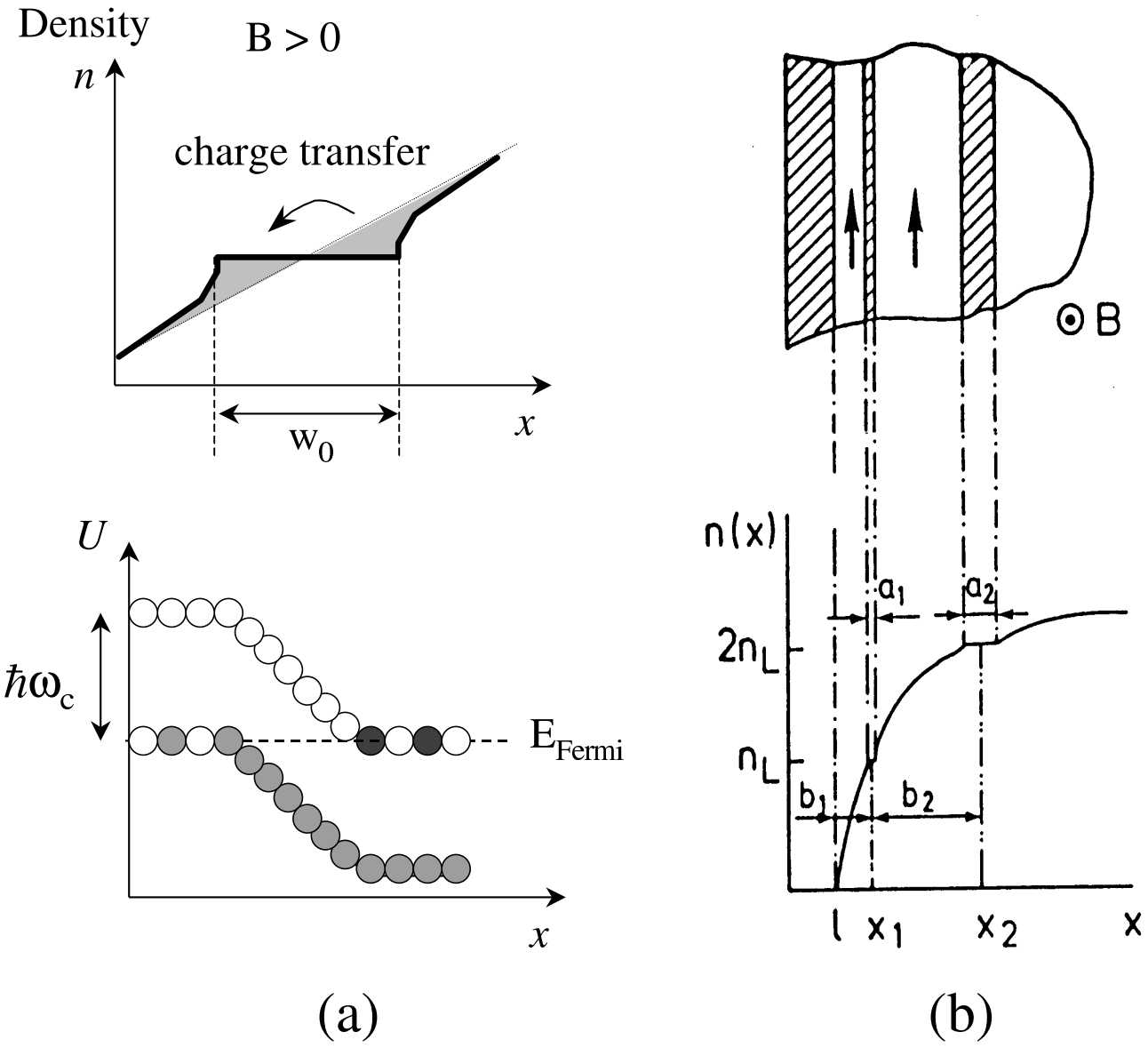

Figure 4-3: (a) An incompressible strip forms at a location where the electronic density exactly fills a Landau level. (b) Series of compressible and incompressible strips near the edge of a 2DEG. This schematic is taken from Reference [60].

Figure 4-3(b) that is taken from Reference [60]. However, the experimental results that we are going to present in this chapter, are based on density gradients that we artificially create inside the 2D electron system. This is the subject of the next section.

4.2 Creating and Characterizing a Density Gradient in a 2DEG

We use our scanning probe microscope to study a two-dimensional electron gas that is formed at a GaAs/AlGaAs interface, 90 nm below the semiconductor sample surface. The electron density is $\approx 3.5 \times 10^{11} cm^{-2}$ and the mobility is $\approx 4 \times 10^{5} cm^{2} V^{-1} s^{-1}$ The layer structure of the heterostructure samples used in this work, is the one shown in Figure 2-1.

We proceed to create a density gradient in the bulk of the 2DEG by locally perturbing the charge distribution in the sample. In order to achieve this, a d.c. voltage of +2 to +3.5 Volts is applied between the scanning probe and the 2DEG for $\sim$ 30 seconds, with the tip brought in close contact with the surface. The injected tunneling current results in an increase of the 2DEG density, in a region that extends laterally a few microns from the tunneling site. The electron density at the center of the perturbation is typically about 20% higher than the bulk value, and we find that this density profile remains unchanged with time after the tunneling current is switched-off. The local modification of the electron density is most likely due to electron transfer from the donor layer to the 2DEG, similar to the persistent photoconductivity effect [71].

Kelvin probe imaging proves to be a very useful tool in our disposal, as it helps us to determine quantitatively the extent of the perturbation. As described in detail in section 2.4.3, we mechanically vibrate the sample in the vertical direction with a frequency of 2 kHz and an amplitude of $\sim$ 10 nm. The electrostatic potential difference ΔV between the scanning tip and the sample induces an oscillating charge

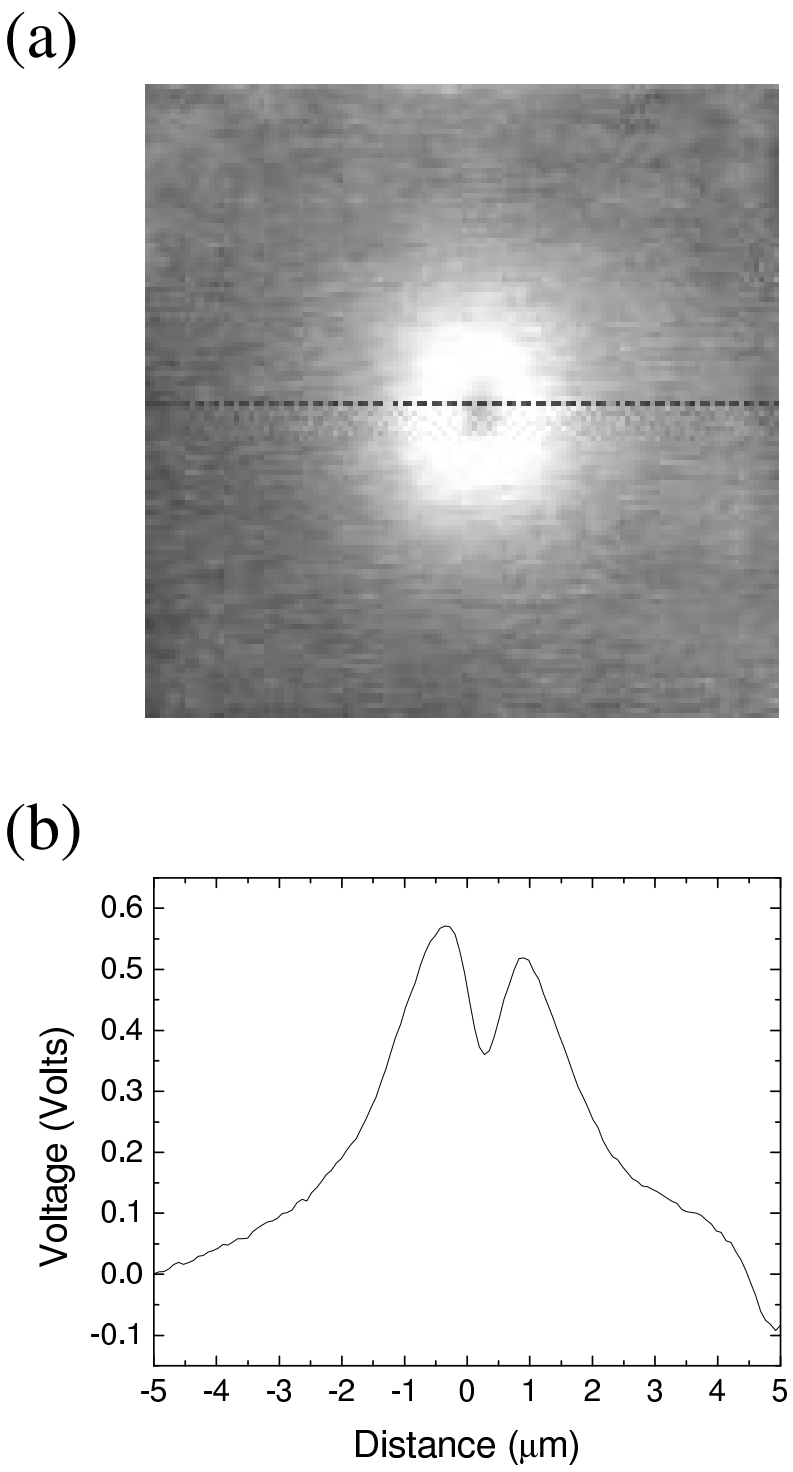

Figure 4-4: (a) 10×10 μm scan of a GaAs/AlGaAs heterostructure in Kelvin probe mode. The imaged region has been perturbed on purpose with the use of tunneling current. The resulting charge (or equivalently, electrostatic potential) distribution reflects the almost circularly symmetric density gradient that has been created in the 2DEG. (b) Calibrated Kelvin probe signal along the dashed line in part (a).

on the tip, which we measure with a lock-in amplifier. To calibrate the sensitivity of the measurement to potential differences, we proceed as follows: We first change the (bias) voltage between the 2DEG and the tip and record the resulting change in the Kelvin signal. We then position the scanning tip well outside the perturbed region and balance the Kelvin signal by applying a d.c. voltage between the 2DEG and the tip. This procedure nulls the electric field created by the work function difference between the two materials. However the Kelvin signal reappears upon placing the scanning probe above the perturbed region, due to the non-uniform charge distribution in the sample donor layer. Using the known sensitivity of our measurement to the potential difference, we map the electrostatic potential by scanning just above the sample surface.

Such a scan in Kelvin probe mode appears in Figure 4-4(a). The perturbation caused by tunneling extends symmetrically outwards from the point where the tunneling event occurred. Figure 4-4(b) plots the signal from a line through the center of the scan. The signal is proportional to the deviation of electron density from the unperturbed (i.e. bulk) value and reaches a maximum of $\Delta V \approx 0.5V$ close to the center of the perturbed region. The small dip at the center is related to the particular realization of the density gradient and is not relevant in our study. We shall thus ignore it in our discussion.

In section 4.3 we use the results from SCA measurements to determine the density enhancement as $\Delta n = 1 \times 10^{10} cm^{-2}$. We can also estimate Δn by assuming that the Kelvin signal arises from the transfer of electrons from the donor layer to the 2DEG. Taking the distance between the typical donor atom and the 2DEG as $s \approx 50nm$ we get that:

$$\Delta V = \mathcal{E} s = \frac{4\pi e \Delta n}{\epsilon} s \Longrightarrow \Delta n = \Delta V \frac{\epsilon}{4\pi e s} \tag{4.4}$$

This gives $\Delta n \approx 5 \times 10^{10} cm^{-2}$. This result is larger than the value obtained previously and probably indicates that most of the charge is transferred within the donor layer and not from the donor layer to the 2DEG. This extra charge contributes to the Kelvin signal, but does not change the 2DEG density. In general, it is not easy to determine

the precise charge balance within the various layers of the sample contributing to the Kelvin signal.

4.3 Imaging Incompressible Strips as Density Contours

We employ the subsurface charge accumulation (SCA) imaging technique to measure the charge distribution in areas of a 2DEG where an electronic density gradient has been established as detailed above. This charge is driven by an external a.c. excitation that is directly applied to the 2D electron gas. The excitation frequency is 100 kHz unless noted otherwise. Capacitive coupling between the scanning probe and the sample allows us to detect the charge that accumulates in the 2D layer both in-phase and 90° lagging from the excitation. A detailed account of the technique appears in section 2.4.1. All measurements are performed at a temperature of 0.35 Kelvin.

SCA measurements performed at zero magnetic field do not show any structure in the region of study, despite the induced density perturbation. At zero field, the 2DEG compressibility does not depend on electron density and the conductivity is high enough so that the sample charges fully during the excitation cycle. The situation changes when we apply a large magnetic field. Figure 4-5 shows a 10×10 μm SCA image at 4.15 Tesla. The scanned region is exactly the same as the one in Figure 4-4, and hence the aforementioned density gradient is present in the 2D electron layer underneath the surface. A ring-shaped feature of lower signal appears in the image in-phase with the excitation. At the same time, the out-of-phase SCA image is mostly featureless. To understand these characteristics we should recall that when the scanning probe is located just above an incompressible (insulating) region, it will not record any signal since the 2DEG below will not charge and discharge with the weak a.c. excitation. In addition, the absence of out-of-phase signal confirms that the contrast seen in the in-phase images is due to compressibility variations in the 2DEG (see section 3.4).

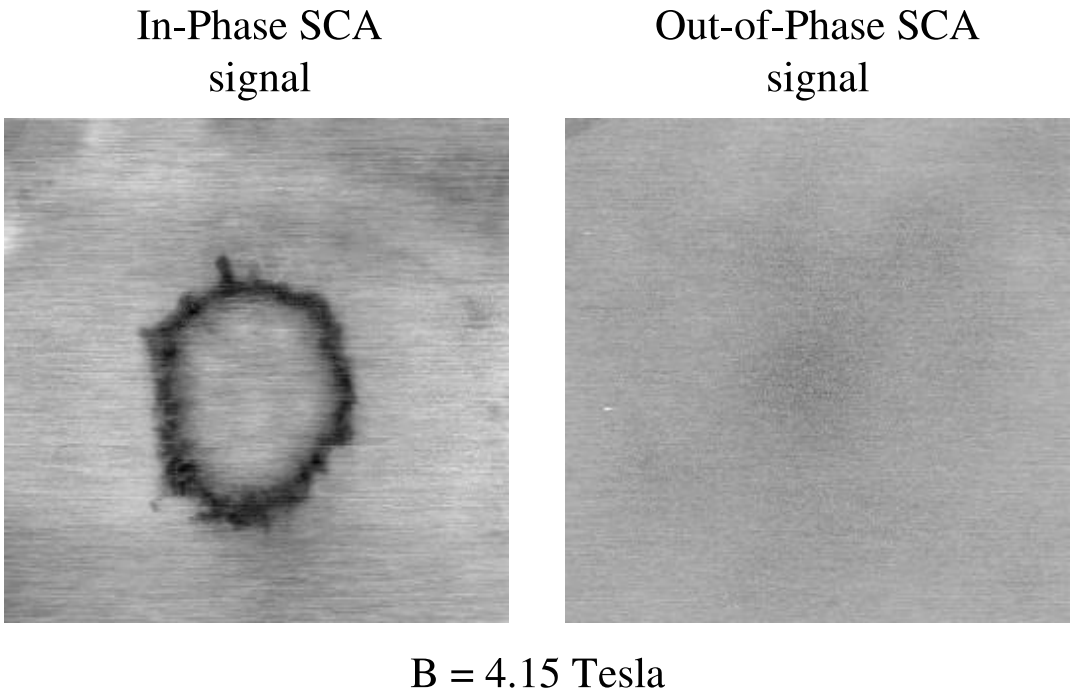

Figure 4-5: In and out-of-phase SCA images of the same 10×10 μm area, as the one imaged in Kelvin probe mode in Figure 4-4. The measurements are taken at a magnetic field of 4.15 T.

The $\nu = 4$ filling factor is reached at 3.5 Tesla in the bulk of our sample. We thus attribute the region of low SCA signal in Figure 4-5 to an incompressible (or more accurately as we will later see, low-compressibility) strip at $\nu = 4$. The strip forms in the region where the electronic density satisfies the condition for exact filling of the $\nu = 4$ Landau level filling factor. Figure 4-6 follows the evolution with magnetic field of the signal measured across the center (y=0) of the scan window, i.e. across the diameter of the ring. The position of the strip is indicated by an arrow. As the field increases, the diameter of the ring shrinks, moving towards the center of the perturbed area. Additional measurements taken on different regions of the sample (prepared in the same manner) appear in Figures 4-8, 4-9 and clearly illustrate this behavior. At even higher fields the charging signal in the interior of the ring drops, forming a circular depression in the SCA signal (two lower curves in Figure 4-6, Figure 4-9). We will further discuss the origin of this latter effect in section 4.5.

The reduction in the ring diameter can be explained in the following way. With increasing magnetic field, the degeneracy of the Landau levels increases and the con-

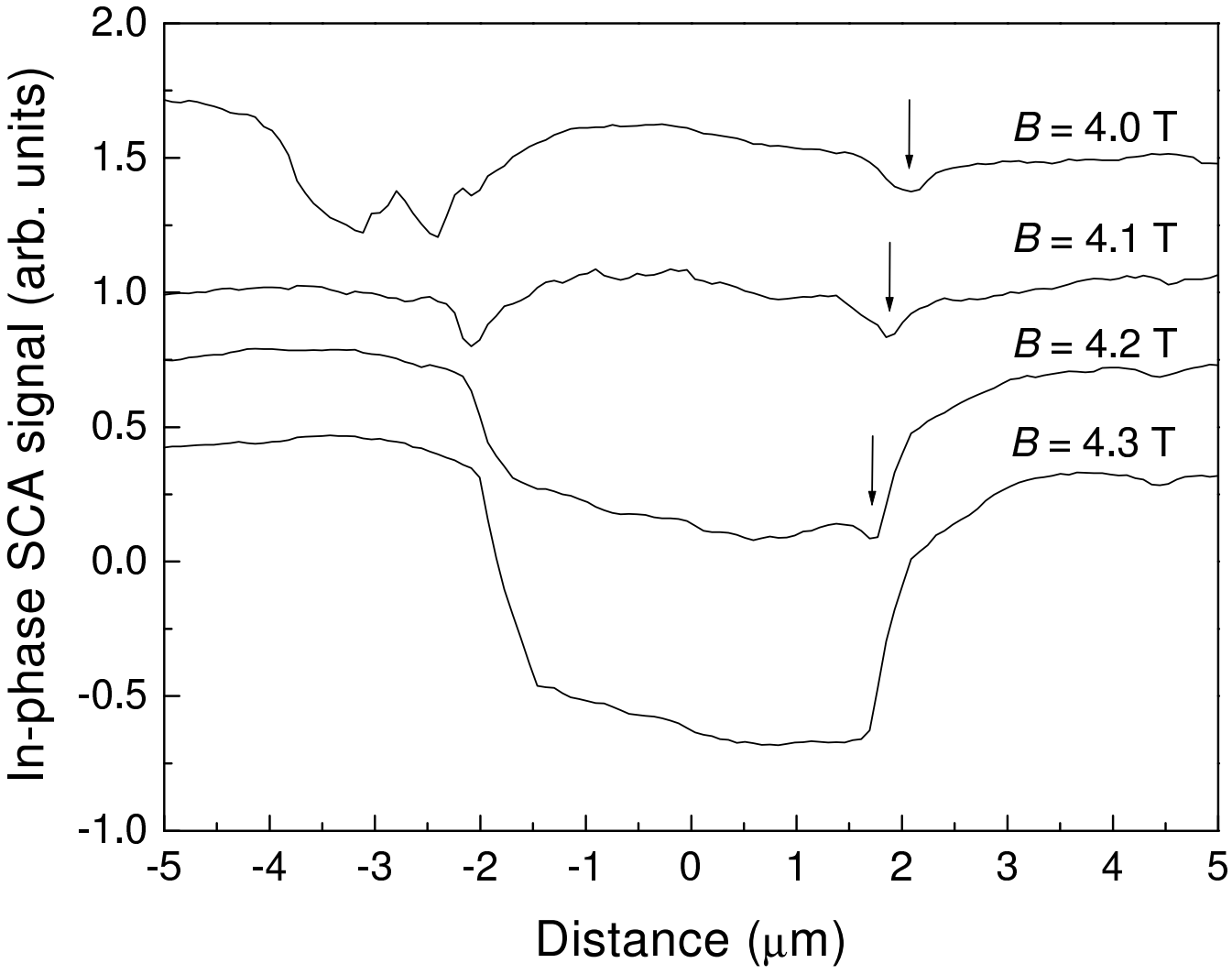

Figure 4-6: Evolution of SCA line scans (in-phase signal) with magnetic field. The arrows point to depressions in the signal resulting from the formation of an incompressible strip.

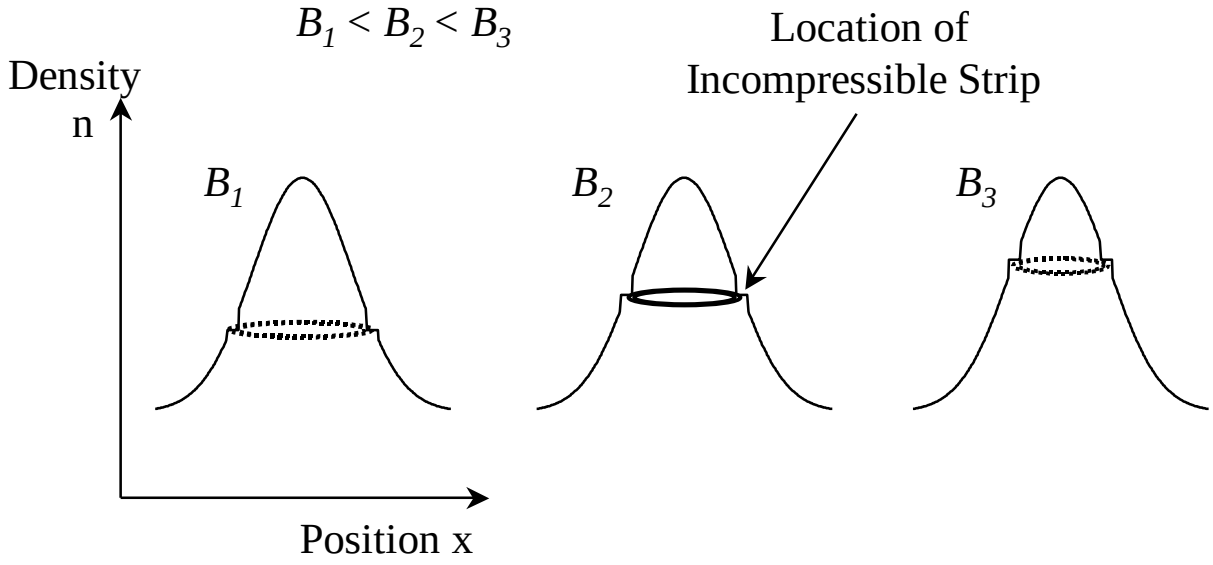

Figure 4-7: Incompressible strip location as a function of magnetic field B. As B increases the strip moves towards higher density regions along the artificially created gradient.

dition for integer filling will be satisfied at regions of higher electronic density. The strip thus moves up the density gradient and shrinks towards the center of the scan window (see schematic in Figure 4-7). Going back to Figure 4-6, the position of the $\nu = 4$ strip shifts by ≈ 200 nm as we step the magnetic field by 0.1 Tesla. At $\nu = 4$, this change in magnetic field corresponds to a $\Delta n = \nu \frac{\Delta B e}{hc} = 1 \times 10^{10} cm^{-2}$ change in the electron density (see Equation 1.4). We therefore estimate the magnitude of the electron density gradient $\frac{dn}{dx} \approx 5 \times 10^{10} cm^{-2} \mu m^{-1}$ in the case of Figures 4-4 and 4-5.

From the discussion in this section, it immediately follows that the observed strips effectively mark the contours of constant electron density in the 2DEG and they serve to separate regions characterized by different filling factors. For example, the ring in Figure 4-5 marks the boundary between areas where $\nu < 4$ (outside the ring) and areas where $\nu > 4$ (inside the ring). Moreover, the equivalence between the coordinate x and the wavevector k (section 4.1.1), makes the observed incompressible strips, real-space realizations of the Fermi surface in the 2D electron system.

4.4 Incompressible Strips at different Filling Factors

We have performed extensive measurements of strips corresponding to filling factors $\nu = 2$, $\nu = 3$, $\nu = 4$. Our ability to laterally translate the sample in our microscope gave us the flexibility to create and study a large variety of density gradients, each time starting with a new unperturbed 2DEG region. Our superconducting magnet can achieve a maximum field of 10.5 Tesla. Filling factor $\nu = 1$ is reached at ~ 14 Tesla in the bulk of our sample and hence, measurements at this filling were unattainable in this work.

We present some of our measurements at $\nu = 4$ in Figure 4-8. The location of the strip changes with increasing field and moves towards the center of the almost circularly symmetric density perturbation, as we explained in the previous section. SCA images at several filling factors from that same location are shown in Figure 4-10. The position of the strips is directly linked to the complete filling of an integer number of Landau levels. As a consequence, when increasing the magnetic field by e.g. a factor of two, we should observe the $\nu = 2$ strip at exactly the same location as the $\nu = 4$ strip. This is indeed the case, as demonstrated in this last figure.

We have already seen that Equation 4.3 gives a theoretical expression for the dependence of the strip width on magnetic field. We shall further pursue the comparison of the theoretical prediction with our experimental results in section 4.6.

Figure 4-9 contains measurements from yet another artificially perturbed 2DEG region, and shows both the in-phase and 90°-lagging signal. The information contained in the out-of-phase signal, helps us distinguish between the two dominant sources of contrast present in the images. This is the subject of the next section.

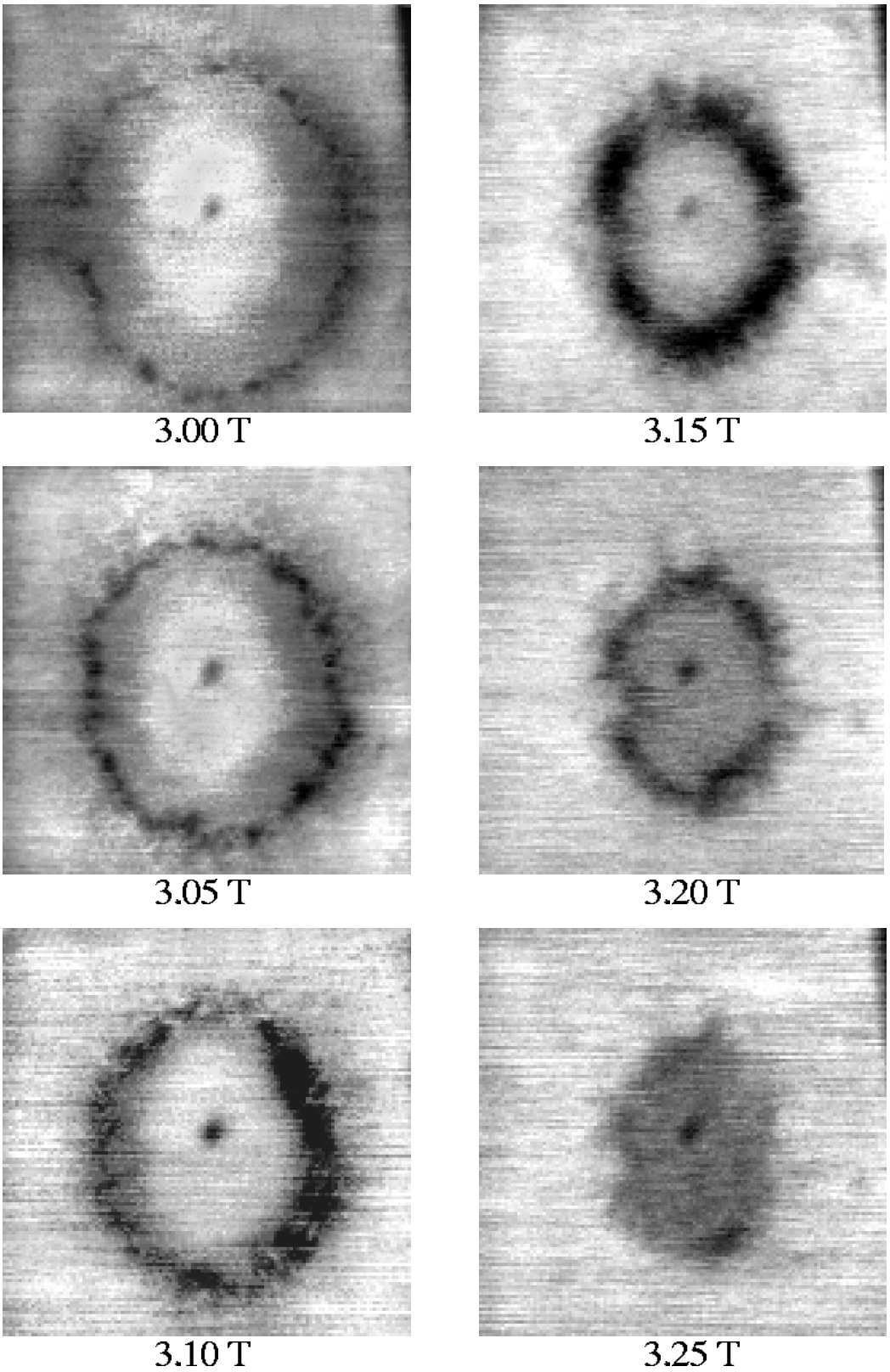

Figure 4-8: $14 \times 14\ \mu m$ in-phase SCA images as a function of magnetic field. A low compressibility circular strip forms in the 2DEG. The strip acts as a density contour moving towards areas with higher electronic density as the field increases.

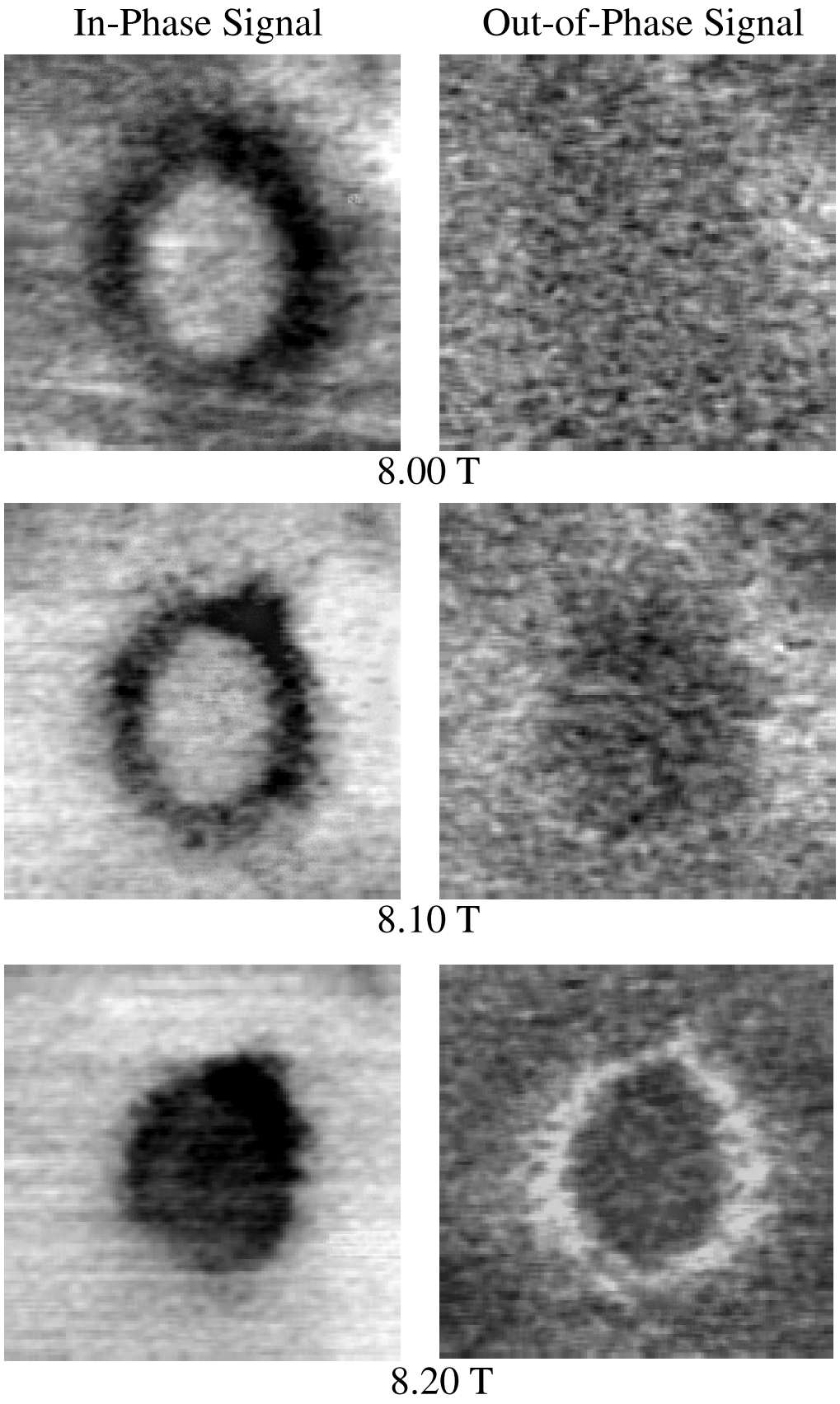

Figure 4-9: 13×13 μm in and out-of-phase SCA images for different magnetic fields near $\nu = 2$.

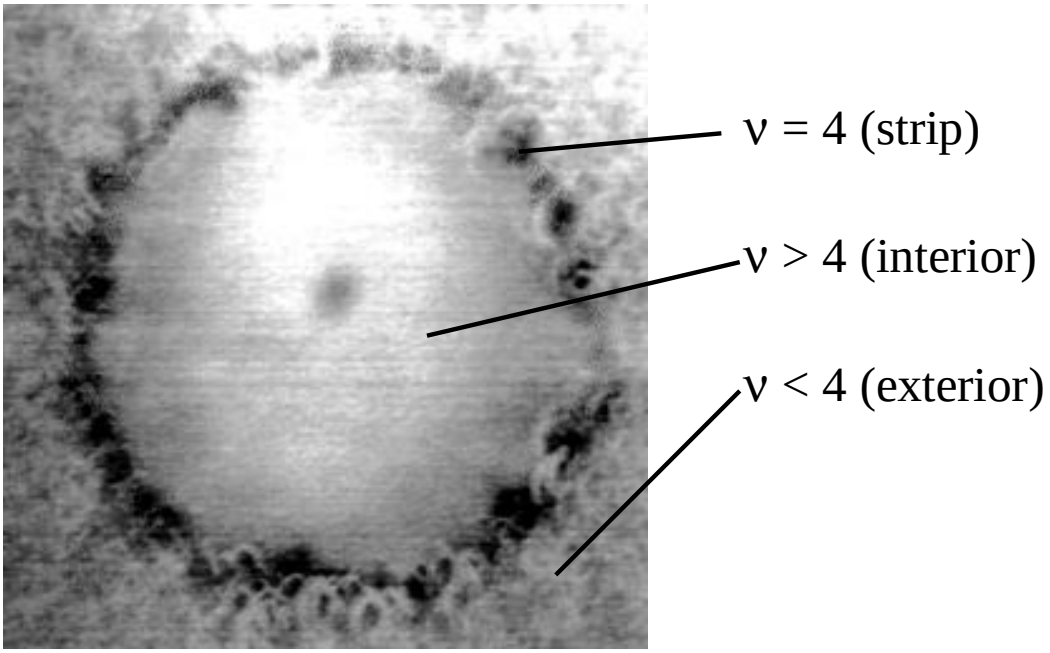

3.07 T (ν ~ 4)

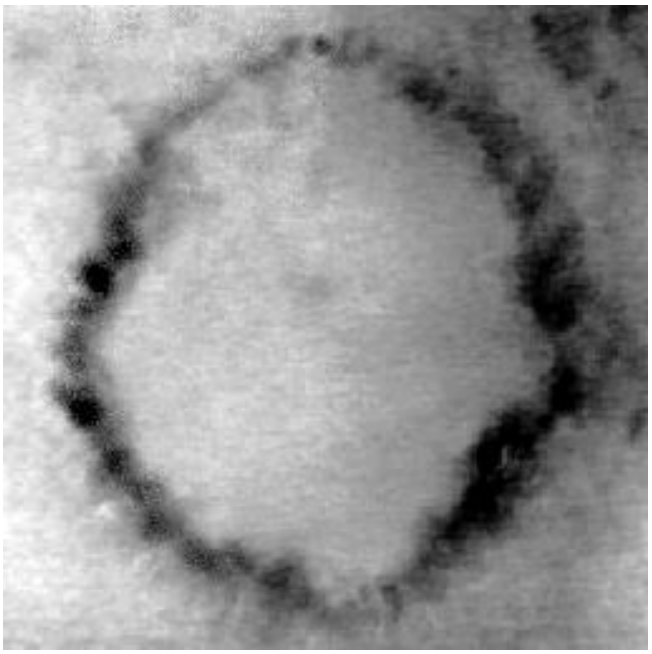

4.17 T (ν ~ 3)

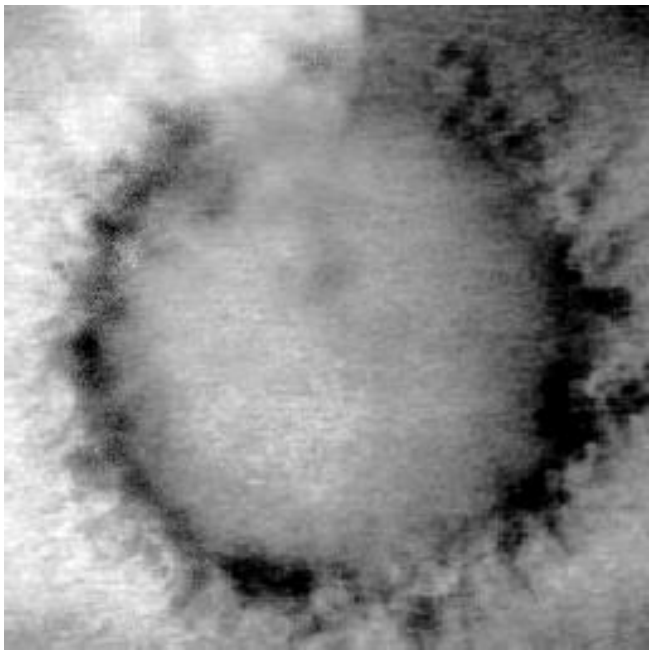

6.14 T (ν ~ 2)

Figure 4-10: Incompressible strips at $\nu = 2, 3$ and 4. The scans are 10.5×10.5 μm large. Magnetic field values are related between them by the ratio of the corresponding filling factors. The same value of electron density is required to fill the available Landau levels in each case, and as a result, strips of different ν appear at the same location.

4.5 Interplay between Compressibility and Resistivity

A suppression of the SCA signal at a certain region may be the result from either low compressibility or low conductivity. In the latter case there is insufficient time to charge the region during the period of the excitation. As the 2DEG longitudinal conductivity is very low in the vicinity of integer filling factors, this possibility must be carefully examined. To distinguish between the two mechanisms we study both the in-phase and out-of-phase (90° degree lagging) SCA signals as a function of frequency.

A negligible phase shifted signal and no frequency dependence were observed in measurements relating to the upper curve in Figure 4-6. This is evidenced in Figure 4-11 where the in-phase and 90° lagging SCA signals, all obtained at the same location and magnetic field, are measured at frequencies of 10, 30 and 100 kHz. As before, these plots are line-scans through the center of the perturbed region corresponding to Figures 4-4 and 4-5. We therefore conclude that the observed features reflect a suppressed 2DEG compressibility at integer filling factor.

However, there are cases where a phase shifted signal is present in our measurements. Typically, at higher magnetic fields, SCA features appear both in and out-of-phase from the excitation, demonstrating that the 2DEG does not have enough time to fully charge during the excitation cycle. Under conditions giving rise to a phase shift, a ring-shaped feature in the 90° lagging signal accompanies the circular region of suppressed in-phase SCA signal. This is clearly seen in the bottom panels of Figure 4-9. This pattern results from incomplete charging of the interior of the circle, through a poorly conducting strip of integer ν around it. The situation resembles an RC circuit with a variable R where the effective resistance increases as the scanning tip moves towards regions to the interior of the strip. From our analysis in section 3.4.2 we know that this causes the measured in-phase signal to steadily decrease to zero, while the 90° lagging signal first increases from zero, goes through a peak and then decreases back to zero level (Figure 3-6(b)). The peak is exactly the bright ring in the out-of-phase image at 8.20 Tesla in Figure 4-9. This ring effectively

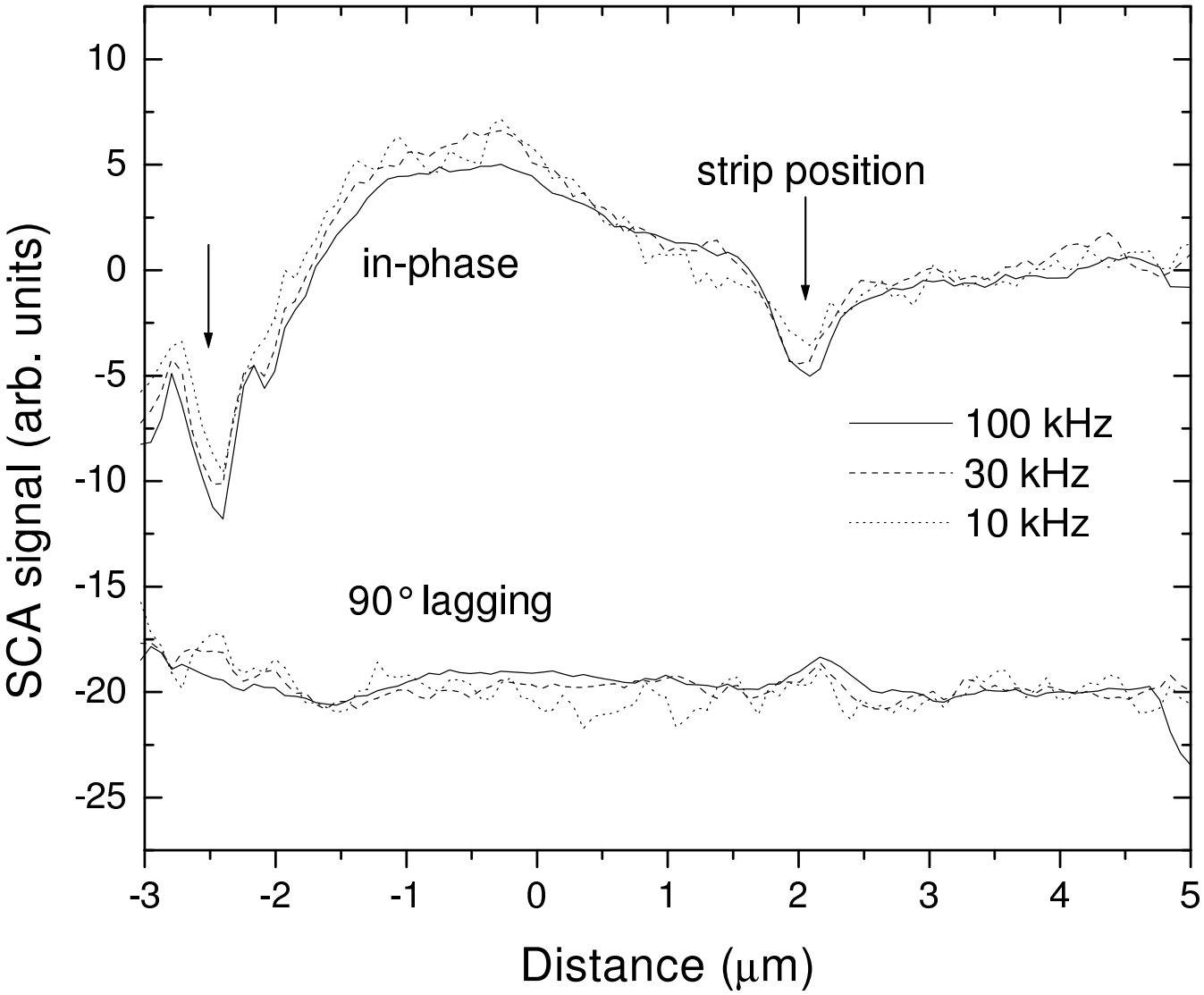

Figure 4-11: In-phase and 90° lagging SCA signals at three different frequencies around filling factor $\nu = 4$. The vertical scale is the same for all frequencies. There is practically no out-of-phase signal present in the measurements.

marks the boundary between charging and non-charging regions of the 2DEG. In such circumstances it is difficult to extract separately the conductivity and compressibility information from the signal. We are currently performing extensive numerical modeling that will allow us to obtain this additional information [72].

We have managed so far to identify the physical origin of most features present in our scans and we now proceed to extract quantitative information from our data. To this goal, we use the lowest curve of Figure 4-6 to estimate the sensitivity of the SCA measurement. At a magnetic field of 4.3 Tesla, the resistive strip at $\nu = 4$ prevents charging of the interior region while the exterior region charges fully due to the a.c. excitation that is applied to the electron layer. The difference in signal between fully charging and non-charging regions is taken as the measure of the degree of charging, S_0. We observe that the contrast in the strip location at 4.0 Tesla (upper curve in Figure 4-6) reaches only about $0.20S_0$. This situation is depicted in Figure 4-12 which reproduces the relevant curves. In what follows, we are going to examine the origin of this observation.

4.6 Density of States and Width of Low Compressibility Strips

The SCA signal is proportional to the capacitance C_{tip} between the tip and the 2DEG. We can crudely estimate the density of states D between Landau levels by approximating the scanning probe and the 2DEG as a parallel plate capacitor. The signal $S(x)$ at the strip location can then be expressed as [37, 73]:

$$S_{strip}(x) \propto C_{tip} \propto \frac{1}{\frac{d}{\epsilon} + h + \frac{1}{4\pi e^2 D}} \tag{4.5}$$

where $d = 90$ nm is the depth of the 2DEG and $h = 10$ nm is the distance between the scanning tip and the surface (see Figure 4-13). The signal in neighboring regions that charge well is $S(x) \propto \frac{1}{\frac{d}{\epsilon}+h}$. It then follows that $S_{strip}(x) \approx 0.25S(x)$, from where we get that the density of states (DOS) D at the strip location is approximately 30 times

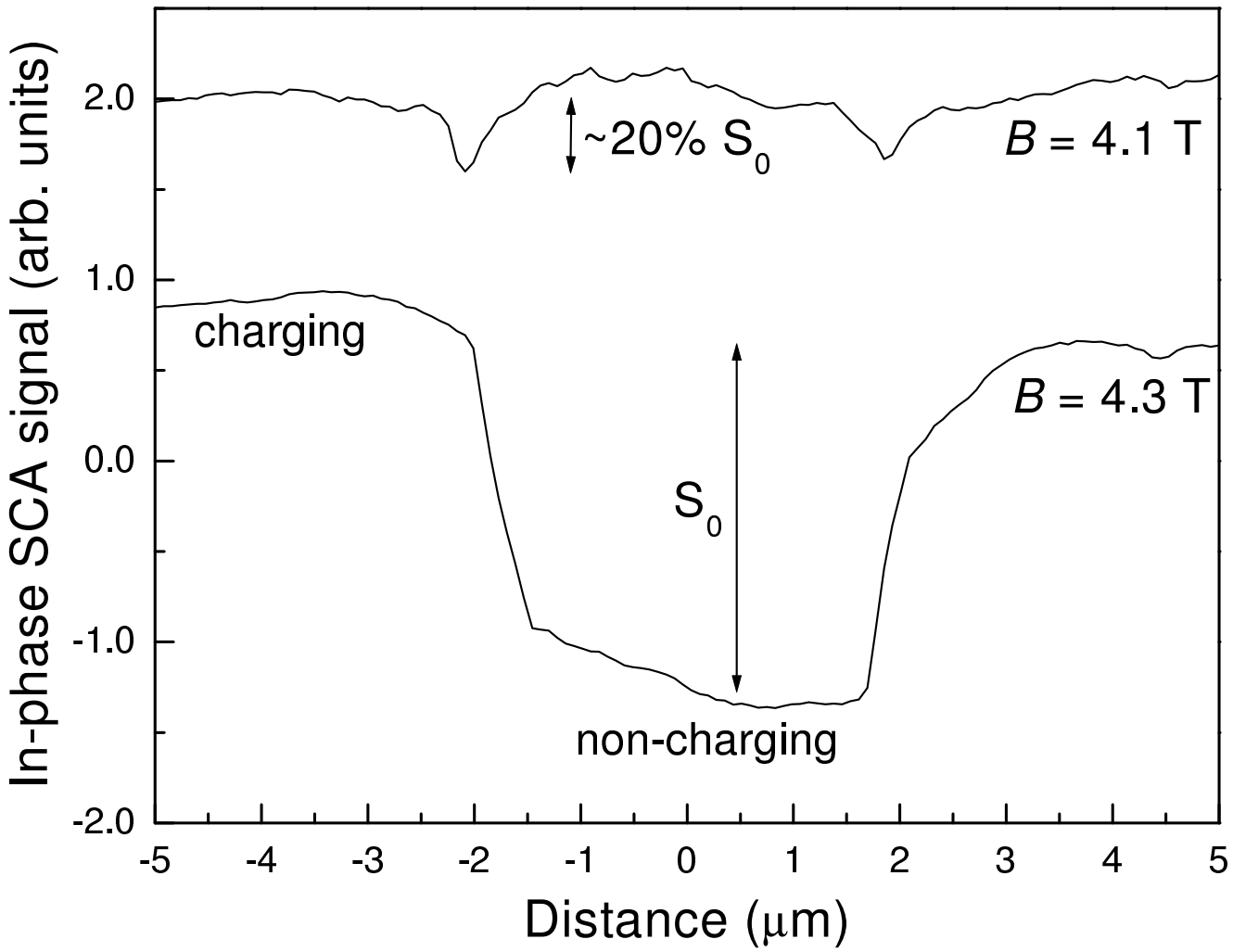

Figure 4-12: SCA line scans reproduced from Figure 4-6. The vertical scale is the same for the two curves. The trace at 4.3 Tesla (bottom) is dominated by the strip resistance that does not allow charging of the interior region ($-2.0 < x < 2.0\ \mu m$). The trace at B=4.1 Tesla (top) is dominated by capacitance. The DOS inside the strips is finite and the strips partially charge. Hence, the signal measured at the strip location, only attains 20% of the charging-completely non charging magnitude, S_0.

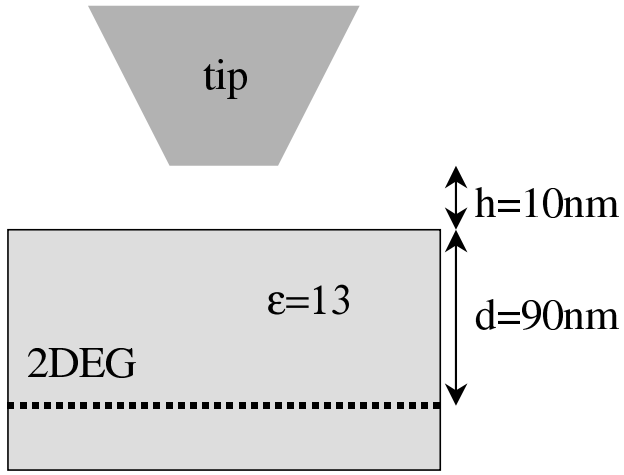

Figure 4-13: Approximating the tip-2DEG system as a parallel plate capacitor. The tip scans at a fixed distance h above the sample surface.

smaller than the zero magnetic field DOS value. This result is in agreement with the values obtained from measurements of D between Landau levels on bulk 2DEG samples with lateral dimensions of $\sim$ 100 μm [36]. Our observation demonstrates that the nonzero density of states in the cyclotron gap is established on length scales smaller than the strip width.

The low-compressibility strip discussed above, corresponds to filling factor $\nu = 4$ and reappears at filling factor $\nu = 2$. We compare the strips at $\nu = 2$ and 4 in Figure 4-14. Their measured widths are at least $w \sim 0.6$ μm and ~ 0.4 μm respectively. These widths are significantly larger than predicted by the theory on which Equation 4.3 is based. This result is typical of our measurements under a range of filling factors and electronic density gradients. Taking for example, $\frac{dn}{dx} \approx 5 \times 10^{10} cm^{-2} \mu m^{-1}$ which is the case for the data in Figure 4-14, we obtain from Equation 4.3 the widths $w_0 = 0.23$ μm at $B = 4$ Tesla ($\nu = 4$) and $w_0 = 0.17$ μm at $B = 8$ Tesla ($\nu = 2$). The deviation from the theoretical result is even more pronounced in Figure 4-9, where the measured width of 2 μm is four times larger than expected.

Theory predicts that the magnetic field modifies the electron distribution so that within the incompressible strip the electron density is everywhere fixed at a level corresponding to an integer Landau level filling factor. This picture relies on a zero DOS in the cyclotron gap and must be altered if the density of states is nonzero. In

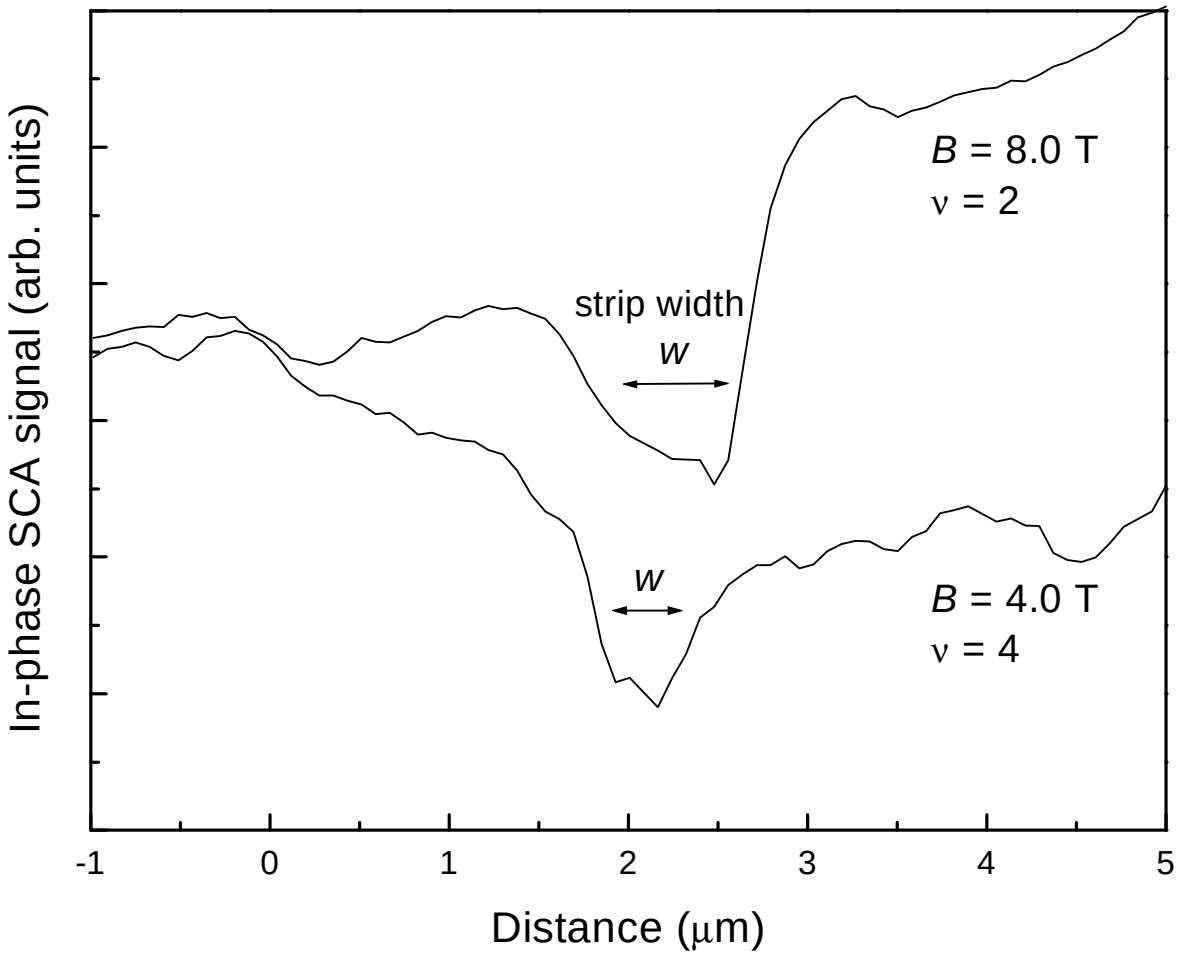

Figure 4-14: Width of low-compressibility strip at filling factors 2 and 4. The widths are larger than those expected from theory.

particular, the resulting screening should eliminate the region of $\frac{dn}{dx} = 0$. However, even in this case, a low compressibility strip should form in sample regions where the Fermi energy lies between Landau levels and the DOS is low. If the average DOS between the Landau levels is D, then the areal density of these states is $\hbar\omega_c D$. This should in turn be equal to the span of the electron density across the strip, given by $\frac{dn}{dx}w$. We thus estimate the average DOS between Landau levels as

$$D \sim \frac{dn}{dx}\frac{w}{\hbar\omega_c} \tag{4.6}$$

Taking the strip width $w \sim 0.5\ \mu m$, we obtain an approximately tenfold suppression of the DOS as compared to its value at zero magnetic field. This result agrees well with our previous estimate that was based on the signal strength at the strip location.

The effect of finite DOS can be understood by considering the corresponding Thomas-Fermi screening length $q_s^{-1} = \frac{\epsilon}{2\pi e^2 D}$. One then finds that $q_s^{-1} \sim 50$ nm, which is much smaller than the width of the strip. The electric field across the strip is then effectively reduced. But the potential difference across the strip remains unchanged at $\frac{\hbar\omega_c}{e}$ (see Figure 4-3(a)). Since,

$$eEw \approx \hbar\omega_c \tag{4.7}$$

it follows that the width w must increase. We thus see that the basic assumption underlying Equation 4.3, namely that the screening by the states in the cyclotron gap is negligible, does not hold in our case.

The broadening of a low compressibility strip as a result of a nonzero density of states between Landau levels, has been studied theoretically by Larkin and Levitov [74]. They found that in that case, the width of the strip is quite accurately given by:

$$w = \frac{2}{\pi}w_0 + \frac{\Delta n}{\frac{dn}{dx}} \tag{4.8}$$

where Δn is the areal density of electrons in the cyclotron gap. Equation 4.8 shows that when $w \gg w_0$, we may approximate w by $\frac{\Delta n}{\frac{dn}{dx}}$ as we have done above. Conse-

quently, from our experimental results, we estimate that the areal density of states in the cyclotron gap is $w\frac{dn}{dx} \lesssim 5 \times 10^{10} cm^{-2}$. This value agrees well with that measured in a sample of similar quality at $\nu = 4$ in [41], as well as with a theoretical result obtained by Efros in [75, 76].

4.7 Conclusion

In this chapter we have presented a detailed study of a 2DEG in the quantum Hall regime in the vicinity of integer filling factors. Our ability to create smooth density gradients in the 2DEG enables us to observe incompressible strips corresponding to integer Landau level filling factors, and follow their evolution with magnetic field. By comparing our signal strength at different regions of the 2DEG, we conclude that the strips in our sample partially charge due to the nonzero density of states in the cyclotron gap between Landau levels. We have obtained an estimate for the value of the relevant areal DOS and we thus, more accurately, refer to these strips as "low-compressibility" rather than "incompressible".

In addition, our measurements indicate that the strips are significantly wider than predicted by a theory that does not include a short range disorder potential. As we have argued in this chapter, the disorder-induced finite density of states in the cyclotron gap for real samples, may account for the discrepancy.

Chapter 5

Determination of the Longitudinal Resistance of Incompressible Strips through Imaging of Charge Motion

The importance of the edge state picture of transport for a two-dimensional electron gas in conditions giving rise to the quantum Hall effect, has already been discussed in Chapter 4. Several efforts have been made to experimentally investigate aspects of the compressible and incompressible regions that accompany the appearance of these states [77, 78, 79, 80]. In the following pages we proceed to characterize the charging properties of incompressible strips that form in the 2DEG in the presence of a density gradient at high magnetic fields [58, 59, 60].

A metal gate deposited on the sample surface aids in pumping charge into the electron gas and its edges also serve to define the path followed by the incompressible strips. In our present setup we charge an isolated region of the electron layer across such an incompressible strip. We shall show that a simple RC charging model dominated by the tip-sample capacitance, fits the data well. Using this model we can also determine the strip resistance R_{strip} as a function of magnetic field for a range of filling factors [81]. Surprisingly, we find that the strips become more resistive as their widths decrease.

5.1 Sample, probe-sample approach and Measurement Method

The sample used in this work was grown by Prof. M. Shayegan in Princeton University. It is a standard GaAs/AlGaAs heterostructure with a carrier concentration of $1.5 \times 10^{11} cm^{-2}$ and transport mobility of $1.5 \times 10^{6} cm^{2}/V$. A 2-dimensional electron gas forms at the GaAs-AlGaAs interface, 80 nm beneath the surface. The relatively low density of this particular electron system (about half the value when compared to the one used in our previous studies) enables us to reach the $\nu = 1$ filling factor in its bulk, at a magnetic field of about 6 Tesla. In addition, the fractional filling factor of $\nu = \frac{2}{3}$ is also accessible in this 2DEG. These facts become apparent by examining Figure 5-1 which plots the capacitance Shubnikov-de Haas oscillations originating from the quantum Hall conductivity minima in the 2DEG.

Through standard lithography we produce a metal (chromium) gate, patterned in the form of a fingered grating, on top of the surface. The "fingers" are all connected to a common "branch" and they are 10 μm wide with a periodic 10 μm - 20 μm spacing between them. The gate structure is 10 nm tall and the arrangement is shown in Figure 5-2.

We use the technique of subsurface charge accumulation (SCA) imaging to obtain a charging map of the 2DEG in-between top gate "fingers", in the regime of the integer quantum Hall effect. Our a.c. excitation has an r.m.s. amplitude of 6 mV, and is applied to both the top gate and the 2DEG. As explained previously, due to its capacitance to the grounded body of the scanning microscope, the 2D electron layer charges and discharges periodically in response to the applied signal. Again, we measure the signal in-phase and 90° lagging from the excitation. This signal is induced on a sharp metal tip that we scan $\approx$ 10 nm above the sample surface (i.e. just above the metal top gate). The sample and microscope are immersed in a pool of pumped liquid helium-3 and are maintained at a constant temperature of 0.35 Kelvin during operation.

In principle, we may use the sample gate in order to vary the electronic density

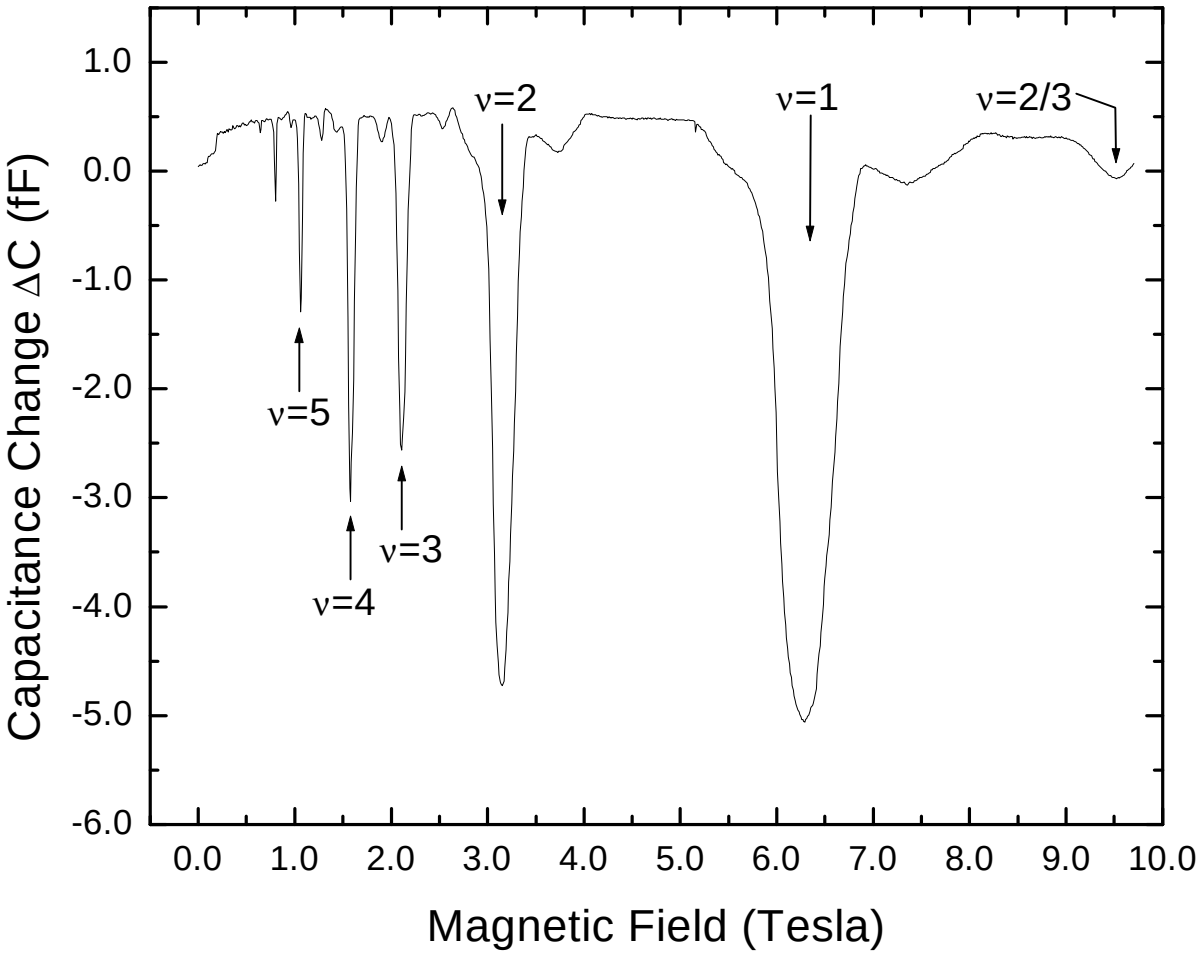

Figure 5-1: Shubnikov-de Haas oscillations in the tip-2DEG capacitance, measured at 0.35 Kelvin. Each minimum results from greatly reduced longitudinal conductivity in the bulk of the 2DEG due to the onset of the quantum Hall effect, and is accordingly labeled with the corresponding filling factor.

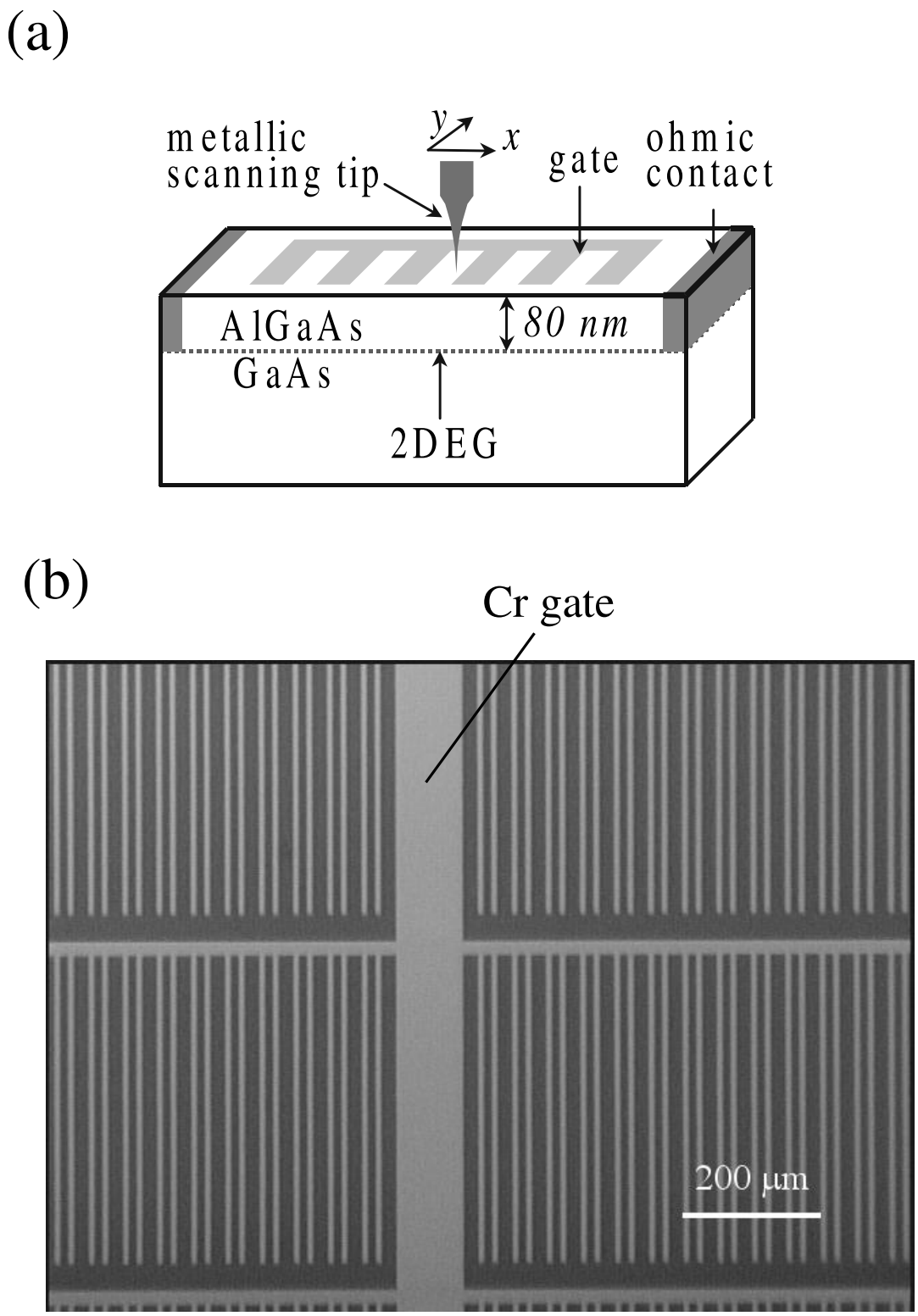

Figure 5-2: (a) 2DEG sample schematic. (b) Photograph of the sample surface taken with an optical microscope. A chromium "tree" gate has been deposited on the surface. The spacing between gate fingers alternates from 10 to 20 μm.

n in the 2DEG. We may also control the gradient in n in the depletion region that naturally exists near the gate edges (section 5.2.1). In practice however, we find that our data possess significant "drift" when the gate is d.c. biased with respect to the 2DEG. The drift occurs in time scales as small as a few minutes and renders the measurement meaningless. This behavior is most likely caused by mobile donors and impurities in the donor layer or by a parallel conduction layer that partially screens the electron gas. To avoid these problems, we cool the sample with 0 Volts d.c. applied to the gate with respect to the 2DEG, and maintain this potential difference between them at all times during our measurements.

It is important to mention here that the presence of the top gate greatly facilitates the procedure of tip-sample approach. It also totally eliminates the need to operate the instrument in tunneling mode in order to locate the sample surface before measurements can begin. The following steps are used to achieve this: While operating the microscope in capacitance mode, the bottom piezoelectric tubes are employed to "walk" the sample closer to the tip. The potential on the Cr gate is kept at 0 Volts d.c. with respect to the Pt-Ir tip. The signal is constantly monitored and grows as the distance to the tip decreases. The walking process may be stopped at any time, so that one can take a scan image. If the sample is sufficiently close, the scan image will display contrast due to the fact that the gate is closer to the probe than the 2DEG and the capacitive signal is higher. Of course, this will happen provided that some part of the gate lies within the scan window. The location of the gate then becomes known and one may position the probe directly above a region of the metal gate. While recording the capacitance signal, one should slowly move the probe vertically so that it eventually touches the gate. At this point the scanning probe becomes grounded, and so does the base of the measurement transistor that is electrically connected to it (recall that the sample gate is kept at zero Volts d.c.). The measured signal drops to zero. The movement of the probe should be stopped at this point to avoid damage from pressing it against the Cr gate. Since the vertical motion of the tip results from the calibrated displacement of the scan piezo tube, the tip-sample separation may be accurately determined.

The advantage of circumventing tunneling mode, is obvious if one recalls the perturbative effect of the tunneling current on the 2DEG density from section 4.2. One may thus accurately position the tip with respect to the sample, and operate the microscope without inducing undesirable perturbations in the 2DEG or donor layer above it. From now onwards, our measurements only probe unperturbed regions of two-dimensional electron systems.

5.2 Experimental Results

Figure 5-3 presents a 12×12 μm SCA image at zero magnetic field. These images result from scanning the tip over an ungated portion of the sample situated between two gate fingers that run parallel to each other. The scan window is positioned so that only one finger appears on the left. In the absence of magnetic field, the 2DEG maintains high conductivity and thus charges uniformly in phase with the applied a.c. excitation. As a consequence, the signal lagging the excitation (Y-phase) is zero everywhere, and the corresponding image shown in Figure 5-3b displays no contrast. The picture changes dramatically in the presence of a perpendicularly applied magnetic field. At 6.4 Tesla (filling factor $\nu = 1$ occurs at ≈ 6.2 Tesla in the bulk of our sample), charge flowing from near the gates, now penetrates the 2DEG only partially (Figure 5-3c). In addition, the Y-phase signal in Figure 5-3d peaks at the boundary between charging and non charging regions. Of course, we do not detect any signal from areas of the 2DEG lying below the gate fingers since the metal gate fully screens the electric field from these regions.

5.2.1 Formation of Incompressible Strips and Consequences from their Presence

The formation of an incompressible strip occurs in regions where electrons completely fill a Landau level. Therefore, in these areas $\sigma_{xx} \rightarrow 0$, and the strip prevents charge from flowing freely into the interior of the sample, exactly as depicted in Figure 5-3c.

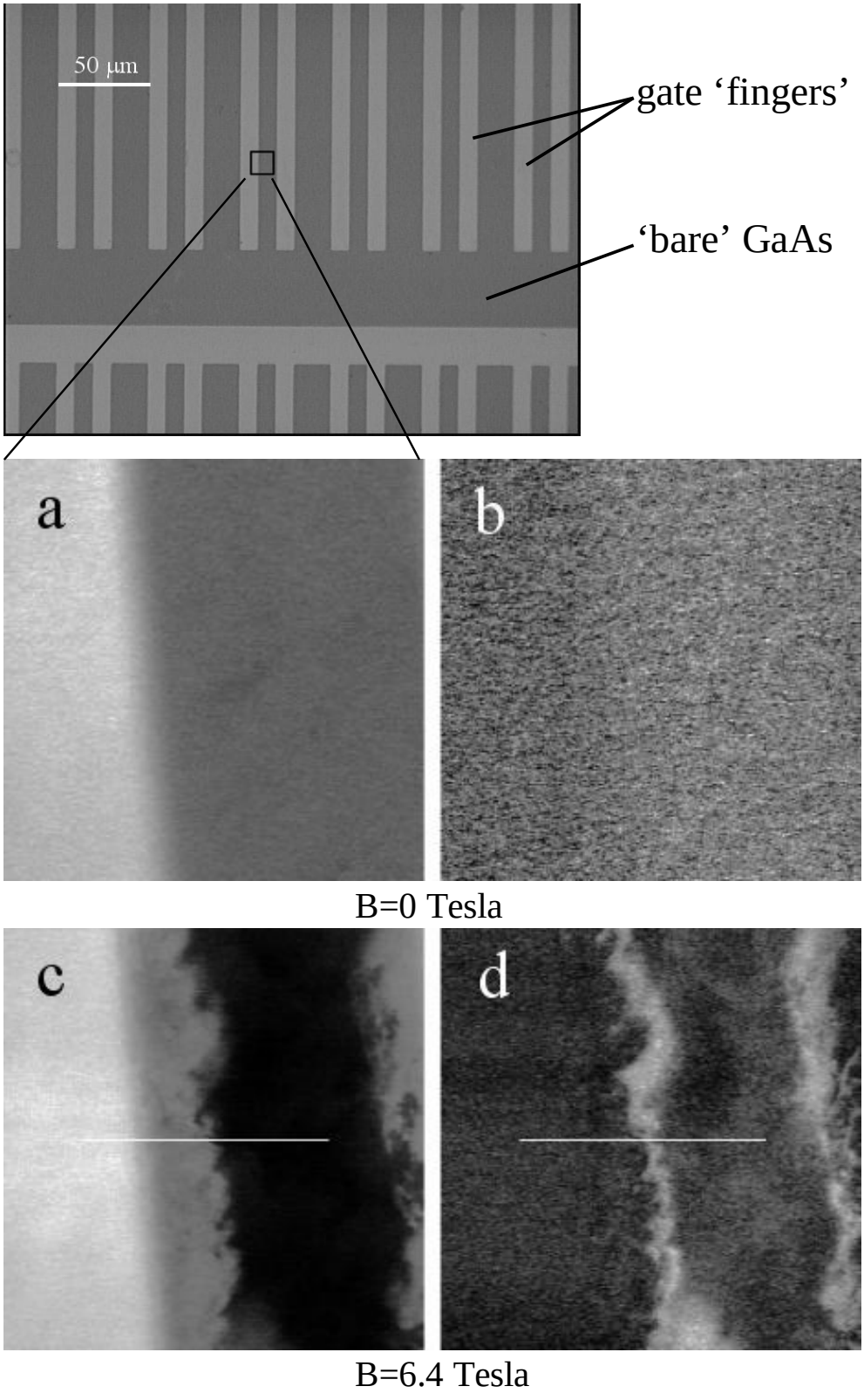

Figure 5-3: In-phase (left panels) and out-of-phase (right panels) SCA images of a $12 \times 12 \mu m$ region. The gate (bright region on the left of the images) is closer to the scanning probe than the 2DEG, resulting in a larger capacitance signal.

The regions of the 2DEG with very low conductivity give rise to a phase lagging SCA signal.

Decreasing the strength of the applied magnetic field reduces the degeneracy of the Landau levels. The strip, as well as the boundary that separates charging from non-charging regions, moves closer to the fingers where the density is lower. By following this evolution with field, we determine the density gradient close to the gate to be $\approx 1.2 \times 10^{10} cm^{-2} \mu m^{-1}$.

A detailed series of images in stepped magnetic field, shows that the electron density of the 2DEG in the region between the gate fingers is constant around the center but then decreases moving toward the fingers to the left and to the right. In this work, we do not apply any external bias voltage on the gate. However, the electronic density under the metal (chromium) gate is reduced by about 15% from its bulk value due to the difference in chemical potential between the metal and GaAs. As a result of this density profile, an incompressible strip, running parallel to each finger, forms at high magnetic fields. By moving our scan window laterally along the fingers of the gate, we have verified that neighboring strips may close on each other at certain locations (Figure 5-4), thus forming closed loops. The area of the 2DEG inside such a loop becomes electrically isolated from the rest of the electron layer. We should note here that although we do not observe the strips directly, we infer their presence from the characteristics of the charge flow in different regions of the sample.

We would also like to bring attention to the jagged nature of the charging boundary, in our scans near quantum Hall plateaus. Variations in the underlying potential landscape can generate a complex topology of edge channels and incompressible strips more specifically [38, 82]. Figure 5-5 clearly illustrates this fact with scans at two distinct sample regions, near the edge of the metal gate. These high resolution images allow us to observe a percolation-like charging behavior of the 2DEG [83, 84], as dictated by the topology of the background 2DEG potential.

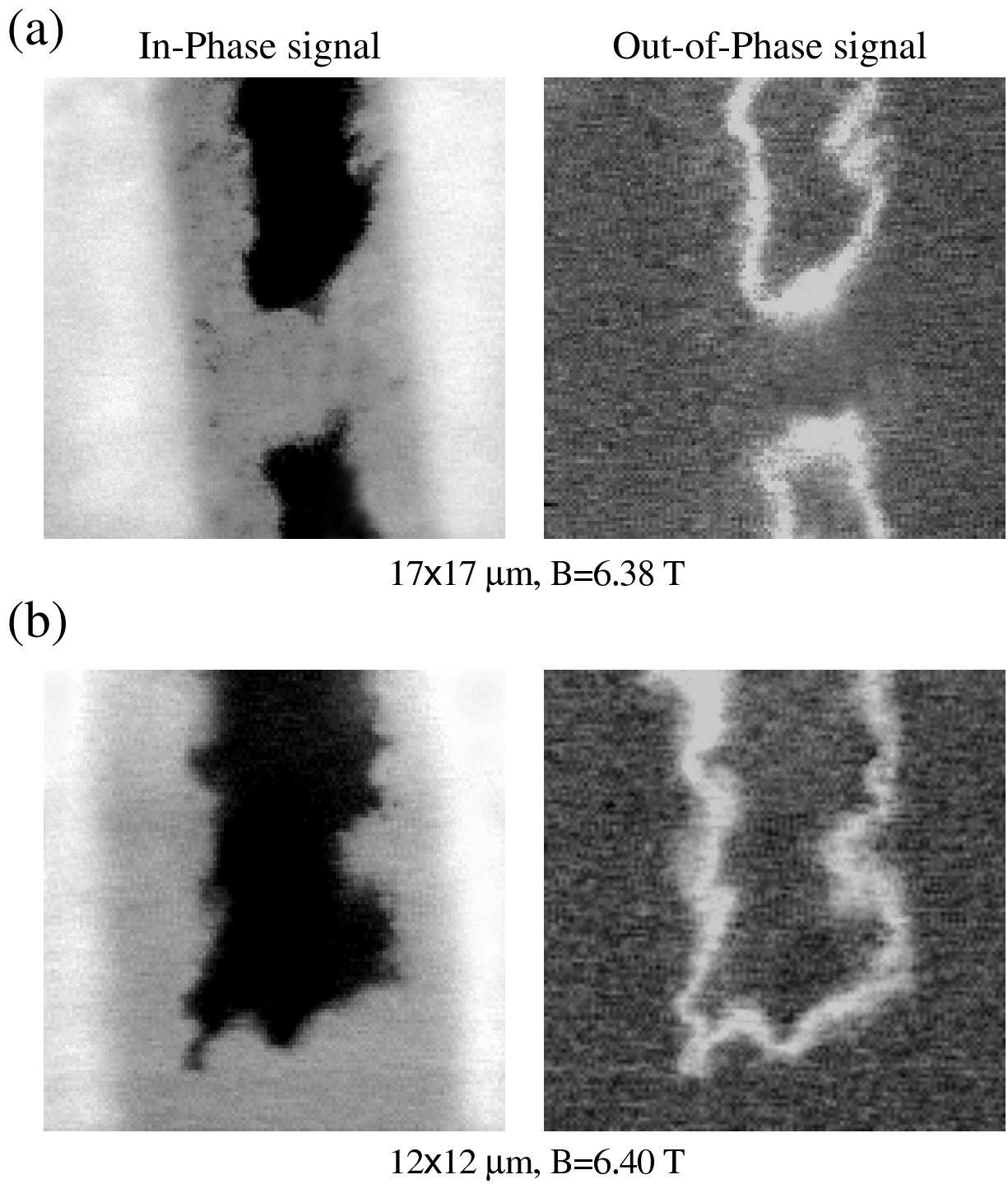

Figure 5-4: SCA images demonstrating strips closing on each other. Images in (a) and (b) originate from different sample locations and are not related to each other. The out-of-phase signal peaks at the boundary between charging and non-charging 2DEG regions.

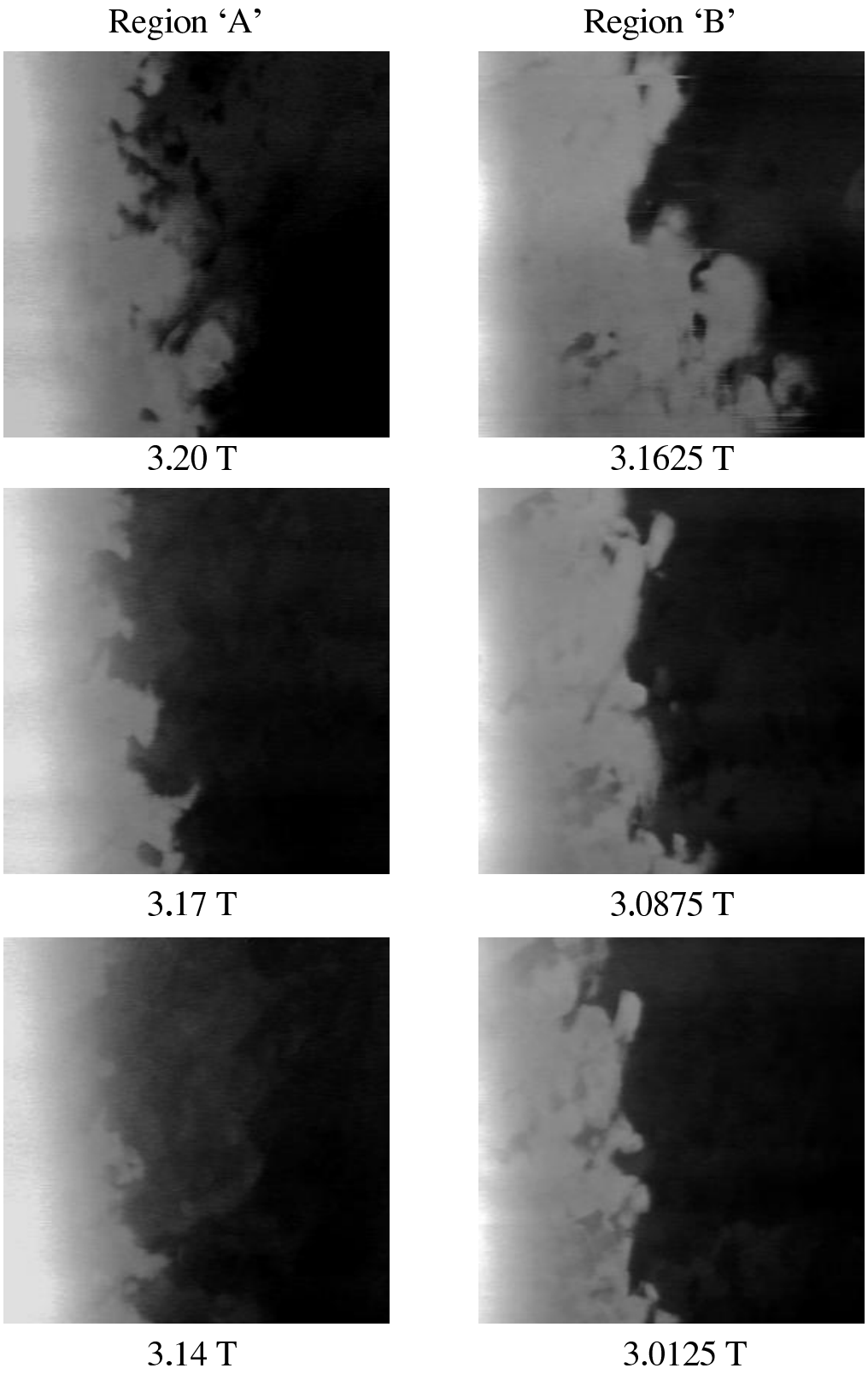

Figure 5-5: 5×5 μm scans at $\nu = 2$ of two different areas near the gate. Inhomogeneities in the background potential (and hence density) in the 2DEG, cause the appearance of intricate spatial variations at the edge of the charging regions.

5.2.2 Gating effect of the Scanning Probe

The work function difference between the Pt-Ir scanning tip and the GaAs surface results in a finite electric field that perturbs the electronic density of the 2DEG in the vicinity of the tip. As described in section 2.4.3, we perform Kelvin probe measurements and subsequently apply a bias voltage to the tip that nulls this electric field. For values away from this nulling voltage, the probe acts as an effective gate on the sample. Figure 5-6 illustrates this behavior by showing scans of a 12×12 μm region at 6.30 Tesla for different tip biases. With the local density under the tip reduced, the condition for integer filling of the $\nu = 1$ Landau level is satisfied at a region with higher intrinsic electron density. As a result, the location of the observed strip changes and shifts towards the interior of the imaged region. The resulting density suppression, though local, extends to $\approx 1\mu m$ and connects regions that would otherwise be separated by incompressible fluid.

The shapes of areas with high out-of-phase signal in Figure 5-6b,c resemble sets of arcs. The centers of the arcs are located roughly along the strip position measured at nulling voltage in Figure 5-6a. This observation suggests the following non-local gating mechanism: Bringing the biased tip on-top of a high density region that does not charge at nulling voltage may reduce the density and permit charging. In this case, there should exist a path going from the tip location all the way to the gate, where the filling factor is everywhere less than the nearest integer. The density perturbation induced by the tip decays sharply in the lateral direction. Hence the most crucial point along this path is situated at the strip location as measured at nulling. Indeed, in many cases the centers of the arcs such as seen in Figure 5-6, point to the location of features in the unperturbed images (see for example the feature in Figure 5-6a marked by "x"). We speculate that each arc indicates tip locations where the tip influence on the "weak link" in the strip is the same. On one side of the arc, the weak link is open and the area under the tip charges fully (zero phase-lagging signal and large in-phase signal). On the other side of the arc, the weak link is closed and the area under the tip becomes effectively disconnected from the gate (zero in-phase

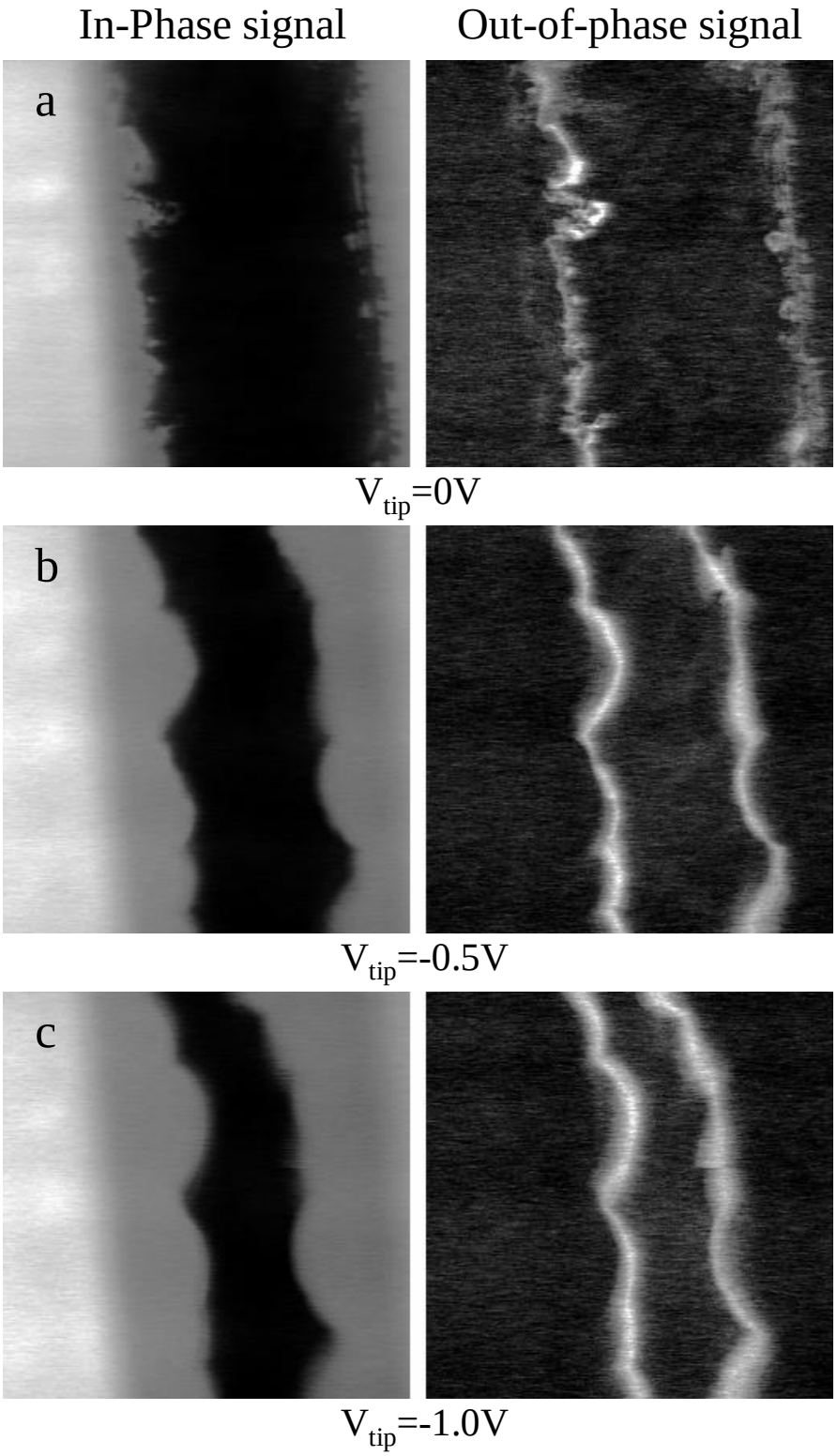

Figure 5-6: 12×12 μm SCA images at B=6.30 T for different biases applied to the tip with respect to the 2DEG. Images on the right again correspond to the measured out-of-phase signal. The scan window is positioned so that two neighboring gate fingers are imaged. The incompressible strips at $\nu = 1$ are squeezed towards the two fingers as the density is raised with the tip.

and phase-lagging signals). As usual, the high phase-lagging signal indicates partial charging. Since there are a number of weak spots in the strip, the areas of high phase lagging signal appear as arcs in our measurements away from nulling voltage. These spots are separated by an average distance of $\sim 3\mu m$ and are very similar to the scattering centers reported in Reference [85].

We can counter changes in the position of the strip effected by the tip bias, by properly tuning the magnetic field. At $\nu = 1$, the incompressible strips appear at the same location if we change both magnetic field and tip voltage at a rate of $\frac{dV}{dB} = 0.5\frac{V}{T}$. At $\nu = 2$ we find that $\frac{dV}{dB} = 1.0\frac{V}{T}$ creates the same effect. This behavior shows that density changes are compensated by varying the degeneracy of the Landau levels, or equivalently the number of electrons that each level can accommodate. The voltage required for compensation should then be proportional to the filling factor, in good agreement with the experiment.

Having understood how our probe may affect the system under study, we null the electric field created by the intrinsic work function difference between the scanning tip and the sample. All SCA images and measurements, other than those in Figure 5-6 reported in this chapter, result from scans taken at null tip-sample electric field.

5.3 Charging a 2DEG across an Incompressible Strip

We now describe the results of SCA measurements obtained by scanning single lines from the gate to the interior of the sample. Figure 5-3 shows schematically their positions within the 12×12 μm scan window. The boundary between the gate finger and the bare sample occurs at $x \approx 1.5\mu m$ (distance of 1.5 μm from the leftmost point of the linescan). The magnitude of the resulting signal step reflects the difference in SCA signal measured with the tip positioned above the metal gate ($0 < x < 1.5\mu m$) and above a fully charging region of the 2DEG ($1.5\mu m < x < 3.1\mu m$). This observed step does not vary with magnetic field (see Figure 5-7), indicating no field dependence

in the response of our charge amplifier to the amount of charge flowing in regions of the 2DEG adjacent to the gate.

At zero magnetic field as well as at fields away from the quantum Hall plateaus, the 2DEG charges nearly as a classical 2D metal. This situation changes upon tuning the field close to the integer Hall plateaus. The leftmost sequence (in-phase signal) of line scans in Figure 5-7 shows the appearance and evolution of another SCA signal step at fields around 6.4 Tesla. The decrease in signal in the region between neighboring gate fingers results from the formation of incompressible strips at $\nu = 1$, running parallel to the gate. We point out that this region in the interior, bounded by incompressible strips on both sides, has $\nu > 1$ and high conductivity (σ_{xx}).

To understand the origin of the 90° lagging SCA signal (curves on the right of Figure 5-7), we consider an RC charging model for our 2DEG and assume that the interior of the sample charges through a strip characterized by resistance R while the tip is coupled to the 2DEG via a capacitance C (see inset in Figure 5-8b). As we shall see below, this capacitance totally dominates over the self-capacitance of the "isolated" $\nu > 1$ higher conductivity region. We may recall from section 3.4.2 that the resulting in-phase signal measured at the tip, is proportional to $\frac{1}{1+(\omega RC)^2}$ while the out-of-phase evolves as $\frac{\omega RC}{1+(\omega RC)^2}$. The X-signal drops steadily to zero as the resistance of the region under the tip increases while the Y-signal goes through a peak near the roll-off frequency of $\frac{1}{\omega RC}$. The presence of the out-of-phase signal indicates that there is not enough time to fully charge the 2DEG during one complete cycle of the excitation. Clearly, when the conductivity of the 2DEG is high (e.g. in zero magnetic field or away from the QH plateaus) there is no Y-signal, and the corresponding image displays no contrast (see Figure 5-3b).

We find that at the high field side of the Hall plateau (6.46 T in Figure 5-7), the effective resistance for charging the interior region through the incompressible strip turns out to be fairly low. In this case, the interior region can still partially charge during the a.c. excitation cycle. With decreasing magnetic field, the incompressible strips move to the lower density region closer to the gate. The signal step between charging and non-charging regions grows, indicating that the interior region charges

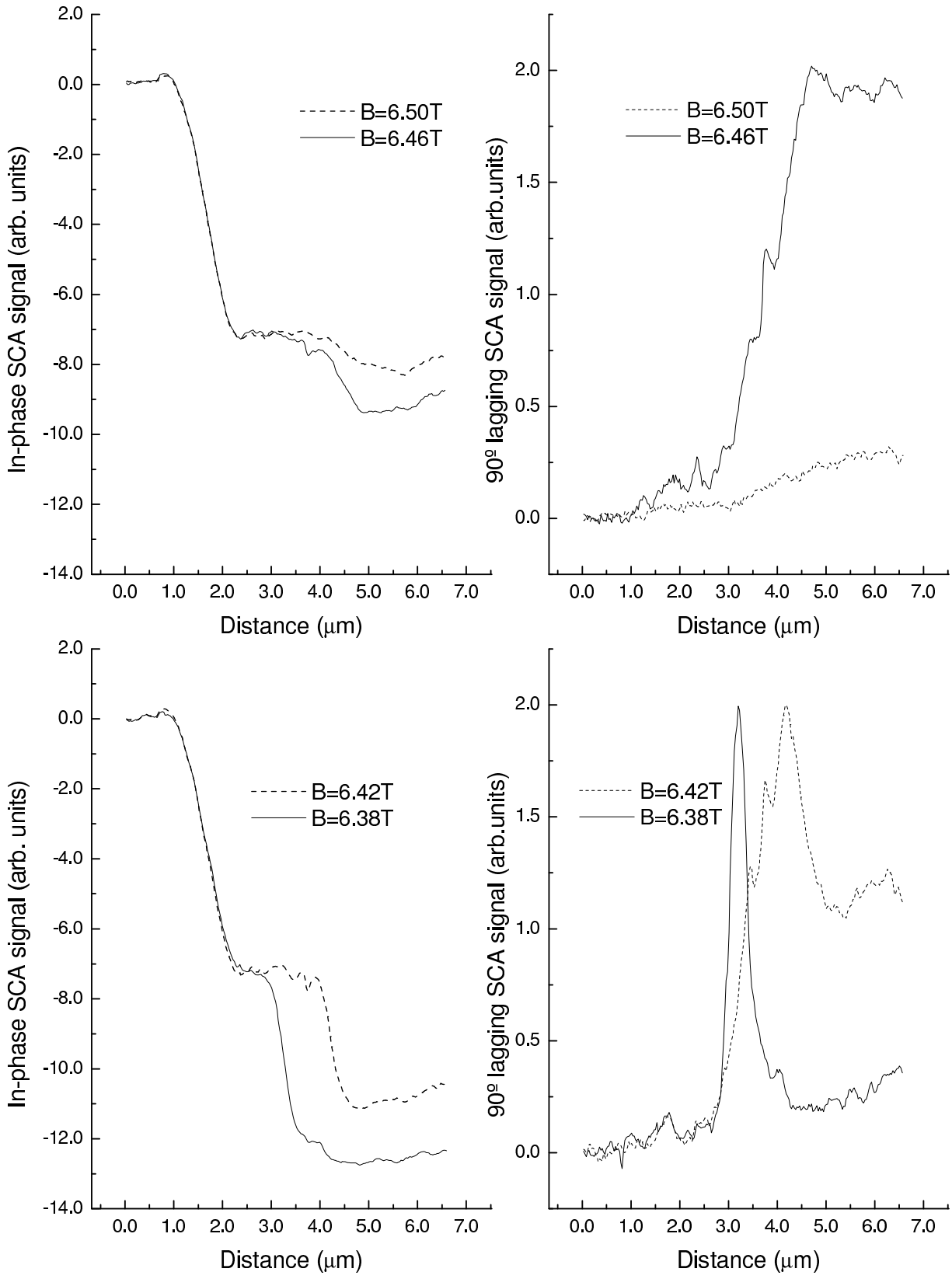

Figure 5-7: Evolution of scans taken along the solid line of Figure 5-3 with magnetic field. Note the different vertical scales for the in-phase and out-of-phase curves.

less, and therefore that the effective resistance across the strip steadily grows as the field is reduced. By tracing the strip position as a function of magnetic field, we have determined that the density gradient is steeper closer to the gate. Therefore, the incompressible strips should become narrower in this case [60, 64]. We conclude that, counter-intuitively, at lower fields, when the strip is expected to become narrower, the effective resistance for charging across the strip increases.

Summarizing our findings so far, we have deduced that the formation of the strip at $B = 6.50$ Tesla begins to impede charging of the inner sample region. With decreasing field, this signal in the interior $\nu > 1$ region gradually drops and eventually disappears almost completely at B=6.38 T. At this field and for this excitation frequency, the strip becomes totally impenetrable to charge flowing from near the gate. Further reduction of the field simply pushes the strip closer to the edge of the gate and leaves the picture observed at 6.38 T, along with the magnitude of the X-signal step, unchanged.

5.4 Frequency Dependence of the Charging Signal

The crude RC model used so far dictates that the measured signal also depends upon the excitation frequency. Lowering the measurement frequency should enhance the charging of the 2DEG through the strip provided that R and C remain constant. Figure 5-8(a) presents data that are consistent with this expectation. The same line scan (in a different sample location from the ones plotted in Figure 5-7), is measured at 10, 30 and 100 kHz at a field of 6.52 Tesla. As expected, the 2DEG charges more efficiently at lower frequencies, as evidenced by the increased in-phase signal in the $\nu > 1$ region. The lower trace in that Figure corresponds to a magnetic field of 6.44 Tesla where the strip allows essentially no charge to cross it, and the out-of-phase signal goes through a peak and drops to zero as described earlier. In contrast to line scans taken at slightly higher fields, this trace remains unchanged with frequency. This fact further strengthens our previous assertion that at this particular field value, charge cannot penetrate the strip.

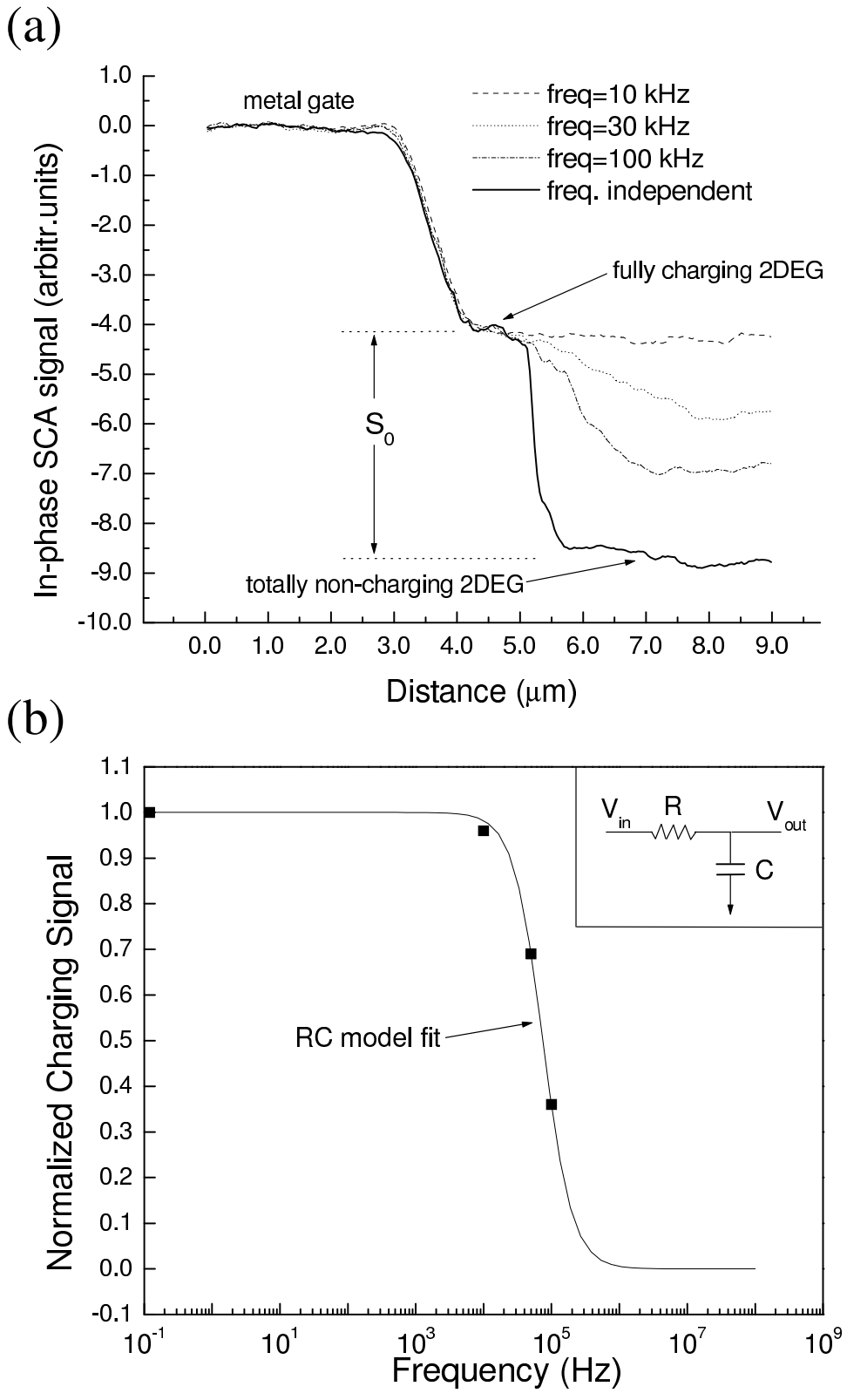

Figure 5-8: (a) In-phase SCA signal from line scans at 10, 30 and 100 kHz. The bottom line is frequency independent and corresponds to the sensitivity calibration trace measured at 6.44 T. (b) Frequency dependence of the measured capacitance signal at 6.52 T, as extracted from the traces in (a).

We use the corresponding step in the in-phase signal between the fully charged and totally non-charged regions that the strip separates (Figure 5-8(a)), to calibrate the sensitivity of our measurement, S_0. We can therefore determine precisely the degree of charging of the 2DEG in the region between the strips at different fields for a range of frequencies and express it as a fraction q of S_0. Figure 5-8(b) plots the quantity q against frequency (the 2DEG charges fully as the frequency approaches zero) using the curves from part (a). The smooth curve fits the data points using the RC model discussed earlier. This simple circuit representation seems to work remarkably well for the system under study. We have performed extensive measurements at several different locations within the sample and find consistent agreement with the RC model. Of course, depending on the particular realization of the density gradient, the exact field at which the strip becomes impenetrable may vary (typically by not more than 1%) but this has no effect on the results or the applicability of the model.

5.5 Resistance of Incompressible Strips

We are now in a position to extract directly the resistance, R, of the strip by assuming that the value for C is the known geometric capacitance C_g between the tip and the 2DEG. We justify this assumption below in an examination of the effects of changing the tip-sample separation. C_g is determined by measuring the signal change at zero magnetic field, as we move the tip vertically from 'infinity' to within 10 nm from the sample surface, yielding $C_g \simeq 0.5$ fF. In addition, since strips form closed loops in our experiment, we are able to follow them to their full extent and hence measure exactly their total length.

For the fit in Figure 5-8 we obtain $RC = 2 \times 10^{-6}$ s and deduce that at 6.52 Tesla ($\nu = 1$), $R_{strip} \approx 100$ M$\Omega/\mu m$. This resistance increases by 1 order of magnitude to ≈ 1000 M$\Omega/\mu m$ at $B = 6.48$ Tesla. We find that at a field of 6.44 T, the strip becomes impenetrable to charge for our range of measurement frequencies. Assuming that the same RC charging model continues to hold, we estimate a lower boundary of 7000 M$\Omega/\mu m$ for the value of R_{strip} in that case. These results reproduce consistently

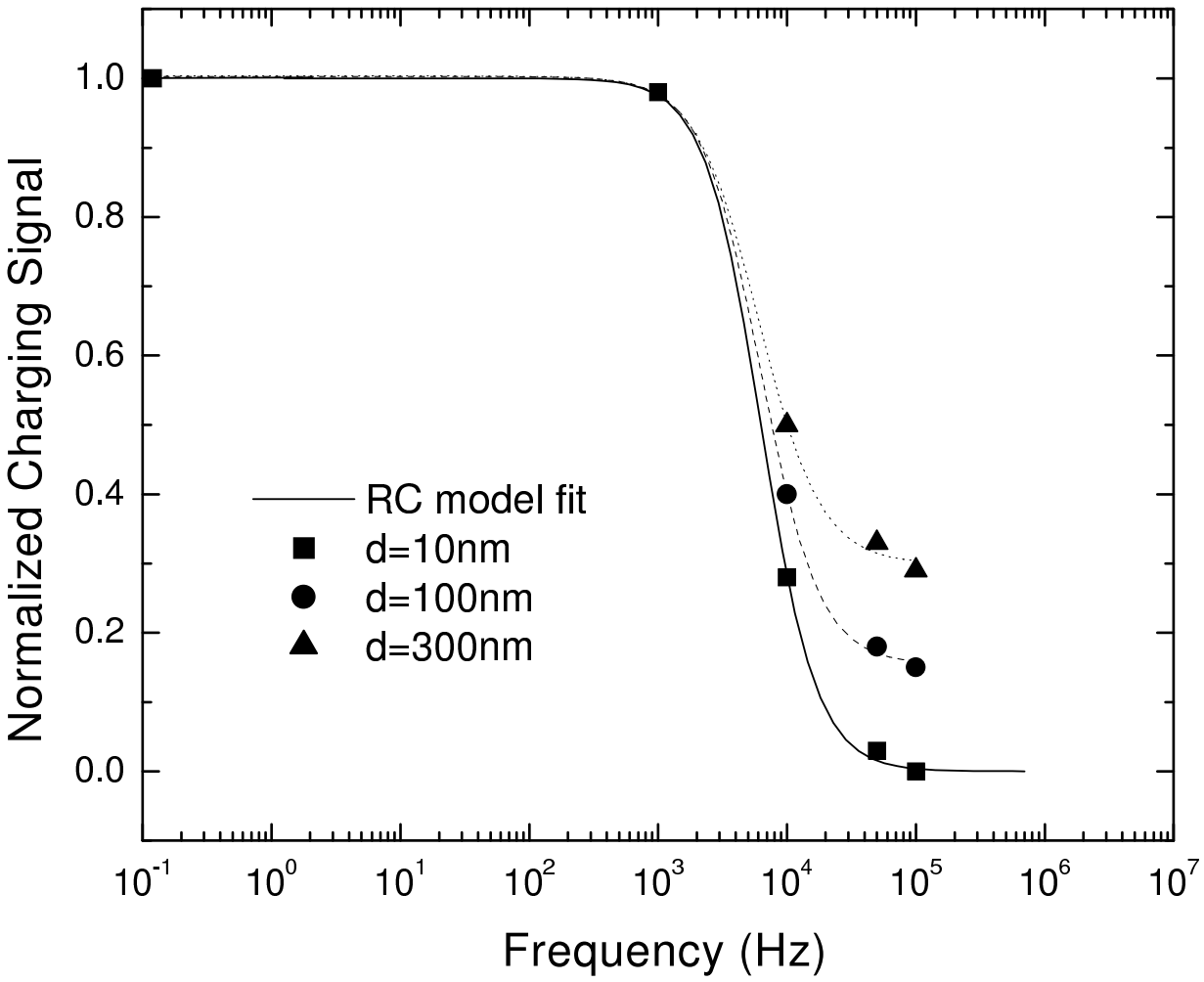

Figure 5-9: Degree of charging of the 2DEG measured for different tip-sample separations at 1, 10, 50 and 100 kHz. Data points are derived from linescans at 6.40 Tesla. Reduction of C_g due to the increase in d, leads to faster charging of the electron layer. The dashed and dotted lines simply connect the respective data points and do not result from fits to them. They serve to accentuate the deviation from the actual RC model fit (solid line).

with small variations (less than a factor of 2) at different locations throughout the sample.

The theory discussed in Chapter 4, predicts that at higher filling factors, the energy gap $\hbar\omega_c$ across an incompressible strip decreases [60]. As a result, the strips should become less resistive. Indeed, we find that the extracted strip resistivity is ≈ 10 M$\Omega/\mu m$ at B=3.26 T and ≈ 400 M$\Omega/\mu m$ at 3.24 T (corresponding to $\nu = 2$). For B=1.60 T ($\nu = 4$), we get $R_{strip} \sim 1$ M$\Omega/\mu m$.

We performed all measurements described so far with the probe scanned very close (~ 10 nm) to the sample surface. The effects of changing tip height are depicted in Figure 5-9. The corresponding line scans are performed at 6.40 Tesla at the same location where the data set in Figure 5-7 originated. The capacitance data points are extracted at the same frequencies for 3 different tip-sample separations, $d = 10nm$, $100nm$ and $300nm$. Their strong dependence on d implies that the geometric capacitance C_g between the probe and the sample dominates over the self-capacitance of the region of the 2DEG located to the right of the strip. We obtained similar results for lower field values up to the point where the strip becomes totally impenetrable. Indeed, $C_{self} \sim \varepsilon_0 a$, with a being the typical length scale of the 2DEG region enclosed by the strip, is about one order of magnitude less than the value calculated for C_g in our experiment. Consequently, C_g seems to be the relevant parameter in our model and its known value may be used in determining the strip resistance from the product RC_g. From the same Figure we also note that, as expected, the 2DEG charges faster as d increases and C_g is reduced. However, the observed deviation from the simple RC charging model implies that a distributed resistance model with variable R is more suitable in this situation. Of course, points corresponding to $d = 10nm$ (black squares) still fit well with the model described earlier, yielding a strip resistance of ~ 1000 M$\Omega/\mu m$ at 6.40 T.

The exact mechanism that is responsible for charge penetrating the incompressible strip can be elucidated by performing temperature dependent measurements of charging across the strip. If the conductivity is due to tunneling of charge [86], then the results should be independent of temperature. In contrast, the presence of tempera-

ture dependence will point towards a conduction mechanism due to electron hopping. Variable-range hopping is a general conduction mechanism in systems with strongly localized carriers at sufficiently low temperatures. In such a regime, the hopping distance increases as temperature is lowered and the conductivity is given as:

$$\sigma(T) = \sigma_0 e^{(-T_0/T)^x} \tag{5.1}$$

The parameter T_0 and the exponent x, depend on the model that one wishes to apply. The Mott law [87] in the absence of long-range Coulomb interactions gives:

$$x = \frac{1}{3} \quad \text{and} \quad T_0 \propto \frac{1}{g(E_F)\xi^3} \tag{5.2}$$

where $g(E_F)$ is the density of states in the vicinity of the Fermi level E_F and ξ is the localization radius. When the interaction energy between localizes electrons is important, the Efros-Shklovskii law [88] gives:

$$x = \frac{1}{2} \quad \text{and} \quad T_0 \propto \frac{e^2}{\epsilon_r \xi} \tag{5.3}$$

where ϵ_r is the relative permittivity.

However, as we described in Chapter 2, our microscope is not thermally compensated. It is thus extremely difficult in practice to perform temperature dependent measurements and as a result they are currently unavailable. In our setup the tip to sample separation will be constantly changing by tens of nanometers as the temperature fluctuates. To overcome this problem one requires an instrument able to compensate for such drifts.

5.6 Conclusion

We have presented a complete account of charging a 2D electron layer through incompressible strips in the regime of the quantum Hall effect. Using a gated heterostructure, we have directly observed the resulting charging patterns in the 2DEG due to

the presence of the strips. Unlike the work described in Chapter 4, we have left the 2D layer completely unperturbed. We instead relied on the small electronic density gradient near the gate edge that led to the formation of the incompressible strips.

We found that a lumped RC charging model of the 2DEG across the strips agrees well with the data and allows us to accurately deduce the strip resistance for a range of integer filling factors. We also presented images that illustrate how small scale density fluctuations and "weak spots" (or scattering centers) affect the spatial properties of the charging region bounded by incompressible strips.

Chapter 6

Topographic mapping of the quantum Hall liquid using a Mobile Quantum Dot

Since the discovery of the integer quantum Hall effect in a two-dimensional electron gas, physicists have argued that electron localization plays a key role in the phenomenon. As we have seen in section 1.2, the existence of localized states at the tails of the Landau levels density of states, is an essential ingredient of the basic Hall conductance quantization [6]. It is now accepted that at $T = 0$, the transition between Hall plateaus is a quantum critical phenomenon in which all states away from the exact center of the Landau level (populated by a single extended state), are localized.

In GaAs heterostructures, the random potential responsible for localization derives mainly from randomly situated ionized donors, located between the submerged 2DEG and the sample surface. In general it is difficult to quantify this potential experimentally since conductivity measurements, the principal tool for studying the QHE, provide only average information about the disorder. Scanning techniques however, provide the ability to probe 2D electron systems on nanometer scales [38, 66, 40, 39].

In this chapter, we show how our charge accumulation imaging microscope can be used to image microscopic details of the disorder potential. We achieve this goal by detecting the motions of single electrons within the system under study. A quantum

dot is created inside the electron layer and the tip drags the dot underneath it as it scans across the sample surface. Monitoring the single-electron charging pattern of the quantum dot, we map the exact electrostatic potential that electrons in the layer sense [89]. Since quantum dots play a central role in this class of measurements, we begin with a brief account concerning their properties. After establishing a basic understanding about them, we continue and present the details of the experiment and its results.

6.1 Quantum Dots

A quantum dot (QD) is an artificially fabricated pool of charge that can contain a discrete number of electrons. This number may range from a single electron to several thousand of them. Dots are usually defined inside a semiconductor material using advanced lithographic techniques and have a typical size of the order of 100 nm. As in a real atom, the energy levels inside QDs are quantized as a direct result of the confinement of discrete electrons in a small region in space. It is thus not surprising that in many ways, quantum dots behave exactly as "artificial atoms", which is another widely used term to describe them [90, 91].

Several of the properties of quantum dots can be studied by performing conductance measurements with them. One may directly probe their quantized energy level spectrum by allowing single electrons to tunnel into and out of the QD. The situation is shown schematically in Figure 6-1. The central metallic island is weakly coupled to two electrodes that act as source and drain of electrons. Particle exchange can only occur between these two reservoirs. A third electrode, the gate, is electrostatically or capacitively coupled to the island and serves to change its potential in a continuous manner.

If we assume that the QD in the above example is initially electrically neutral, an electron tunneling to it must possess an amount of energy at least equal to $\frac{e^2}{C}$, the charging energy of the dot. C denotes the total capacitance between the island and the rest of the system. Equivalently, if the dot contains N electrons, extra energy

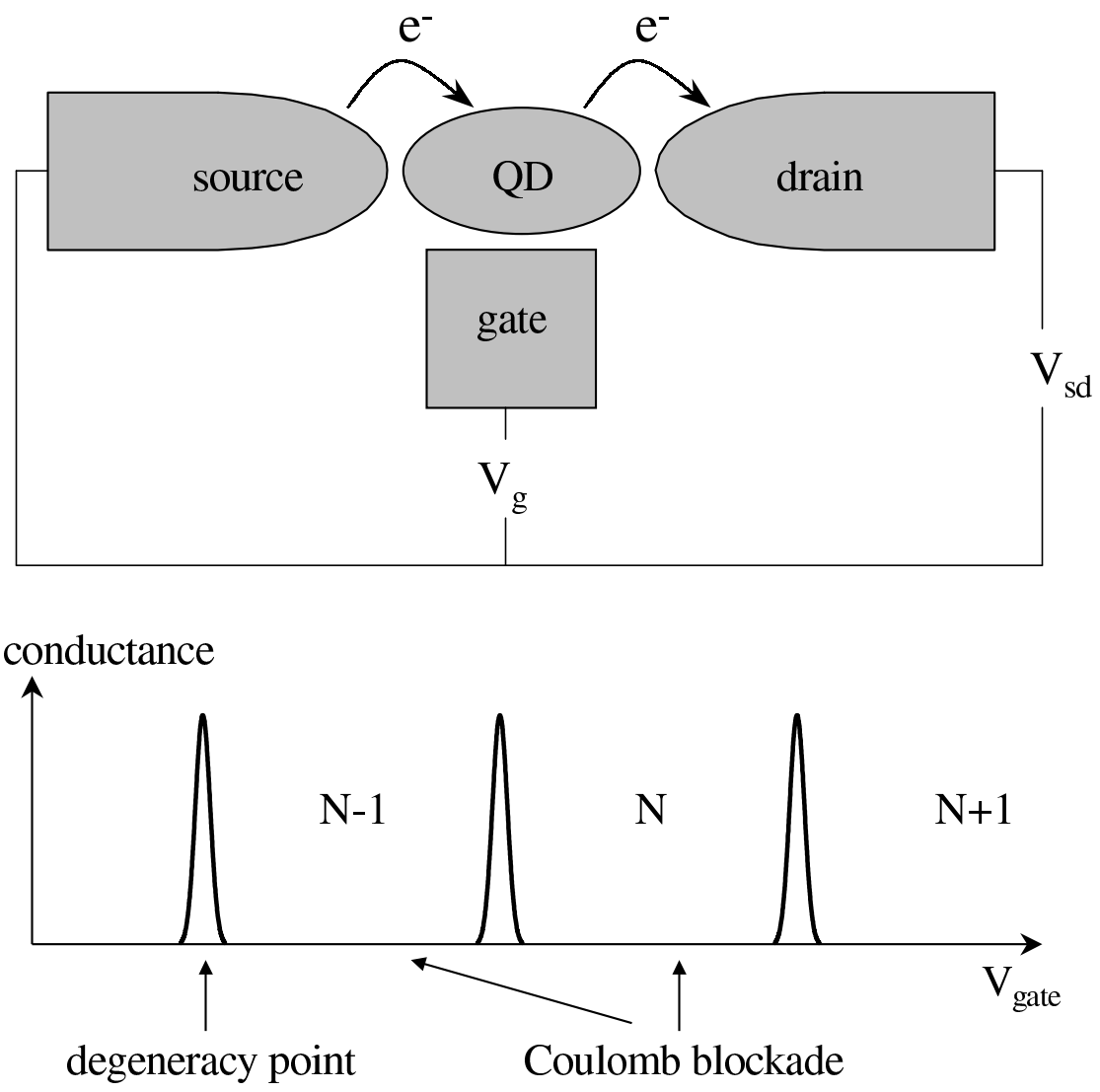

Figure 6-1: Schematic of electron transport through a quantum dot. In-between Coulomb blockade regions, the number of electrons in the dot differs by one.

is required to increase this number to $N + 1$. There will be no current through the system unless the gate voltage is increased by the proper amount. The effect is known as Coulomb blockade [92, 93] and in its simple form presented here, results in a periodic electron addition spectrum as a function of gate voltage.

Of course for Coulomb blockade to be observed, it is necessary that the thermal energy is less than the charging energy E_c. In addition, quantum fluctuations in the number N of electrons should be low enough for the particles to be located on either the source-drain electrons or on the QD. This gives a lower boundary that the tunnel resistances R_t of the barriers should meet. So, the following requirements should be met for charge quantization and Coulomb blockade effects.

$$R_t \gg \frac{h}{e^2} \tag{6.1}$$

$$\frac{e^2}{C} \gg k_b T \tag{6.2}$$

A modified experimental setup that employs a capacitive technique to measure the electronic spectrum of a confined two-dimensional island, is shown schematically in Figure 6-2 [15, 94, 21]. As we will shortly see, this configuration is directly applicable to our measurements performed with the capacitance microscope. From this last figure we notice that the drain lead has been removed and the gate is used to add more electrons into the island. An a.c. excitation applied to the source causes electrons to tunnel back and forth from the dot whenever the Fermi level in the source lines up with one of the energy levels in the "atom" (a so-called degeneracy point of the system). The capacitance between the QD and the gate is thus greatly enhanced due to the image charge induced on the gate. As a result, a peak occurs in the capacitance signal with the addition of every single electron to the dot as V_g is scanned toward more positive voltages.

The physics of quantum dots has become an extremely active research area over the past 10 years. The interested reader will find a wealth of information on experimental and theoretical aspects in [91, 95] and in references therein. Our discussion will continue with the details of our technique and experimental results.

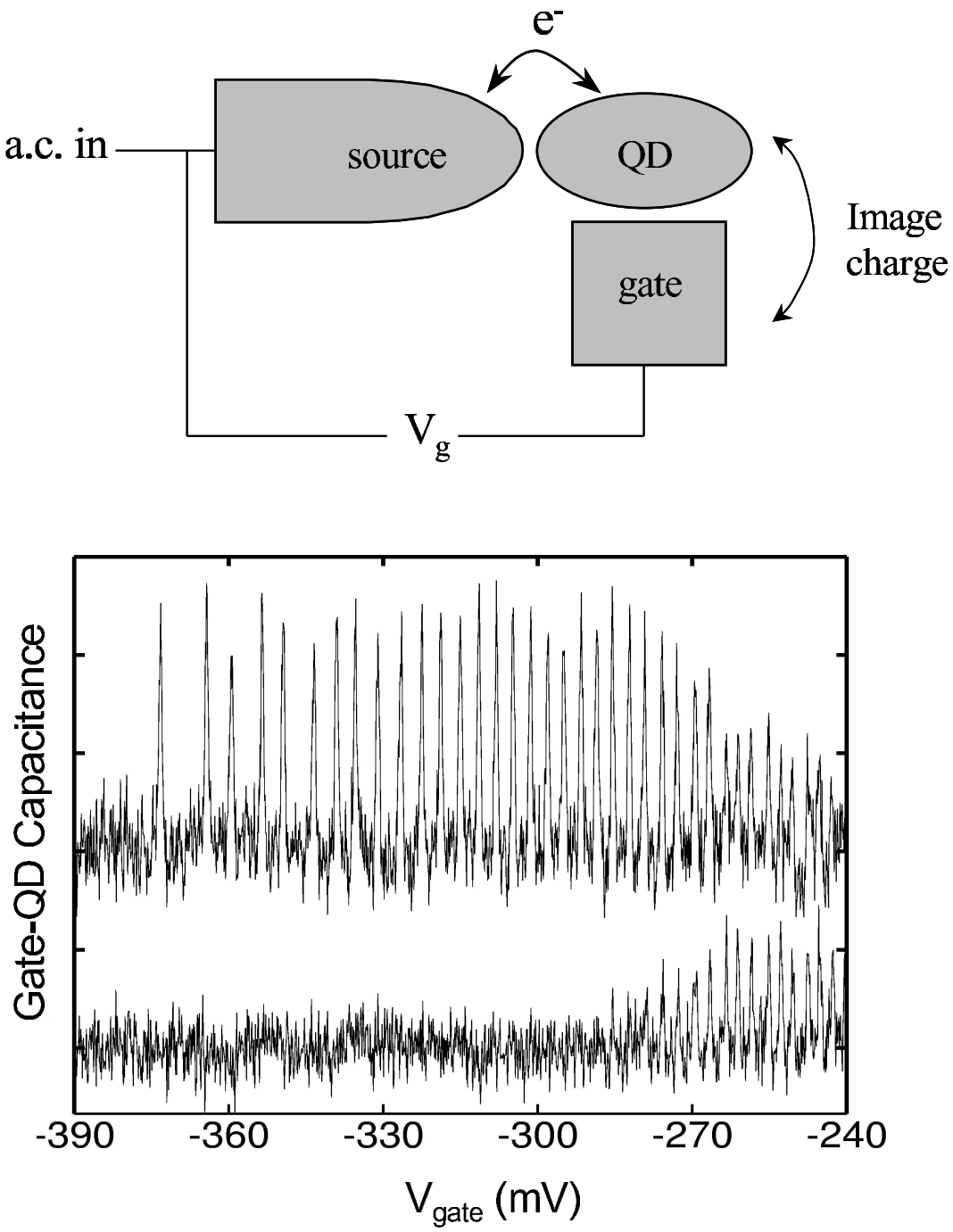

Figure 6-2: Schematic of capacitive measurements of quantum dots. The data in the lower panel have been obtained by Ashoori [15, 16]. Capacitance peaks correspond to additions of single electrons in the dot.

6.2 Measurement details. Creating a Mobile Quantum Dot in the 2DEG

The present study uses the same gated heterostructure sample that was described in section 5.1. We recall that a 2-dimensional electron gas with an areal density of $1.5 \times 10^{11} cm^{-2}$ forms 80 nm below the surface. A metallic gate electrode covers the sample (Figure 5-2). Using our charge accumulation scanning (SCA) technique, we bring a sharp probe close ($\approx$ 10 nm) to the surface and image a region several micrometers in size between two fingers of the gate. As in the work presented in the previous chapter, we do not allow any tunneling current to pass between the probe and the sample. Instead we apply a 3 mV r.m.s. 100 kHz a.c. excitation to the 2DEG and to the gate, and monitor the charging of the electron layer by measuring the image charge induced on the scanning probe with a sensitive cryogenic amplifier.

In scanning probe measurements of semiconductor structures, the tip may strongly affect the system under study, by altering the local electron density. In some occasions, this effect can also work to the researchers' advantage. In our measurements discussed in previous chapters, we compensated the work function difference between the scanning tip and the sample to prevent the tip perturbing the sample electrostatically. The resulting SCA images revealed features arising from variations of the 2DEG compressibility or resistivity.

We still use the Kelvin signal to null the electric field between the tip and the sample as detailed in section 2.4.3. However, we now apply an additional voltage on the scanning tip in order to purposefully change the electron density directly underneath it. The situation is shown schematically in Figure 6-3(a). Unlike the density gradients created in connection with the investigations in Chapter 4, our current density enhancement is local and reversible in nature since it is a direct result of the gating effect that the positive tip exerts on the 2DEG below it. From now onwards we designate the tip-sample voltage as measured in deviation from the nulling voltage.

Let us now consider the situation in the presence of magnetic field. For fields

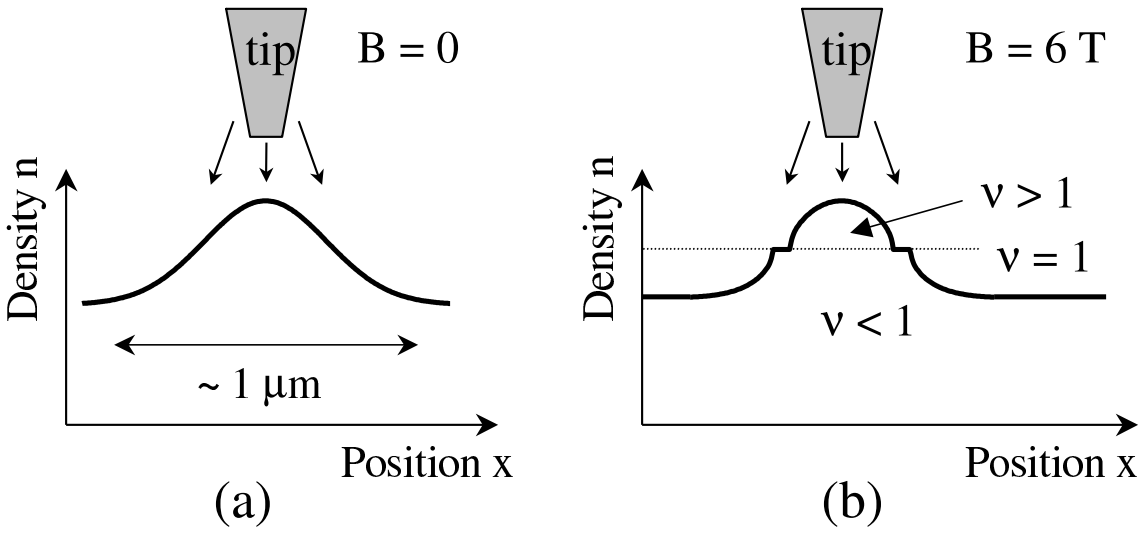

Figure 6-3: (a) Local density enhancement due to positive bias on the tip (b) At fields near integer filling n of the 2DEG, a quantum dot forms where $\nu > n$. An incompressible strip decouples the pool of electrons inside the dot from the rest of the 2D layer.

such that the Landau level filling factor in the bulk of the sample is slightly less than integer, an incompressible strip of integer Landau filling will form in the higher density region beneath the tip, exactly as depicted in Figure 6-3(b). We thus effectively create an isolated "bubble" of electrons in the next Landau level. Using the language of section 6.1, the strip acts as the weak link (or tunneling barrier) that connects an island of electrons (i.e. the "bubble") to the rest of the 2DEG. Electrons may tunnel across the strip and their motion is governed by Coulomb blockade. The analogy with the setup in Figure 6-2 is thus obvious. With the tip assuming the role of a gate, we have created a quantum dot inside the electron layer. As the d.c. biased tip scans above the sample surface, the dot underneath follows, hence the origin of the term mobile quantum dot.

6.3 Mapping contour lines of the 2DEG potential landscape

Figure 6-4 presents a SCA image of a 3.5×3.5 μm region at a magnetic field of 5.5 Tesla. This field corresponds to the $\nu = 1$ Landau level filling factor in the bulk

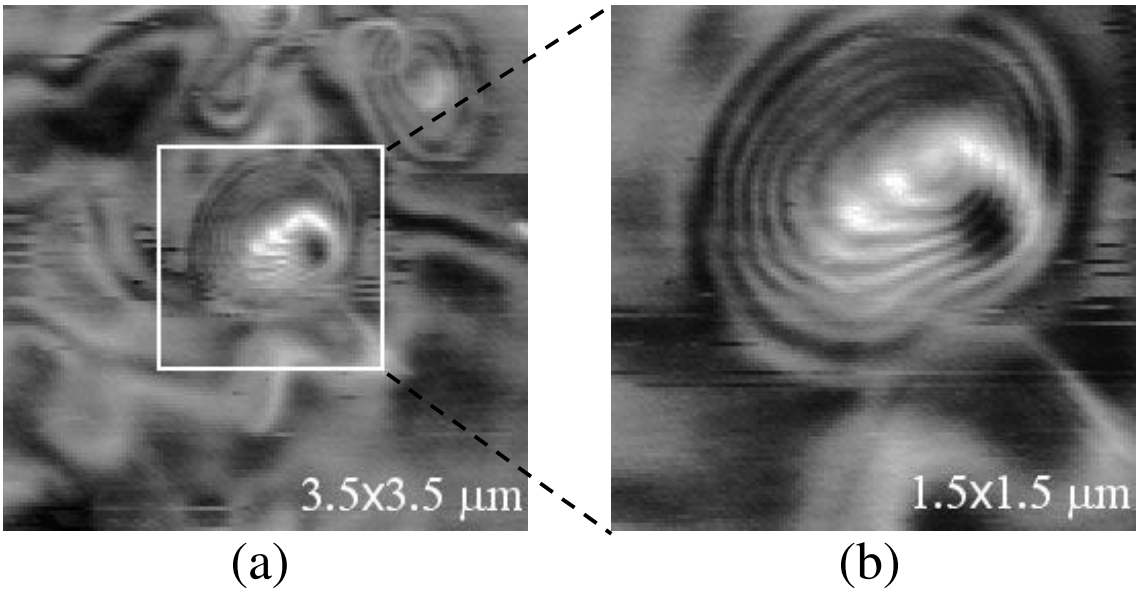

Figure 6-4: (a) SCA image near $\nu = 1$ taken with a positive voltage applied to the scanning tip relative to the electron layer. (b) Zoom-in SCA image of the central region in (a).

of the sample. The tip-sample voltage is +0.7 Volts, resulting in accumulation of electrons below the tip. Bright colors in the image correspond to regions of high signal. The observed features consist of a number of closed contour lines, reminiscent of a topographic map. We remind here that the resolution limit of our SCA microscope is ultimately given by the depth of the 2DEG, which is 80 nm in this particular sample. The separation between successive contour lines can however be as small as 30 nm as shown in the zoomed-in image in part (b) of the latter Figure. Consequently, the contour lines do not represent charging patterns inherent to the 2DEG. They rather reflect variations in the 2DEG charging induced by changes of the tip position. We have established that the periodic appearance is directly linked to the phenomenon of Coulomb blockade. Sweeping the tip-sample bias voltage with the tip held at a fixed position results in periodic oscillations of the measured signal. The tip acts as a gate controlling the electron number in a quantum dot.

So what is the origin of the contour lines when the tip is scanned at a constant bias with respect to the 2DEG? We have already hinted to the answer in the previous section. Assuming that the bias is positive, electrons accumulating underneath the tip form a few-electron bubble. The bubble (or equivalently, quantum dot) is dragged

in the 2DEG following the motion of the tip and thus experiences different local electrostatic potentials. In locations where the potential energy for electrons is high, electrons are expelled from the dot. When it is low, they are drawn into it. As the tip scans across these positions of single electron transfer, the applied a.c. excitation causes an electron to move back and forth (i.e. resonate) between the dot and the surrounding 2DEG. A peak in the in-phase SCA signal is thus produced, in the same manner as described in Figure 6-2. Between the peaks, the dot is in the Coulomb blockade regime and the number of electrons in it remains fixed. A minimum of SCA signal is then detected and it is visualized in our 2D scans as the darker area in-between bright contour lines.

The resulting contour lines are essentially equipotentials that accurately map the background electrostatic potential in the 2DEG as seen by the electrons themselves. Such "maps" taken from other locations in the 2D layer appear in Figure 6-5. It is important to notice that the contours in our measurements do not intersect between them. This provides additional proof that they stem from a single electron bubble below the tip, rather than from a collection of localized "puddles" of electrons formed within the quantum Hall liquid. Such puddles may exist in the local maxima of the random electrostatic potential in the 2DEG even in the absence of the tip. In this latter case, a biased tip scanning across a puddle would act as a gate, changing the number of electrons in it. SCA images would then contain a superposition of rings from different puddles, each contributing its own high capacitance signal at regions where it would be energetically favorable to add or remove electrons to them. This scenario though, is not supported by our data and we conclude that there is indeed only one quantum dot formed in the 2DEG.

6.3.1 Evolution with Magnetic Field

The contour features in the images appear only in the high field side of the quantum Hall plateau as demonstrated in the example of Figure 6-6. These four images are taken at magnetic fields around $\nu = 1$. For the three scans taken at fields down to 5.8 Tesla, the Landau level filling factor in the bulk of the sample is $\nu < 1$, while

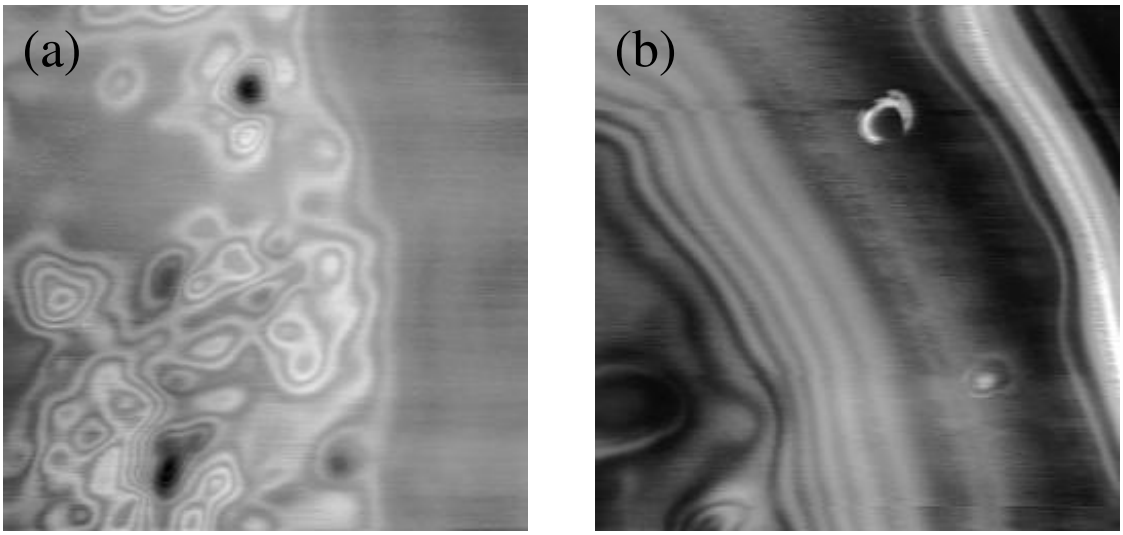

Figure 6-5: Maps of the electrostatic potential in the 2DEG. Images (a) and (b) originate from different sample areas. The tip-2DEG voltage is $V_{tip} = 1.0$ Volts for (a) and $V_{tip} = 2.0$ Volts for (b).

underneath the tip it is $\nu > 1$. The electron bubble at $\nu > 1$ is separated from the bulk by an incompressible strip with $\nu = 1$. The strip serves to isolate the bubble from the bulk and ensures charge quantization. However, as the magnetic field decreases, the degeneracy of Landau levels drops and the condition for exact integer filling at the strip location is satisfied at regions of lower density. This evolution is shown schematically in the lower part of Figure 6-6. Eventually, the filling factor becomes everywhere larger than one and the region of enhanced density merges with the rest of the electron layer. The bubble does not form and the contours are no longer present.

6.3.2 Evolution with Tip Bias

The observation of single-electron contours is inextricably linked to the presence of the mobile quantum dot (or bubble). This fact is further confirmed by following their evolution with tip-sample bias V_{tip}. As this voltage decreases, the contours shrink and gradually disappear around nulling. Figure 6-7 illustrates this behavior. In the absence of an electric field between the tip and the sample, the tip does not influence the density distribution in the 2DEG and the above mentioned quantum dot does

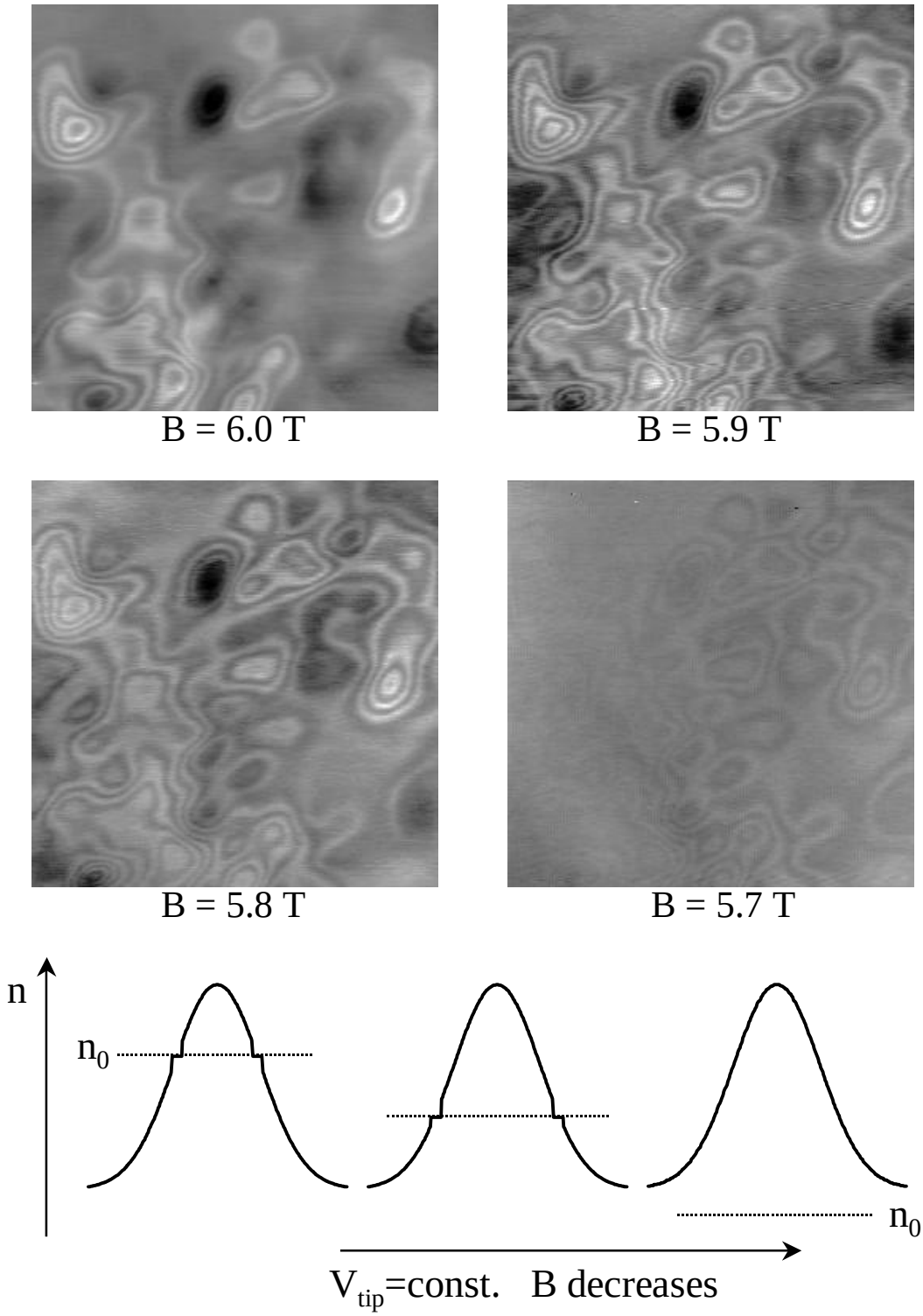

Figure 6-6: Evolution of contour features with magnetic field. The SCA images are $2.5 \times 2.5 \mu m$ large. A d.c. voltage of +1.0 Volts is applied to the tip with respect to the 2DEG, and creates a local enhancement in the electron density. Contours fade away and disappear as the field approaches the low field side of the $\nu = 1$ quantum Hall plateau.

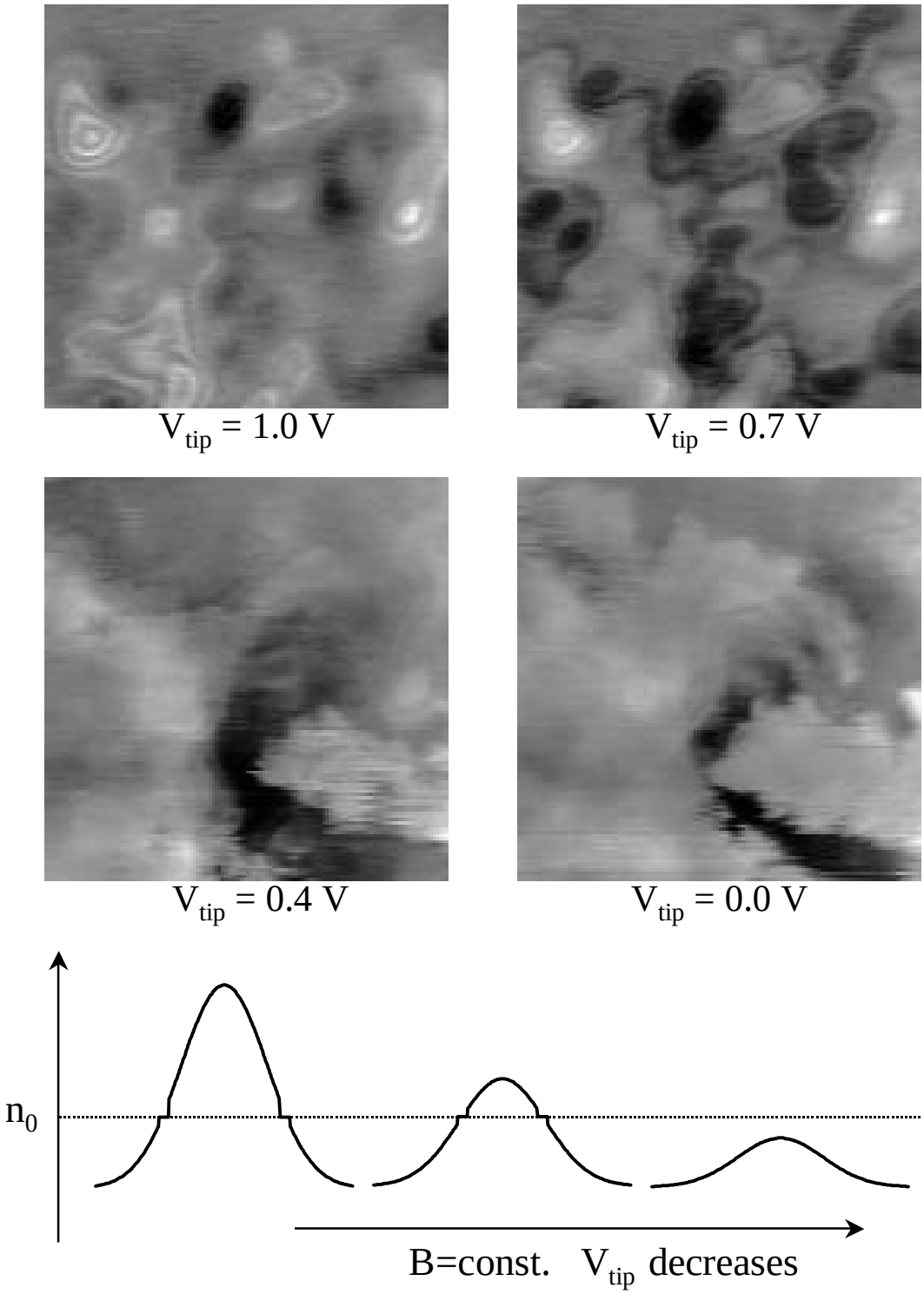

Figure 6-7: Evolution of contour features with tip-sample bias voltage. The scans are $2.5 \times 2.5 \mu m$ large and are all taken at 6.0 Tesla. Contour features are absent when V_{tip} approaches zero.

not form. The contrast seen in images taken with $V_{tip} = 0$, mainly originates due to compressibility or resistivity variations in the electron system, as we discussed in the previous chapters.

It is not surprising that our observations relating to contours evolving with B-field and V_{tip} can be presented within a unified picture. Specifically, changes induced by variations of magnetic field and electric field (i.e. tip-sample voltage) are quite similar. This is shown in Figure 6-8 with images of another sample region. We find that we can compensate for the change of a contour's size induced by magnetic field, by properly tuning the tip-sample voltage. Contours in successive SCA images at $\nu = 1$, characterized by the condition $\frac{dV}{dB} \approx 2\frac{V}{T}$, all maintain the same size. We can readily explain this observation by recalling that the quantum dot forms on top of an integer number of completely filled Landau levels. When the magnetic field increases, the degeneracy of the levels grows and they can accommodate more electrons. We supply these electrons by applying a larger voltage between the tip and the sample as illustrated in the schematic at the bottom of the latter Figure. We also expect the voltage required for compensating this difference in electron number, to be roughly proportional to the number of filled Landau levels. This result is in good agreement with the experiment.

6.3.3 Effects due to contaminated Tip

In some cases (see Figure 6-9), features on the submicrometer scale similar to those discussed above, persist at any voltage between the tip and the sample, including the nulling voltage for the Kelvin signal (i.e. the voltage designated as $V_{tip} = 0$ in our discussion). By measuring the Kelvin signal as a function of tip height, we have found that in such cases the tip does not have a uniform workfunction over its entire surface. Most probably, this results from GaAs debris partially covering areas of the scanning tip. As a result an electric field exists between the probe and the sample at any tip-sample voltage, even when the averaged Kelvin signal is zero. To avoid possible problems or artifacts in the images due to this effect, we carefully check the cleanliness of the tip before we begin measurements. The cleanliness of the tip has

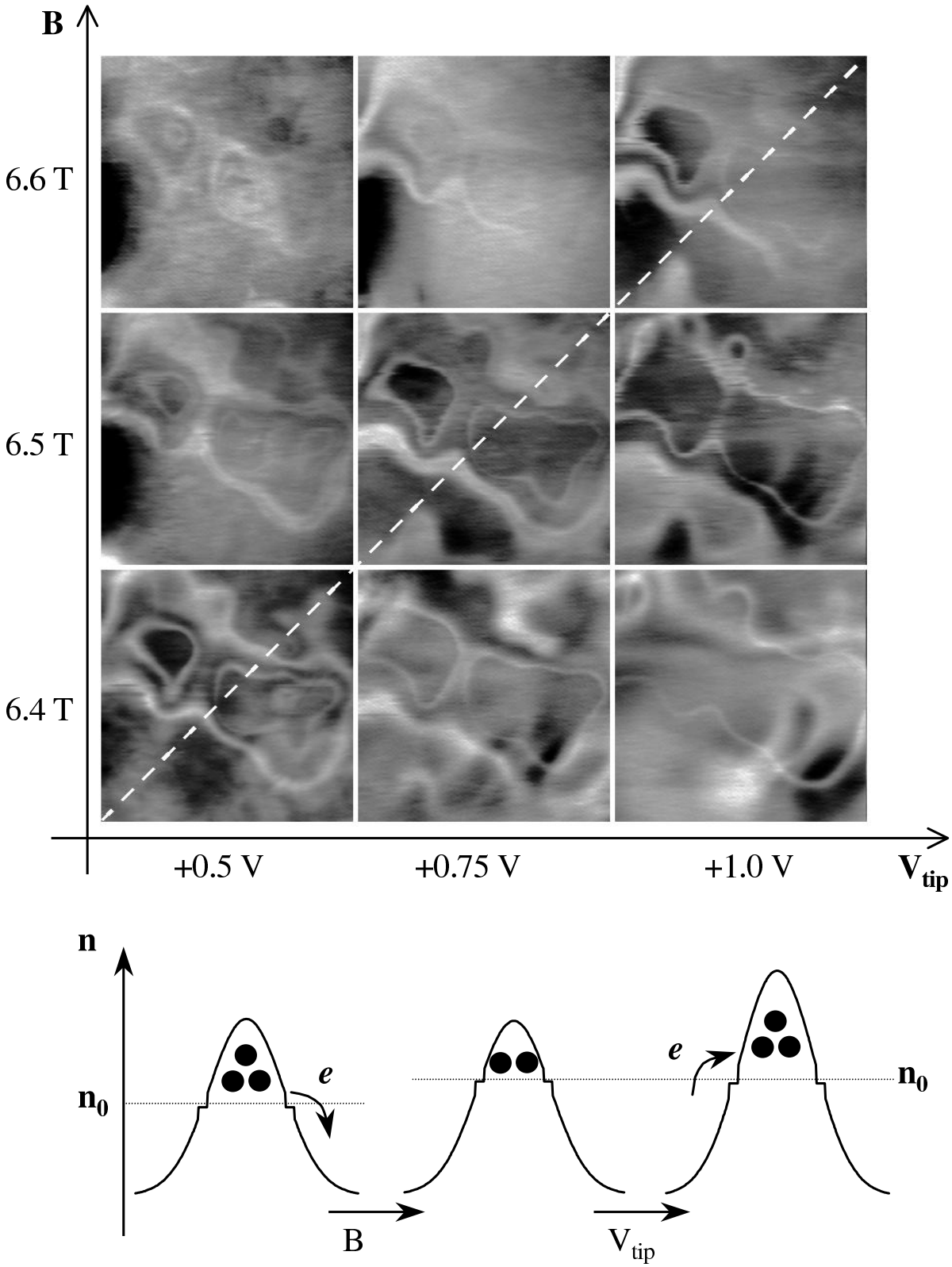

Figure 6-8: Series of 2×2 μm SCA images. Changes in contour size introduced by the tip voltage and magnetic field compensate each other, as seen in images along dashed diagonal line.

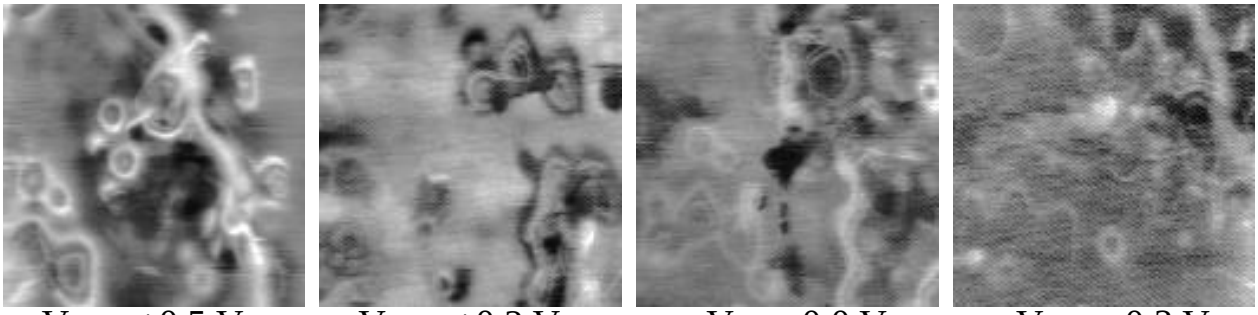

Figure 6-9: Signature of a "dirty" scanning tip. Features resembling single electron contours persist at all values of tip-voltage bias V_{tip}.

been ensured for all scans and data (excluding of course those in Figure 6-9) reported in this chapter.

6.4 Comparison between $\nu = 1$ and $\nu = 2$

The contour lines observed at $\nu = 1$ filling factor in the bulk of the 2DEG, reappear at fields corresponding to $\nu = 2$. The comparison is made in Figure 6-10. The contours observed at $\nu = 2$ display a weaker contrast, but they clearly encircle the same locations as at $\nu = 1$. The exact mechanism that gives rise to the contrast variation is not known with certainty. We surmise though that it most likely derives from the difference in electronic rates for tunneling across the incompressible strip that defines the quantum dot.

The similarity between images indicates that the electrostatic potential remains the same at both filling factors. The random potential fluctuations extend laterally by typically $\sim 0.5 - 1\ \mu m$. This scale is significantly larger than 50 nm, the width of the spacer layer that separates the 2DEG from donors. One expects however that random potential fluctuations due to remote ionized donors, should have a characteristic lateral length scale of about the spacer width [76]. Most probably in our sample, screening by the remaining electrons in the donor layer smoothens the background potential.

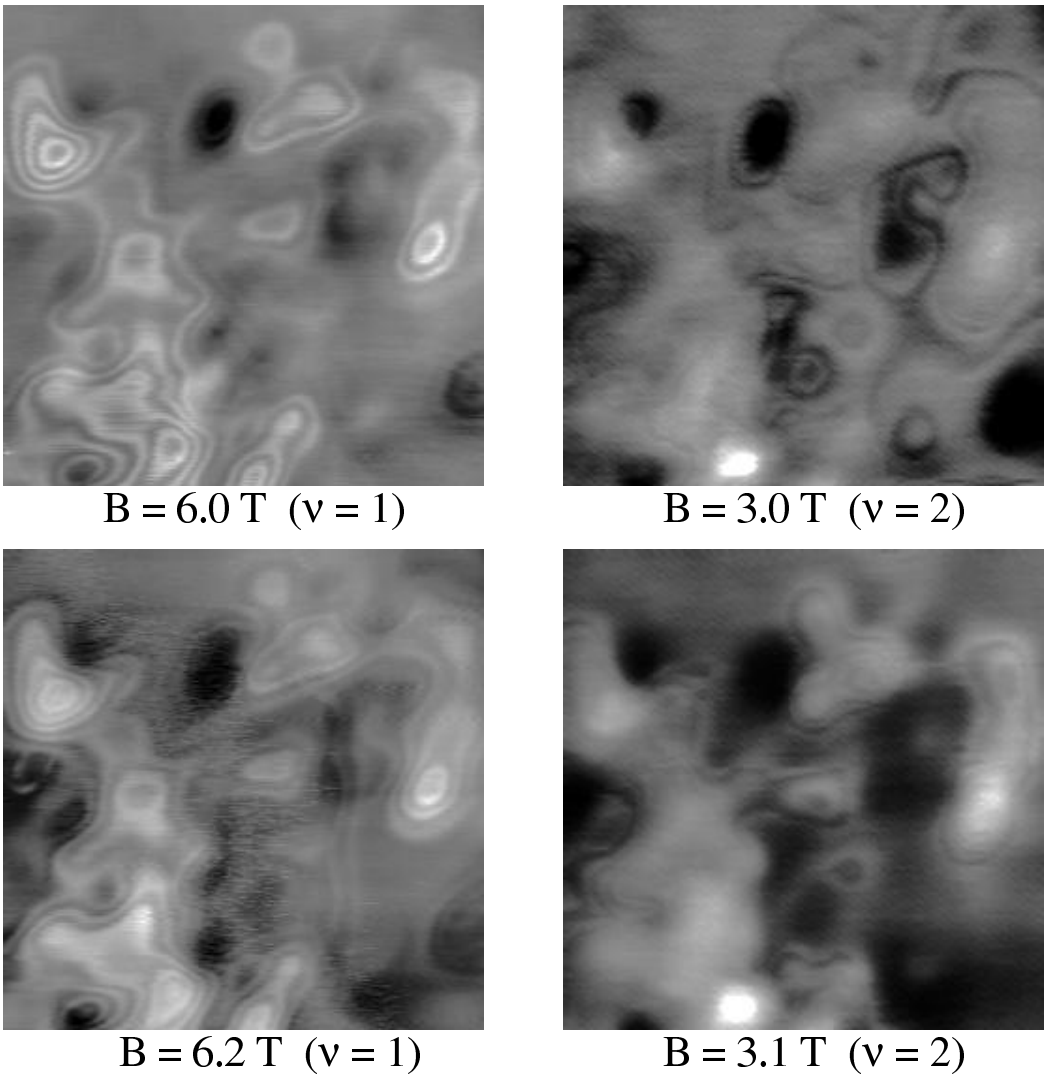

Figure 6-10: Maps of the electrostatic potential in the 2DEG at two different filling factors. $V_{tip} = 1.0$ Volt for all scans. Contour lines form around the same potential centers for both $\nu = 1$ and $\nu = 2$.

The size of the scanned quantum dot (estimated in section 6.7) should not prevent observation of smaller scale potential fluctuations. Single electron contours at select locations display very small radii of curvature, signaling steep potential peaks or troughs.

6.5 Characteristics of the Random 2DEG Potential

We now return to the examination of the contour lines depicted in Figure 6-8. As we have demonstrated, these results are typical of our measurements and will serve to illustrate the arguments put forward in this section.

Each contour line in the above mentioned figure marks the position within the 2DEG plane where the number of electrons in the quantum dot formed below the biased tip, changes by one. As the tip voltage V_{tip} decreases, the state with N electrons in the dot, drops in energy relative to the $N+1$ state. The former electron state is thus more energetically favorable and the contour line moves to a location where the background electrostatic energy is higher so that it compensates for the difference. Monitoring the evolution of SCA images at constant magnetic field we observe that contours shrink around the central locations as the voltage goes towards nulling. It follows that inside each contour the quantum dot has one more electron (and hence larger energy due to Coulomb interactions) than outside. Since the electronic charge carries a negative sign, we conclude that contour lines in Figure 6-8 surround two local potential minima as sensed by the electrons.

Different contours follow the same evolution as the tip voltage changes to move one contour to a position formerly occupied by another. For example, at a field of 6.5 Tesla, the inner contour at +1.0 Volt and the outer one at +0.5 Volt appear indistinguishable in size and shape. This behavior confirms our view of the dot, or bubble, as an electrostatic potential probe. Despite differences in dots created by different tip voltages, the resulting contours remain practically unchanged.

We have pointed out previously that our equipotential contours have the same meaning as topographic contours on a geographical map. To measure the amplitude of the electrostatic potential inside the 2DEG, we need to know the energetic separation between the single-electron contours. The line shape of the single electron peaks in a SCA trace measured as a function of the tip voltage at a fixed location, may provide us with the desired information [96]. This can be understood by considering the case of electrons tunneling through a quantum dot as depicted in Figure 6-1. The resolution of the corresponding single-electron peaks is determined by the energy spread of electrons in the source lead, from which they are trying to tunnel to the central island. The electronic state occupancy at thermodynamic equilibrium at temperature T is determined by the Fermi-Dirac distribution function,

$$f(E-\mu,T) = \frac{1}{e^{(E-\mu)/k_BT}+1} \tag{6.3}$$

where μ is the chemical potential and E is the single particle energy.

Let us also define the transmission probability of electrons incident to the island with energy E, as $T(E)$. The tunneling current I through the dot for non-interacting electrons, is then given by the weighted sum of the transmission probabilities of electrons over all energies [97]. We thus have:

$$I = \int \frac{e}{h} T(E)[f(E) - f(E-eV_{ds})]dE \tag{6.4}$$

In the regime where the drain-source voltage $V_{ds} \ll k_BT$ we get,

$$f(E) - f(E-eV_{ds}) \simeq eV_{ds}\frac{\partial f}{\partial E} \tag{6.5}$$

It then follows that the conductance G assumes the form:

$$G \propto \frac{\partial f}{\partial E} = -\frac{1}{4k_BT}\cosh^{-2}\left(\frac{E-\mu}{2k_BT}\right) \tag{6.6}$$

Consequently, returning back to our measurements, we fit the shape of the single

electron peaks responsible for the contours in Figure 6-8, with the derivative of the Fermi function. We assume that the thermal broadening of the peaks is determined by a temperature of 0.35 Kelvin and find that the energy at the bubble changes by $\sim$ 1 meV per 1 Volt change in the tip voltage. From that same Figure, as the tip voltage changes from +0.5 to +1.5 Volts at 6.6 Tesla, the innermost contour expands to span the entire scan area. We thus conclude that the range of the random potential in this region is about 1 meV.

6.6 Charging the Quantum Dot under the Tip

We have explained in previous sections that in the measuremenents described in this chapter, the tip acts as a gate controlling the charge inside a quantum dot. This fact is clearly demonstrated in Figure 6-11 that plots the SCA signal as a function of the tip (i.e. gate) bias. This signal is proportional to the tip-dot capacitance and is being fed to the lockin after the last amplification stage of our two-stage amplifier array. We remind here that we operate this array so that its gain is ≈ 10. One clearly sees the oscillatory behavior of the signal which we attribute to the motion of single electrons successively accumulating in the quantum dot as the gate voltage increases. The occupation of the dot formed under the tip, is of course zero when the tip-2DEG bias voltage is set to zero.

In quantum dot experiments involving vertical structures, the electron travels only a fraction of the distance between the plates of the tunnel capacitor. Therefore, the amount of charge induced on the gate due to a single electron tunneling event is $\frac{e}{\eta}$ [16]. The quantity η is known as the "lever arm". In our setup it is given by the ratio between the tip-2DEG and dot-2DEG capacitances. One then expects a voltage change of $\frac{e}{\eta C_{shunt}}$ at the balance point of the bridge.

Taking into account the gain of our amplifier and a value of $\sim 0.5pF$ for C_{shunt}, we see that the measured voltage change in Figure 6-11 resulting from single electron motion in and out of the dot, is much greater than one would ordinarily expect. One

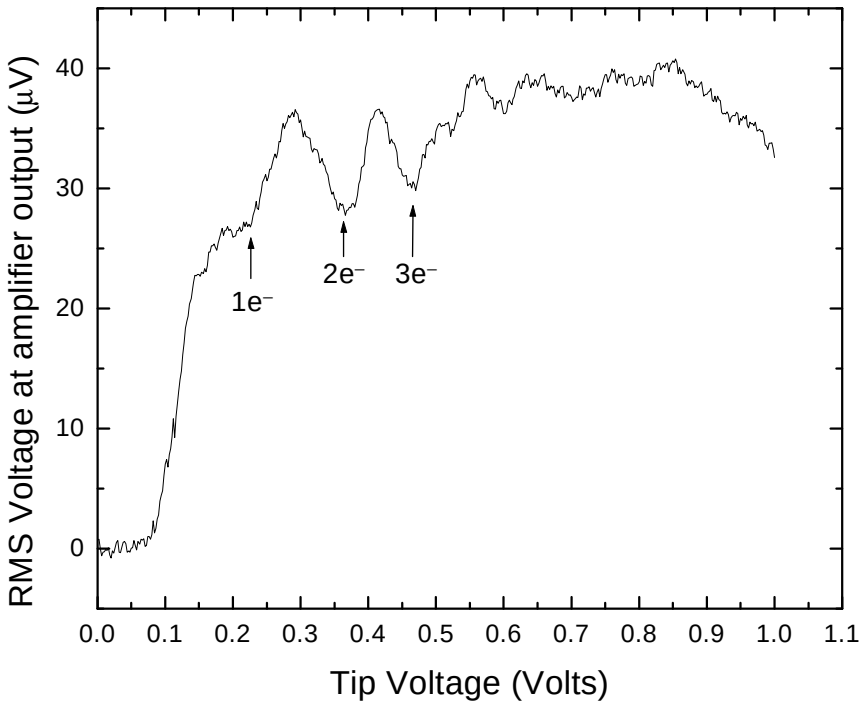

Figure 6-11: The rms signal at the output of the HEMT amplifier as a function of tip bias. The tip position remains fixed during the measurement.

has:

$$gain \times \frac{e}{C_{shunt}} \approx 3\mu V \tag{6.7}$$

and moreover, $\eta > 1$ which will further reduce the above estimate.

The origin of this discrepancy remains an open question. Further measurements accompanied by numerical modeling of the tip-2DEG system in the presence of a background potential, will reveal the exact shape and size of the quantum dot and provide an answer to this issue.

6.7 Size of the Quantum Dot. Dot Formation in Depletion

The number of electronic states per unit area (i.e. the degeneracy) of a full Landau level is:

$$N = \frac{eB}{hc} = \frac{B}{\Phi_0} \tag{6.8}$$

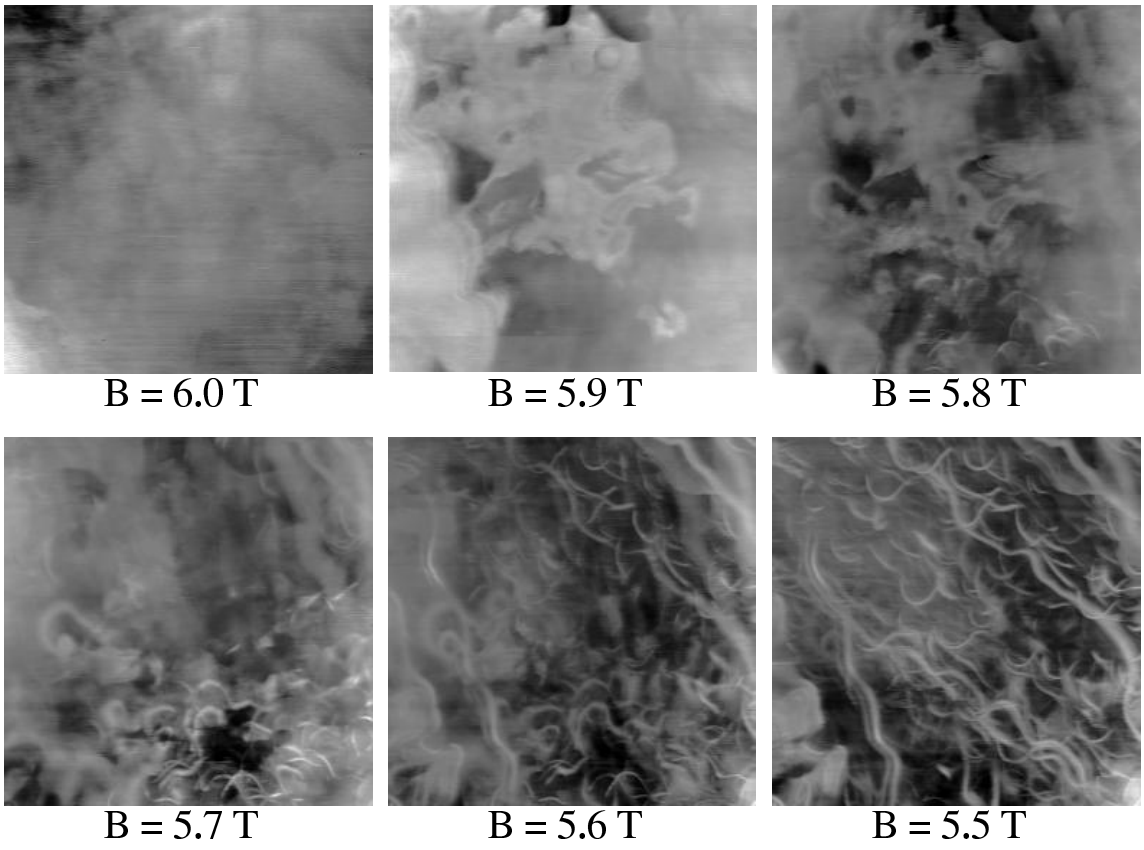

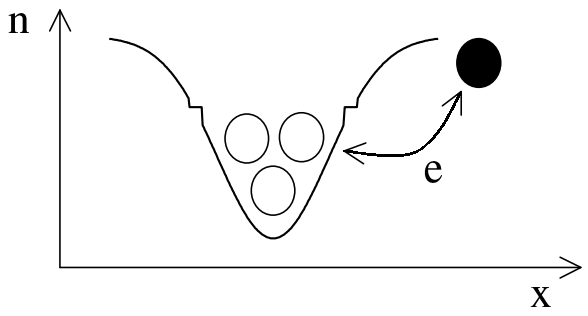

Figure 6-12: Evolution of 4.0×4.0 μm scans with magnetic field. A d.c. voltage of -0.5 Volts is applied to the tip with respect to the 2DEG, and locally depletes the electron gas below as shown in the lower schematic.

where Φ_0 is the flux quantum. In other words the degeneracy of Landau levels per unit area is given by the number of magnetic flux quanta threading it. Consequently, in our particular situation, adding one flux quantum per area of the quantum dot, adds one electronic state to each spin-split, filled Landau level. An electron is thus removed from the upper, partially filled Landau level that constitutes the dot, due to the availability of the extra state in the bulk. This result manifests itself in our measurements as a periodic signal with magnetic field. We here use it in order to determine the size of our quantum dot. From Figure 6-8 we observe that the contour lines move by a complete period as the field changes by ≈ 0.2 Tesla. The area A of the bubble is then found to be,

$$A = \frac{hc}{e\Delta B} \approx (140nm)^2 \tag{6.9}$$

Similar results are obtained from the images in Figure 6-6. Moreover, we note that the magnetic field period ΔB does not depend on location within the image. ΔB remains the same for contours centered around distinct potential peaks or valleys, indicating that the size of the quantum dot is not strongly affected by the random potential.

The discussion has so far concentrated on effects due to the formation of a bubble, as a region of enhanced electronic density underneath the scanning tip. A region of local depletion should in principle produce similar results with quasi-holes assuming the role of charge carriers. Charge accumulation scans when a negative voltage is applied on the tip with respect to the 2DEG, are presented in Figure 6-12. Features in the images are absent at the high-field side of the $\nu = 1$ Hall plateau, in agreement with the fact that we are now dealing with the tunneling of holes rather than electrons (cf. Figure 6-6). Contour lines appear briefly around $\nu \gtrsim 1$ but they are quickly replaced by open "wavy" lines whose behavior is hard to quantify. Although these lines might hint an asymmetry in the behavior between holes and electrons, we have not been able to determine their exact origin conclusively. This still remains an interesting question, open to further investigations.

6.8 Conclusion

Unlike our work described in previous chapters, we presented a novel method with which we probed a 2D electron gas by effectively embedding our sensor (the quantum dot) inside the system under study. Specifically, we have formed a mobile quantum dot within the electron layer by locally accumulating electron density underneath the scanning probe. The resulting Coulomb blockade patterns enable us to map the local potential inside the 2DEG as sensed by the electrons.

We also establish that the electron screening of the random potential remains almost unchanged between $\nu = 1$ and $\nu = 2$ quantum Hall plateaus and within each plateau.

Chapter 7

Future Prospects

In this thesis we have presented the novel scanning probe technique of subsurface charge accumulation (SCA) imaging, and used it to study a 2-dimensional electron gas in the regime of the integer quantum Hall effect. Our results have proven the success of the method in probing electronic systems buried underneath the surface of semiconductors, and its ability to obtain high resolution images of the charge distribution in the systems under study. In addition, the microscope and experimental setup has the sensitivity of detecting the motion of single electrons as we described in the previous chapter.

The combination of these characteristics, make the technique suitable for conducting a number of interesting experiments that have the potential to probe a wide range of mesoscopic systems. We shall concentrate here on aspects of our preliminary work concerning electronic systems in the low-density regime.

7.1 Samples

We have recently processed a GaAs/AlGaAs heterostructure with a grown-in back-gate. This sample was provided by Prof. M. Shayegan from Princeton University. A 2-D electron gas forms 78 nm below the surface as shown in Figure 7-1. The 2DEG is separated from the n+ GaAs substrate (i.e. the back-gate) by a 1.43 μm AlGaAs insulating layer. Separate electrical contacts to the electron layer and the conducting

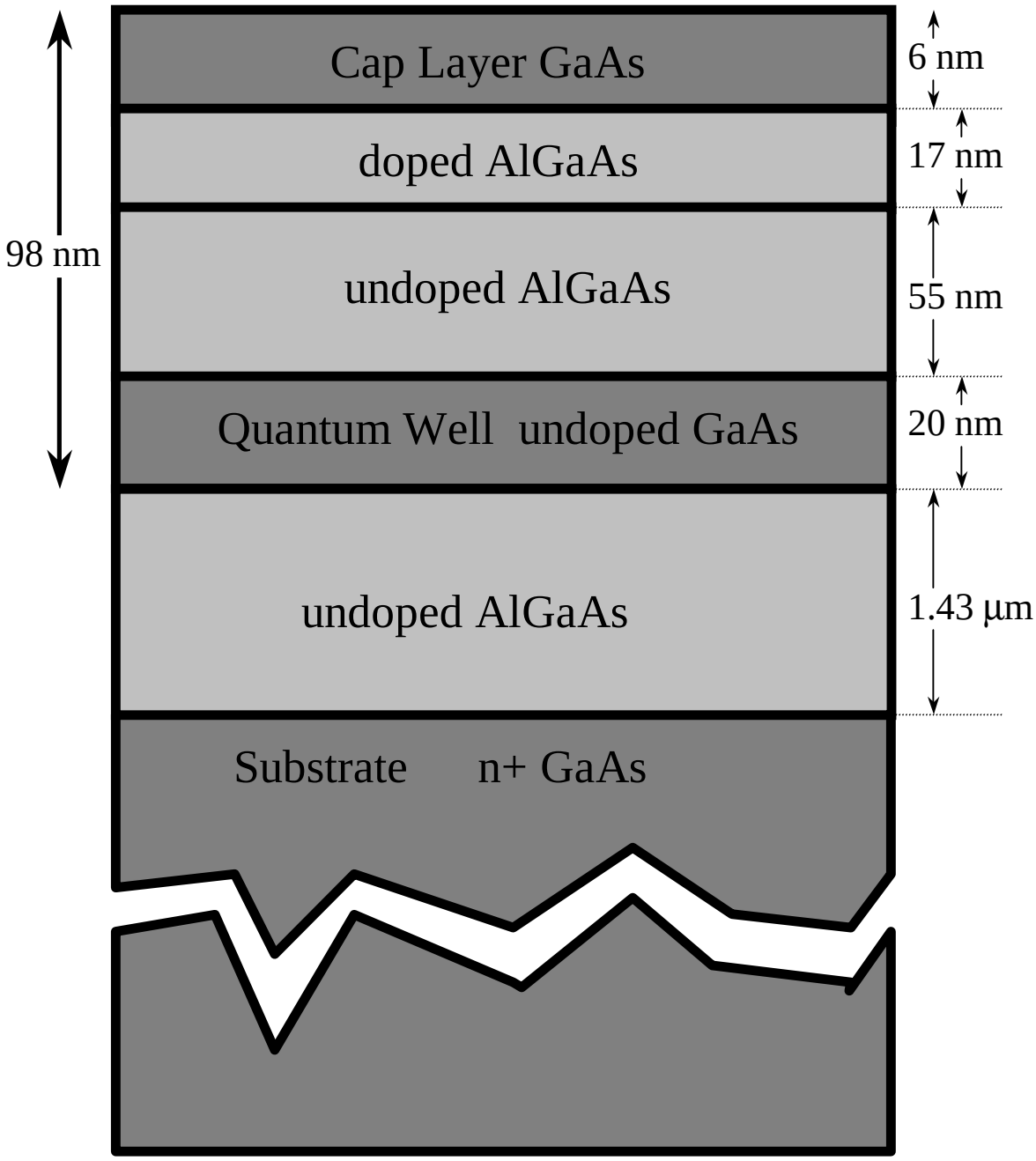

Figure 7-1: Layer structure of our backgated heterostructure (wafer M349).

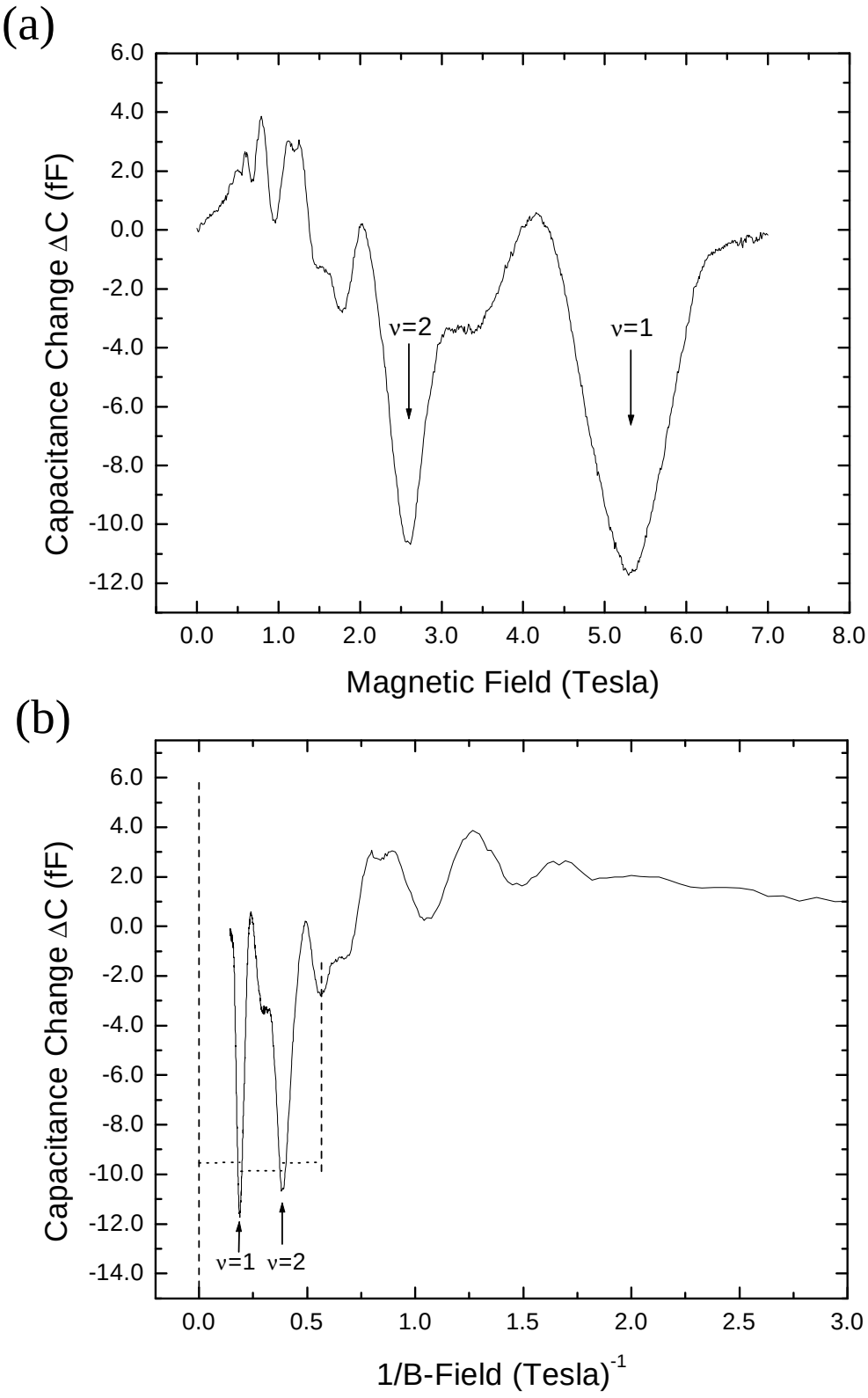

Figure 7-2: (a) Shubnikov-de Haas oscillations in the 2DEG capacitance, measured at 0.35 Kelvin. (b) Capacitance plotted versus inverse field. The three horizontal dotted lines are equal in length and are used to demonstrate the periodicity of the minima.

substrate are produced according to the procedure detailed in Appendix A. In addition, a 10 nm thick Cr gate in the shape of a fingered grating (see Figure 5-2(b)) has been evaporated on the sample surface. The 2DEG has a density of $1.3 \times 10^{11} cm^{-2}$, as deduced from preliminary capacitance measurements at a temperature of 0.35 Kelvin. The Shubnikov-de Haas capacitance oscillations for this sample appear in Figure 7-2. Filling factor $\nu = 1$ occurs at 5.3 Tesla in the bulk of the 2D layer and as a result, the 2DEG density is $1.3 \times 10^{11} cm^{-2}$.

The back-gate will allow us to directly vary the density n of the 2D electron gas in our sample. We can thus use it to perform measurements in the regime of low n.

7.2 Studies of low-density Fermion Systems

The behavior of a two-dimensional fermion layer is determined by the interplay between the Fermi energy E_F, the Coulomb interaction energy E_C and the thermal energy $k_B T$. One has that:

$$E_C = \frac{e^2}{4\pi\epsilon}\sqrt{\pi n} \tag{7.1}$$

The dimensionless parameter r_s measures the average interparticle distance in Bohr radii and can be expressed as the ratio of the Coulomb over the Fermi energy, i.e. $r_s = \frac{E_C}{E_F}$. Since $E_F \propto n$, it follows that $r_s \propto n^{-1/2}$. In other words, electron interactions dominate at low densities.

Theory predicts that in the absence of interactions, all states in a disordered 2D electron system at zero magnetic field are weakly localized, no matter how weak the disorder is. This result is also known as the scaling theory of localization [98]. As the disorder becomes strong there is a crossover to strong localization. It can be also shown that electrons may localize in disorderless systems if the density is low enough so that the Coulomb repulsion dominates [99]. In practice, both disorder and interactions are present inside actual 2-dimensional systems. Moreover, some experiments have demonstrated the existence of a metal-to-insulator phase transition in the regime where $r_s > 1$ [100, 101]. They indicate that the conductivity on the insulating, strongly localized side of the transition is characterized by very strong

temperature dependence whereas it is independent of temperature on the metallic side. Such a transition is in disagreement with the scaling theory of weak localization and may be a direct result of the important role of interactions in the system that this particular theory ignores.

A long time ago, Wigner [102] pointed that a degenerate Fermi gas is not the only possible state of electrons in the jellium model (i.e. electrons moving in a uniform background of equal and opposite charge). Electron or hole systems are expected to crystallize at very low densities, forming a Wigner crystal when $r_s \sim 37$ [103]. There has recently been some evidence for such a formation in a 2D hole system [104], though solid experimental results are still not available.

We thus see that a number of important questions relating to electron correlations and disorder, need to be answered in the regime of low densities. Since most experiments give information about the average properties and conductivity of a 2DEG, our scanning technique may prove invaluable in studies that reveal the actual charge distribution of carriers (in electron or hole samples), in conditions where $r_s > 1$.

7.3 The fractional quantum Hall effect

The results in this thesis have exclusively concentrated on studies of the integer quantum Hall effect. The extension to the fractional case is an obvious one and holds great promise since no results from scanning experiments are yet available in that regime. The construction of a scanning microscope able to operate inside our dilution refrigerator at a temperature of ~ 50 mK, is a step towards that direction.

The creation of a quantum dot in the fractional Hall liquid (cf. Chapter 6) may provide further direct evidence for the presence of fractional charges (quasi-particles) [105, 106, 107] that should in principle tunnel in and out of the dot [108]. At the same time, we may obtain direct information on the potential landscape, as experienced by a collection of quasi-particles.

Of course, there is no reason why further studies should be limited to 2D electron systems. Our instrument and technique is well suitable for probing a wide range of

physical systems and elucidating the behavior of their charged carriers. The exact nature of future measurements is only limited by the imagination and creativity of the experimenter. As a result, the technique of subsurface charge accumulation imaging, most certainly possesses the potential to keep generating a large number of diverse and exciting results.

Appendix A

Sample Processing and Ohmic contact fabrication

In this Appendix we describe the steps taken to prepare our GaAs/AlGaAs heterostructures before loading them into the capacitance microscope. The measurements presented in Chapters 3 and 4 were carried out in "plain" 2DEG samples. In other words, we did not define any patterns such as metallic gates, Hall bars etc., other than the required ohmic contacts through which the a.c. excitation passes to the electron system underneath the surface.

An ohmic contact should have a linear I-V characteristic and a relatively small ($\lesssim 5k\Omega$) resistance down to cryogenic temperatures for our purposes. For "plain" samples we produce Indium contacts by placing the metal on the sample surface and then annealing it. Indium diffuses inside the semiconductor (at least up to the depth of the 2D layer) and heavily dopes it so that the dominant conduction mechanism is tunneling rather than thermal excitation of electrons across a barrier. The result is an ohmic contact to the 2DEG that does not freeze out, even when subjected to extremely low temperatures.

This simple procedure is not suitable for samples where further processing steps will be performed. The reason is that a thick layer of metal will always remain on the sample and will prevent photolithography masks (that will most likely be used in some steps) from making a good contact with the surface. Even if one tries

to avoid this problem by flattening the region, indium metal is soft and will most likely contaminate the mask when pressed against it. As a result, for the samples used in Chapters 5 and 6, we evaporate contacts based on the Germanium/Gold system before we define and deposit the metal finger gate on the surface. Finally, we produce the backgated sample contacts described in Chapter 7, by using yet another combination of materials, namely Pd/Ge. The details of this last process that involves the formation of *shallow* ohmic contacts are given in section A.3.

Let us stress here that the exact processes that occur during metal-semiconductor ohmic contact formation, are not always fully understood. The exact parameters to be used for contact fabrication will vary according to factors related to the exact setup of individual annealer ovens, the purity of substrate surfaces and their metallization etc. The procedures described here were successful in our case, and may serve as useful reference for a similar undertaking.

A.1 Indium Ohmic Contacts

The cleanliness of the sample surface is of utmost importance for both the production of good ohmic contacts (of all types) as well as for the acquisition of meaningful data while scanning the sample with the tip in the microscope. To clean a sample we follow this procedure [21]:

1. Boil sample in 1,1,1 Trichloroethane (TCA) for 3 min.
2. Ultrasonic agitation in acetone for 5 min.
3. Ultrasonic agitation in methanol for 2 min. Blow N_2 on sample until fully dry.

To make the contacts we follow these steps:

1. Use a soldering iron with a clean tip and deposit small dots of pure indium metal on the regions where the contacts are to be made.
2. Anneal the semiconductor on a strip heater at 425° C for 10 minutes, while maintaining an environment of forming gas (95% N_2, 5% H_2) around the sample.

Eurotherm Temperature Controller			
Pr1 : 400	Pr2 : 600	Pr3 : 100	Pr4 : 800
Pl1 : 200	Pl2 : 410	Pl3 : 425	Pl4 : 0
Pd1: 0.5	Pd2: 0	Pd3: 10	Pd4: end

Table A.1: Temperature settings for annealing Indium ohmic contacts.

The exact parameters for the Eurotherm temperature controller used, are given in Table A.1.

3. Test the contacts resistance at 77 Kelvin (liquid nitrogen) using a probe station. If they work, test contacts once more at 4.2 Kelvin (in a dewar of liquid helium). If their I-V curve is still linear near the origin and their resistance is reasonable ($\approx 2 - 4\ k\Omega$ from our experience), load the sample into the microscope.

A.2 Fabrication for samples with Germanium/Gold/Nickel Ohmic Contacts and Top (Schottky) Gate

We used the GeAuNi system to produce contacts to the 2DEG in the samples used in Chapters 4 and 5. In addition, a metal gate in the shape of a grating was deposited on the surface. The procedure is outlined below:

1. Clean sample as instructed in section A.1.

2. Use negative photoresist NR8-1000 to define contact pads on the sample. With the resist acting as a mask, quick etch sample in a 1:8:1000 solution of $H_2SO_4/H_2O_2/H_2O$ for ~ 10 seconds.

3. Glue sample on a glass slide with PMMA and bake at 130° C, so that PMMA hardens.

4. Load sample into an evaporator and deposit metallic layers in the following sequence: Nickel 100 Å, Gold-Germanium alloy (88% Au, 12% Ge by weight) 1100 Å.

5. Perform metal lift-off in acetone with ultrasonic agitation to remove the metallization from the resist-covered areas. Anneal sample on strip heater at 435° C for 1 minute in forming gas. For the exact temperature controller settings refer to Table A.2.

6. Test contacts by measuring their I-V characteristics with a probe station at 77 Kelvin.

7. Pattern finger gate on sample with photolithography using NR8-1000 negative resist.

8. Glue sample on glass slide with PMMA, load into evaporator and deposit 100 Å of chromium.

9. Perform metal lift-off in acetone with ultrasonic agitation.

10. Define gate contact pad using negative photoresist. The pad area should overlap with the edge of the already present chromium gate. Then perform another evaporation and deposit 50 Å of chromium and 1000 Å of gold.

11. Metal lift-off as above concludes the process.

12. Attach sample with silver epoxy on a piece of i-GaAs where gold pads have been previously defined. Wire-bond to the ohmic contacts and the gate pad so that they become easily accessible.

Eurotherm Temperature Controller			
Pr1 : 400	Pr2 : 600	Pr3 : 100	Pr4 : 800
Pl1 : 200	Pl2 : 420	Pl3 : 435	Pl4 : 0
Pd1: 0.5	Pd2: 0	Pd3: 1	Pd4: end

Table A.2: Temperature settings for annealing GeAuNi ohmic contacts.

A.3 Fabrication for backgated samples with Palladium/Germanium/Gold shallow Ohmic Contacts and Top (Schottky) Gate

The sample described in Chapter 7 has a built-in backgate through which the electronic density in the 2D layer may be modulated. The backgate is effectively the n-doped GaAs substrate on top of which the rest of the heterostructure is grown (see schematic in Figure 7-1). As a result, we require independent contacting of the 2DEG and the backgate. However, the proximity of the n+ layer to the plane of the 2DEG makes the creation of contacts to the electron gas particularly challenging. The AuGeNi metallization described previously diffuses into the wafer and forms spikes that may extend to depths of microns [109]. It is thus not suitable for our case since it would electrically short the 2DEG with the backgate. We circumvent this problem by employing a different metallization that is based on the Palladium/Germanium/Gold combination [110, 111, 112]. The diffusion of dopants in the Pd/Ge/Au system is restricted to less than 20 nm resulting in the formation of a very shallow ohmic contact [113]. We contact the backgate by producing a AuGeNi contact at the back side of the sample (the backgate is very thick and there is no concern that the metal will reach the 2D layer).

The back side of the original backgated wafer is covered in gallium that needs to be removed prior to making the back contact. In addition, that same side is very rough and needs to be smoothened in order to ensure good thermal contact of the sample with the heater while annealing. The steps underlying the whole procedure are the following:

1. Glue sample, face down, on a glass slide using photoresist. Put the sample in hydrochloric acid to dissolve gallium from the back side. Heating speeds the process considerably, but the temperature should be kept low enough ($\leq 70^\circ$ C) so that the photoresist protective layer is not damaged. Hydrochloric acid slowly etches GaAs so contact with the sample surface should be avoided.

2. If the back side of the sample is not smooth, polish it using fine grid sandpaper. This step is required since good, uniform thermal contact between the sample and the strip heater is essential when annealing.

3. Glue sample, face down onto a glass slide using PMMA, then bake for 1 minute at 130° C, so that PMMA hardens.

4. Perform a quick etch in a 1:8:1000 solution of $H_2SO_4/H_2O_2/H_2O$ for $\sim$ 10 seconds.

5. Load sample into an evaporator and deposit the following layers: Nickel 100 Å, Gold-Germanium alloy (88% Au, 12% Ge by weight) 1100 Å.

6. Anneal sample on strip heater at 435° C for 1 minute in forming gas. For the exact temperature controller settings refer to Table A.2. The contact to the backgate is now formed.

7. Use negative photoresist NR8-1000 to define contact pads on the sample. It is crucial that the pads are located some distance *away* from the sample edges, so that no metal may be deposited or accidentally touch the edges of the wafer.

8. Calibrate a 1:8:1000 solution of $H_2SO_4/H_2O_2/H_2O$ using a surface profilomter. With the resist acting as a mask, etch a recess in the exposed contact pad areas. This will bring the contact metallization (to be evaporated in the next step) 100 to 150 Å away from the plane of the 2D electron gas. In our case the etch rate was 38 nm/min and we etched for 103 seconds.

9. Glue sample, face up, on a glass slide with PMMA and bake at 130° C, so that PMMA hardens. Then load sample into an evaporator and deposit metallic layers in the following sequence: Palladium 500 Å, Germanium 1290 Å, Gold 1400 Å.

10. Perform metal lift-off in acetone with ultrasonic agitation to remove the metallization from the resist-covered areas. Anneal sample on strip heater at 375° C

for 6 minutes while maintaining a constant flow of forming gas. Table A.3 shows the exact temperature controller settings.

11. Test contacts by measuring their I-V characteristics with a probe station at 77 Kelvin and then at 4.2 Kelvin. In our case they remained ohmic down to 4.3 K with a resistance of 310 Ω between neighboring contacts.

12. Pattern finger gate on the sample following steps 7 to 11 from section A.2.

13. Use silver (conducting) epoxy to glue sample on a piece of i-GaAs with predefined gold pads. The contact to the backgate is thus accessible, as are the contacts to the top gate and the 2DEG.

Eurotherm Temperature Controller			
Pr1 : 400	Pr2 : 600	Pr3 : 100	Pr4 : 800
Pl1 : 200	Pl2 : 340	Pl3 : 375	Pl4 : 0
Pd1: 0.5	Pd2: 0	Pd3: 6	Pd4: end

Table A.3: Temperature settings for annealing PdGeAu ohmic contacts.

Appendix B

Cooling and Warming the Microscope from liquid Helium temperatures

As we described in Chapter 2, the microscope body is bolted at the end of a standard Oxford Instruments probe that is inserted inside a top-loading Helium-3 cryostat. Central to the microscope's operation are the piezoelectric tubes responsible for scanning the tip and moving the sample holder in the x, y, and z directions with respect to the tip. These ceramic tubes are susceptible to cracking when subjected to thermal stress. As a result, it is important to cool down and warm up the microscope slowly, in order to avoid damaging these ceramic elements.

B.1 Cooldown procedure

A calibrated resistor is attached near the bottom of the microscope's brass body and is used as a thermometer to monitor the instrument's cooling rate. To cool the microscope to 4.2 Kelvin from room temperature, we follow the steps outlined below:

1. Ground all signal and transistor cables as well as all high voltage lines that connect to the quadrants of the piezo tubes. Place the Oxford probe on top of

the He-3 cryostat and pump its interior to a high vacuum ($\sim 10^{-5}$ mbar).

2. Open the gate valve and lower the probe approximately two feet. The sorb temperature at this point should be around 5 Kelvin so that the He-3 pressure in the sample space is minimal. The idea now, is to introduce a small amount of He-3 into this space that will act as exchange gas and cool down the microscope in a controlled manner.

3. Turn the sorb heater on and start heating the sorb until the He-3 pressure in the sample space is about 15-20 mbar, as monitored with the gauge in the He-3 "dumps" vessel. This pressure must be maintained throughout the cooling process. So, if needed adjust the sorb heater power and/or the sorb pump settings accordingly.

4. Lower the probe slowly while constantly monitoring the microscope's temperature using the calibrated resistor. A cooling rate of $\sim$ 1-2 Kelvin/minute should be safe for the instrument.

5. Proceed in that manner until the probe is fully lowered in the cryostat.

6. When all temperatures have stabilized, the transistors in the amplifier array can be ungrounded and tested if necessary.

7. Condensing the He-3 gas does not require any special precautions other than maintaining the transistors and the piezo tubes grounded. The procedure is carried out as described in the Helium-3 system manual provided by Oxford Instruments. After the base temperature of the system stabilizes at around 0.35 Kelvin, the transistors, sample and piezo tube quadrants can be ungrounded and powered up. The sample is then positioned within scanning range from the tip and measurements can begin.

B.2 Warmup procedure

The following procedure can be used when one wishes to warm the microscope to room temperature.

1. With all cables (transistors, sample, piezo tubes) grounded, start lifting the Oxford probe from the cryostat. The pressure in the sample space should now be kept to a minimum so that no exchange gas is present in that volume. To that effect, maintain the sorb temperature below 10 Kelvin while raising the probe.

2. Lift the probe until it is located about 2 feet from its fully raised position. This procedure may be carried out fast since in the absence of any exchange gas the microscope remains cold.

3. Wait for $\sim$ 30 mins before raising the probe an extra foot. Wait for another $\sim$ 1.5 hrs and then raise the probe fully. The sample space gate valve on the cryostat should be closed at this point.

4. Leave the microscope to warm up slowly by radiation. Its temperature can be monitored using the calibrated resistor, but no further action is required until it reaches ambient temperature. When this occurs (typically several hours later), double check that the cryostat gate valve is fully closed and introduce nitrogen gas in the evacuated probe sample space. The probe can then be removed from the top of the Helium-3 system.

Appendix C

Kelvin Probe Considerations

In Chapter 2 we described how we can operate the microscope in Kelvin probe mode in order to determine the contact potential V_k between the scanning tip and GaAs surface of the sample. Let C denote the tip-sample capacitance and ω the frequency of the vibrational motion of one capacitor plate (the sample) relative to the other (the tip). It then follows that:

$$Q = C(V - V_k) \Rightarrow I = \frac{dQ}{dt} = \frac{dC}{dt}(V - V_k) \tag{C.1}$$

We however use a lockin amplifier to effectively measure the voltage across a transistor circuit having a shunting capacitance C_s. So:

$$V_{meas} = \frac{Q}{C_s} \Rightarrow \frac{dV_{meas}}{dt} = \frac{1}{C_s}\frac{dQ}{dt} \tag{C.2}$$

Using Equation C.1 along with the fact that $z = z_0 \sin \omega t$, the rate of change of the measured voltage becomes:

$$\frac{dV_{meas}}{dt} = \frac{V - V_k}{C_s}\frac{dC}{dz}\frac{dz}{dt} = \frac{V - V_k}{C_s}\frac{dC}{dz}\omega z_0 \cos \omega t \tag{C.3}$$

or, equivalently:

$$\frac{dV_{meas}}{dt} = \alpha \frac{dC}{dz} z(t) \tag{C.4}$$

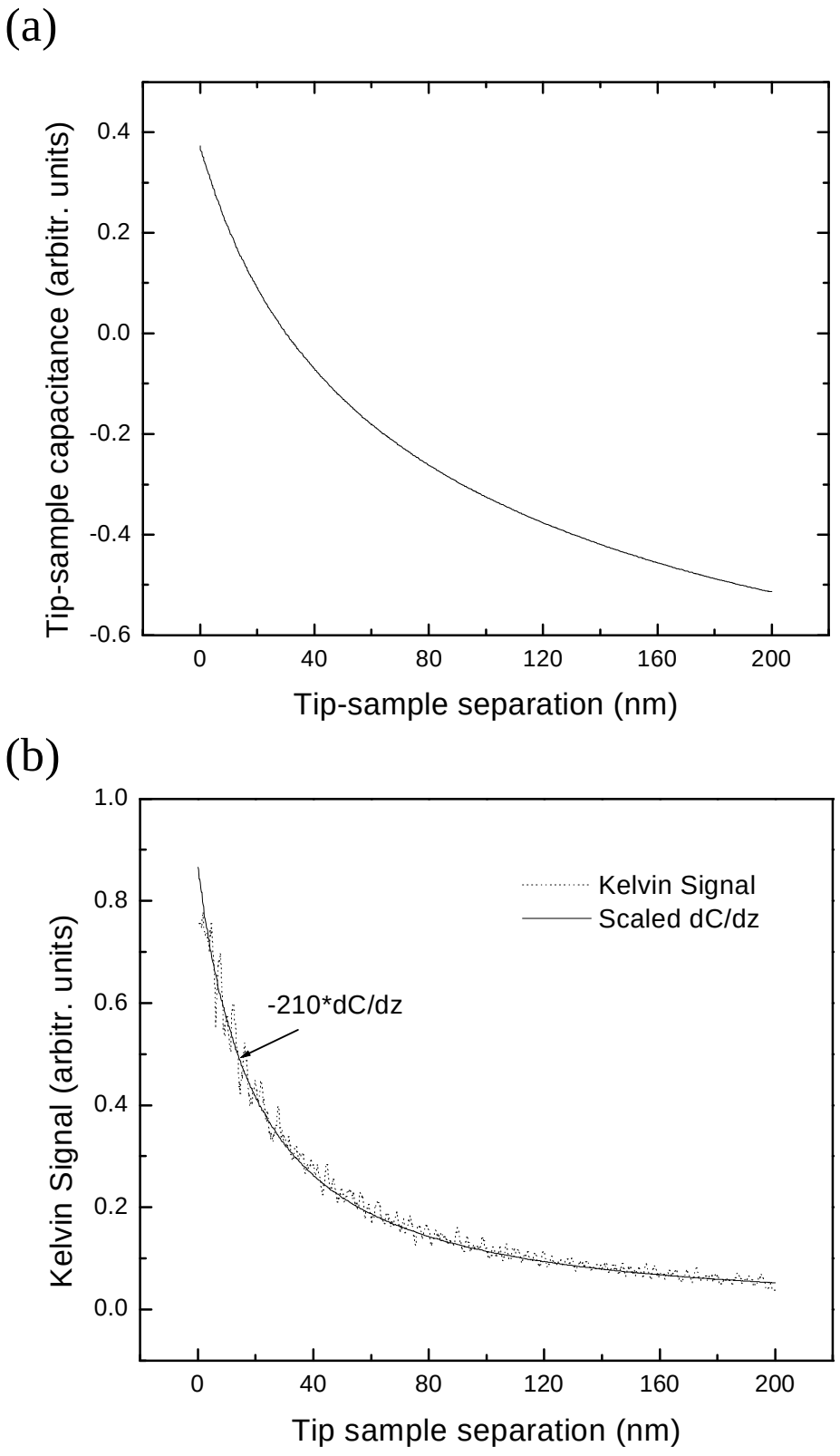

Figure C-1: (a) Tip-sample capacitance as a function of vertical tip distance from the surface. (b) Kelvin probe signal versus tip height (dotted line), compared with the derivative of the capacitance signal from (a). The Kelvin signal is measured away from nulling, with $V - V_k = 04V$.

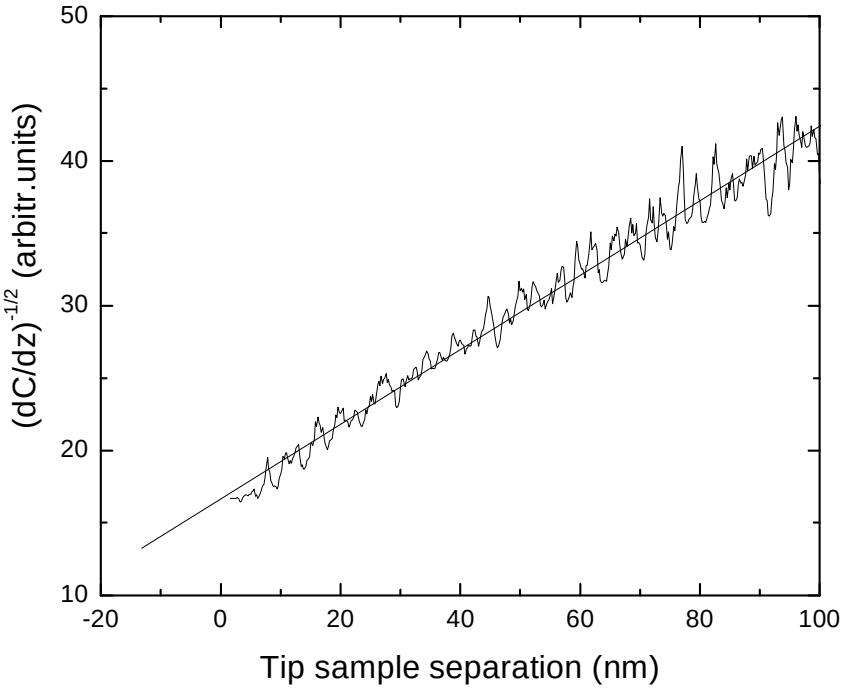

Figure C-2: Testing Equation C.5. The straight line is a fit to the data.

where α is a constant. Figure C-1(a) plots the tip-sample capacitance signal as the probe moves away from the surface in the vertical direction.

The Kelvin signal measured as a function of tip-sample separation at the same spot, appears in Figure C-1(b). Equation C.4 dictates that it should be proportional to the derivative of the corresponding capacitance signal. Indeed, as shown in the Figure, the agreement between the Kelvin signal and the appropriately scaled magnitude of $\frac{dC}{dz}$ calculated from the data in Figure C-1(a), is particularly good.

In some of our previous discussions, we modeled the tip-2DEG system as a parallel plate capacitor. In that case, the capacitance C should vary as:

$$C = \frac{A}{z-\beta} + B \Rightarrow \frac{1}{\sqrt{\frac{dC}{dz}}} \propto (z-\beta) \tag{C.5}$$

A, B, β are constants. Figure C-2 plots the quantity $\frac{1}{\sqrt{\frac{dC}{dz}}}$ as a function of z, again as extracted from the C vs. z plot of Figure C-1(a). A straight line provides a reasonable fit to the data, and partly justifies our use of the above mentioned simple capacitance model.

Bibliography

[1] T. Ando, A.B. Fowler, and F. Stern. Electronic properties of two dimensional systems. *Rev. Mod. Phys.*, 54:437, 1982.

[2] R.B. Laughlin. Quantized Hall conductivity in two dimensions. *Phys. Rev. B*, 23:5632, 1981.

[3] B.I. Halperin. Quantized Hall conductance, current-carrying edge states, and the existence of extended states in a two-dimensional disordered potential. *Phys. Rev. B*, 25:2185, 1982.

[4] D.C. Tsui, H.L. Stormer, and A.C. Gossard. Two-dimensional magnetotransport in the extreme quantum limit. *Physical Review Letters*, 48:1559, 1982.

[5] K. von Klitzing, G. Dorda, and M. Pepper. New method for high-accuracy determination of the fine-structure constant based on quantized Hall resistance. *Physical Review Letters*, 45:494, 1980.

[6] R.E. Prange and S.M. Girvin, editors. *The Quantum Hall Effect.* Springer-Verlag, 1990.

[7] T. Chakraborty and P. Pietiläinen, editors. *The quantum Hall effects: integral and fractional.* Springer-Verlag, 1995.

[8] G. Binnig and H. Rohrer. Scanning tunneling microscopy. *Helv. Phys. Acta*, 55:726, 1982.

[9] G. Binnig, H. Rohrer, C. Berger, and E. Weibel. Tunneling through a controllable vacuum gap. *Appl. Phys. Lett.*, 40:178, 1982.

[10] G. Binnig, H. Rohrer, C. Berger, and E. Weibel. Surface studies by scanning tunneling microscopy. *Physical Review Letters*, 49:57, 1982.

[11] G. Binnig and H. Rohrer. Scanning tunneling microscopy - from birth to adolescence. *Rev. Mod. Phys*, 56:615, 1987.

[12] C.C. Williams, J. Slinkman, W.P. Hough, and H.K. Wickramasinghe. Lateral dopant profiling with 200 nm resolution by scanning capacitance microscopy. *Applied Physics Letters*, 55:1662, 1989.

[13] S. Lanyi, J. Torok, and P. Rehurek. Imaging conducting surfaces and dielectric films by a scanning capacitance microscope. *Journal of Vacuum Science & Technology B*, 14:892, 1996.

[14] R. Wiesendanger and H.J. Guntherodt, editors. *Scanning Tunneling Microscopy II.* Springer-Verlag, 1995.

[15] R.C. Ashoori, H.L. Stormer, J.S. Weiner, L.N. Pfeiffer, S.J. Pearton, K.W. Baldwin, and K.W. West. Single-electron capacitance spectroscopy of discrete quantum levels. *Physical Review Letters*, 68:3088, 1992.

[16] R.C. Ashoori, H.L. Stormer, J.S. Weiner, L.N. Pfeiffer, S.J. Pearton, K.W. Baldwin, and K.W. West. Single-electron capacitance spectroscopy of a few electron box. *Physica B*, 189:117, 1993.

[17] D.W. Pohl. Dynamic piezoelectric translation devices. *Rev. Sci. Instrum.*, 58:54, 1986.

[18] D.W. Pohl. Sawtooth nanometer slider: A versatile low voltage piezoelectric translation device. *Surf. Sci.*, 181:174, 1987.

[19] K. Besocke. An easily operable scanning tunneling microscope. *Surf. Sci.*, 181:145, 1987.

[20] S. Urazhdin, I.J. Maasilta, S. Chakraborty, I. Moraru, and S.H. Tessmer. High-scan-range cryogenic scanning probe microscope. *Rev. Sci. Instrum.*, 71:4170, 2000.

[21] M. Brodsky. *Charging of Small Two-Dimensional Electron Puddles.* PhD thesis, Massachusetts Institute of Technology, 2000.

[22] P. Horowitz and W. Hill. *The Art of Electronics.* Cambridge University Press, 1989.

[23] J. Sudijono, M.D. Johnson, C.W. Snyder, M.B. Elowitz, and B.G. Orr. Surface evolution during molecular-beam epitaxy deposition of GaAs. *Physical Review Letters*, 69:2811, 1992.

[24] M.J. Yoo, T.A. Fulton, H.F. Hess, R.L. Willett, L.N. Dunkleberger, R.J. Chichester, L.N. Pfeiffer, and K.W. West. Scanning single-electron transistor microscopy: Imaging individual charges. *Science*, 276:579, 1997.

[25] Lord Kelvin. *Philos. Mag.*, 46:82, 1898.

[26] P.P. Craig. Direct observation of stress-induced shifts in contact potentials. *Physical Review Letters*, 22:700, 1969.

[27] M. Tanimoto and O. Vatel. Kelvin probe force microscopy for characterization of semiconductor devices and processes. *J. Vac. Sci. Technol. B*, 14:1547, 1996.

[28] H. Baumgartner and H.D. Leiss. Micro Kelvin probe for local work-function measurements. *Rev. Sci. Instrum.*, 59:802, 1988.

[29] C.G. Vayenas, S. Bebelis, and S. Ladas. Dependence of catalytic rates on catalyst work function. *Nature*, 345:625, 1990.

[30] W. Shockley, H.J. Queisser, and W.W. Hooper. Charges on oxidized silicon surfaces. *Physical Review Letters*, 11:489, 1963.

[31] W. Nabhan, B. Equer, A. Broniatowski, and G. de Rosny. A high-resolution scanning Kelvin probe microscope for contact potential measurements on the 100 nm scale. *Rev. Sci. Instrum.*, 68:310, 1997.

[32] D.C. Tsui, H.L. Stormer, and A.C. Gossard. Zero-resistance state of two-dimensional electrons in a quantizing magnetic field. *Physical Review B*, 25:1405, 1982.

[33] B.B. Goldberg. Optical investigations of the integer and fractional quantum Hall effects: energy plateaus, intensity minima, and line splitting in band-gap emission. *Physical Review Letters*, 65:641, 1990.

[34] I.V. Kukushkin. Evidence of the triangular latice of crystallized electrons from time resolved luminescence. *Physical Review Letters*, 72:3594, 1994.

[35] J.P. Eisenstein. Density of states and de Haas-van Alphen effect in two-dimensional electron systems. *Physical Review Letters*, 55:875, 1985.

[36] R.C. Ashoori and R.H. Silsbee. The Landau level density of states as a function of Fermi energy in the two-dimensional electron gas. *Solid State Commun.*, 81:821, 1992.

[37] T.P. Smith, B.B. Goldberg, P.J. Stiles, and M. Heiblum. Direct measurement of the density of states of a two-dimensional electron gas. *Physical Review B*, 32:2696, 1985.

[38] S.H. Tessmer, P.I. Glicofridis, R.C. Ashoori, L.S. Levitov, and M.R. Melloch. Subsurface charge accumulation imaging of a quantum Hall liquid. *Nature*, 392:51, 1998.

[39] M.A. Topinka, B.J. LeRoy, S.E.J. Shaw, E.J. Heller, R.M. Westervelt, K.D. Maranowski, and A.C. Gossard. Imaging coherent electron flow from a quantum point contact. *Science*, 289:2323, 2000.

[40] K.L. McCormick, M.T. Woodside, M. Huang, M. Wu, P.L. McEuen, C. Duruoz, and J.S. Harris Jr. Scanned potential microscopy of edge and bulk currents in the quantum Hall regime. *Physical Review B*, 59:4654, 1999.

[41] Y.Y. Wei, J. Weis, K.v. Klitzing, and K. Eberl. Single-electron transistor as an electrometer measuring chemical potential variations. *Appl. Phys. Lett.*, 71:2514, 1997.

[42] M.A. Eriksson, R.G. Beck, M. Topinka, J.A. Katine, R.M. Westervelt, K.L. Campman, and A.C. Gossard. Cryogenic scanning probe characterization of semiconductor nanostructures. *Appl. Phys. Lett.*, 69:671, 1996.

[43] H.B. Chan. *Tunneling Spectrocopy of the Two-Dimensional Electron Gas*. PhD thesis, Massachusetts Institute of Technology, 1999.

[44] H.B. Chan, P.I. Glicofridis, R.C. Ashoori, and M.R. Melloch. Universal linear density of states for tunneling into the two-dimensional electron gas in a magnetic field. *Physical Review Letters*, 79:2867, 1997.

[45] J.P. Eisenstein, L.N. Pfeiffer, and K.W. West. Negative compressibility of interacting two-dimensional electron and quasiparticle gases. *Physical Review Letters*, 68:674, 1992.

[46] H. Nielsen, S.V. Kravchenko, V.M. Pudalov, and D.A. Rinberg. On negative dielectric permittivity in the quantum Hall regime. *Physica B*, 184:323, 1993.

[47] C.d.C. Chamon and X.G. Wen. Sharp and smooth boundaries of quantum Hall liquids. *Physical Review B*, 49:8227, 1994.

[48] A.H. McDonald, S.R.E. Young, and M.D. Johnson. Quantum dots in strong magnetic fields: Stability criteria for the maximum density droplet. *Aust. J. Phys.*, 46:345, 1993.

[49] P.L. McEuen, E.B. Foxman, J. Kinaret, U. Meirav, and M.A. Kastner. Self-consistent addition spectrum of a Coulomb island in the quantum Hall regime. *Physical Review B*, 45:11419, 1992.

[50] A.A. Koulakov, M.M. Fogler, and B.I. Shklovskii. Charge density wave in two-dimensional electron liquid in magnetic field. *Physical Review Letters*, 76:499, 1996.

[51] M.M. Fogler, A.A. Koulakov, and B.I. Shklovskii. Ground state of a two-dimensional electron gas in a weak magnetic field. *Physical Review B*, 54:1853, 1996.

[52] R. Moessner and J.T. Chalker. Exact results for interacting electrons in high Landau levels. *Physical Review B*, 54:5006, 1996.

[53] M.P. Lilly, K.B. Cooper, J.P. Eisenstein, L.N. Pfeiffer, and K.W. West. Evidence for an anisotropic state of two-dimensional electrons in high Landau levels. *Physical Review Letters*, 82:394, 1999.

[54] R.R. Du, D.C. Tsui, H.L. Stormer, L.N. Pfeiffer, K.W. Baldwin, and K.W. West. Strongly anisotropic transport in higher two-dimensional Landau levels. *Solid State Commun.*, 109:389, 1999.

[55] J.P. Eisenstein. Two-dimensional electrons in excited Landau levels: evidence for new collective states. *Solid State Commun.*, 117:123, 2001.

[56] S. das Sarma and A. Pinczuk, editors. *Perspectives in quantum Hall effects.* John Wiley & Sons, 1997.

[57] A.L. Efros. Nonlinear screening and the background density of 2DEG states in magnetic field. *Solid State Commun.*, 67:1019, 1988.

[58] C.W.J. Beenakker. Edge channels for the fractional quantum Hall effect. *Physical Review Letters*, 64:216, 1990.

[59] A.M. Chang. A unified transport theory for the integral and fractional quantum Hall effects: phase boundaries, edge currents, and transmission/reflection probabilities. *Solid State Commun.*, 74:871, 1990.

[60] D.B. Chklovskii, B.I. Shklovskii, and L.I. Glazman. Electrostatics of edge channels. *Physical Review B*, 46:4026, 1992.

[61] N.B. Zhitenev, R.J. Haug, K. von Klitzing, and K. Eberl. Time-resolved measurements of transport in edge channels. *Physical Review Letters*, 71:2292, 1993.

[62] R.J.F van Haren, F.A.P. Blom, and J.H. Wolter. Direct observation of edge channels in the integer quantum Hall regime. *Physical Review Letters*, 74:1198, 1995.

[63] A.A. Shashkin, A.J. Kent, J.R. Owers-Bradley, A.J. Cross, P. Hawker, and M. Henini. Hall photovoltage imaging of the edge of a quantum Hall device. *Physical Review Letters*, 79:5114, 1997.

[64] G. Finkelstein, P.I. Glicofridis, S.H. Tessmer, R.C. Ashoori, and M.R. Melloch. Imaging of low-compressibility strips in the quantum Hall liquid. *Physical Review B*, 61:16323, 2000.

[65] Y.Y. Wei, J. Weis, K.v. Klitzing, and K. Eberl. Edge strips in the quantum Hall regime imaged by a single-electron transistor. *Physical Review Letters*, 81:1674, 1998.

[66] A. Yacoby, H.F. Hess, T.A. Fulton, L.N. Pfeiffer, and K.W. West. Electrical imaging of the quantum Hall state. *Solid State Commun.*, 111:1, 1999.

[67] M. Büttiker, Y. Imry, R. Landauer, and S. Pinhas. Generalized many-channel conductance formula with application to small rings. *Physical Review B*, 31:6207, 1985.

[68] M. Büttiker. Absence of backscattering in the quantum Hall effect in multiprobe conductors. *Physical Review B*, 38:9375, 1988.

[69] R.J. Haug. Edge-state transport and its experimental consequences in high magnetic fields. *Semicond. Sci. Technol.*, 8:131, 1993.

[70] A.H. MacDonald and P. Streda. Quantized Hall effect and edge currents. *Physical Review B*, 29:1616, 1984.

[71] D.V. Lang. In S.T. Pantelides, editor, *Deep Centers in semiconductors*. Gordon and Breach, New York, 1985.

[72] S.H. Tessmer, G. Finkelstein, P.I. Glicofridis, R.C. Ashoori, and M.R. Melloch. Modeling charge accumulation images of a quantum Hall liquid. *in preparation*.

[73] F. Stern. Self-consistent results for n-type Si inversion layers. *Physical Review B*, 5:4891, 1972.

[74] I.A. Larkin and L.S. Levitov. Spatial structure of an incompressible quantum Hall strip. *Physica E*, 6:91, 2000.

[75] A.L. Efros. Electrostatics of an inhomogeneous quantum Hall liquid. *Physical Review B*, 60:13343, 1999.

[76] A.L. Efros. Density of states of 2D electron gas and width of the plateau of IQHE. *Solid State Commun.*, 65:1281, 1988.

[77] S.W. Hwang, D.C. Tsui, and M. Shayegan. Experimental evidence for finite-width edge channels in integer and fractional quantum Hall effects. *Physical Review B*, 48:8161, 1993.

[78] S. Takaoka, K. Oto, H. Kurimoto, K. Murase, K. Gamo, and S. Nishi. Magnetocapacitance and the edge state of a two-dimensional electron system in the quantum Hall regime. *Physical Review Letters*, 72:3080, 1994.

[79] N.B. Zhitenev, M. Brodsky, R.C. Ashoori, and M.R. Melloch. New class of resonances at the edge of the two-dimensional electron gas. *Physical Review Letters*, 77:1833, 1996.

[80] A. Würtz, R. Wildfeuer, A. Lorke, E.V. Deviatov, and V.T. Dolgopolov. Separately contacted edge states: A new spectroscopic tool for the investigation of the quantum Hall effect. *cond-mat/0108186*, 2001.

[81] P.I. Glicofridis, G. Finkelstein, R.C. Ashoori, and M. Shayegan. Determination of the longitudinal resistance of incompressible strips through imaging of charge motion. *preprint*.

[82] W. Kang, H.L. Stormer, L.N. Pfeiffer, K.W. Baldwin, and K.W. West. Tunnelling between the edges of two lateral quantum Hall systems. *Nature*, 403:59, 2000.

[83] S.A. Trugman. Localization, percolation and the quantum Hall effect. *Physical Review B*, 27:7539, 1983.

[84] B. Huckenstein. Scaling theory of the integer quantum Hall effect. *Rev. Mod. Phys.*, 67:357, 1994.

[85] M.T. Woodside, C. Vale, P.L. McEuen, C. Kadow, K.D. Maranowski, and A.C. Gossard. Imaging inter-edge state scattering centers in the quantum Hall regime. *cond-mat/0002391*, 2000.

[86] S. Datta. *Electronic transport in mesoscopic systems.* Cambridge University Press, 1995.

[87] N.F. Mott and E.A. Davis. *Electronic processes in non-crystalline materials.* Oxford University Press, 1979.

[88] B.I. Shklovskii and A.L. Efros. *Electronic properties of doped semiconductors.* Springer, 1984.

[89] G. Finkelstein, P.I. Glicofridis, R.C. Ashoori, and M. Shayegan. Topographic mapping of the quantum Hall liquid using a few-electron bubble. *Science*, 289:90, 2000.

[90] M. Kastner. Artificial atoms. *Physics Today*, 46:24, 1993.

[91] R.C. Ashoori. Electrons in artificial atoms. *Nature*, 379:6564, 1996.

[92] In Hermann Grabert and Michel H. Devoret, editors, *Single Charge Tunneling: Coulomb blockade Phenomena in Nanostructures*, volume 294 of *NATO ASI Series*. Plenum Press, New York, 1992.

[93] E.B. Foxman. *Single Electron Charging and Quantum Effects in Semiconductor Nanostructures*. PhD thesis, Massachusetts Institute of Technology, 1993.

[94] N.B. Zhitenev, R.C. Ashoori, L.N. Pfeiffer, and K.W. West. Periodic and aperiodic bunching in addition spectra of quantum dots. *Physical Review Letters*, 79:2203, 1997.

[95] L.P. Kouwenhoven, C.M. Marcus, P.L. McEuen, S. Tarucha, R.M. Westervelt, and N.S. Windgreen. Electron transport in quantum dots. In L.L. Sohn, L.P. Kouwenhoven, and G. Schoen, editors, *Mesoscopic Electron Transport*, volume 345 of *NATO ASI Series*. Kluwer Academic Publishers, Dordrecht, 1997.

[96] E.B. Foxman, P.L. McEuen, U. Meirav, N.S. Wingreen, Y. Meir, P.A. Belk, N.R. Belk, M.A. Kastner, and S.J. Wind. Effects of quantum levels on transport through a Coulomb island. *Physical Review B*, 47:10020, 1993.

[97] C.W.J. Beenakker. Theory of Coulomb-blockade oscillations in the conductance of a quantum dot. *Physical Review B*, 44:1646, 1991.

[98] E. Abrahams, P.W. Anderson, D.C. Licciardello, and T.V. Ramakrishnan. Scaling theory of localization: absence of quantum diffusion in two dimensions. *Physical Review Letters*, 42:673, 1979.

[99] P.W. Anderson. Absence of diffusion in certain random lattices. *Physical Review*, 109:1492, 1958.

[100] S.V. Kravchenko, G.V. Kravchenko, J.E. Furneaux, V.M. Pudalov, and M. D'Iorio. Posssible metal-insulator transition at $B = 0$ in two dimensions. *Physical Review B*, 50:8039, 1994.

[101] S.V. Kravchenko, D. Simonian, M.P. Sarachik, W. Mason, and J.E. Furneaux. Electric field scaling at a $B = 0$ metal-insulator transition in two dimensions. *Physical Review Letters*, 77:4938, 1996.

[102] E. Wigner. On the interaction of electrons in metals. *Phys. Rev.*, 46:1002, 1934.

[103] B. Tanatar and D.M. Ceperley. Ground state of the two-dimensional electron gas. *Physical Review Letters*, 39:5005, 1989.

[104] J. Yoon, C.C. Li, D. Shahar, D.C. Tsui, and M. Shayegan. Wigner crystallization and metal-insulator transition of two-dimensional holes in GaAs at B=0. *Physical Review Letters*, 82:1744, 1996.

[105] J.A. Simmons, H.P. Wei, L.W. Engel, D.C. Tsui, and M. Shayegan. Resistance fluctuations in narrow AlGaAs/GaAs heterostructures: Direct evidence of fractional charge in the fractional quantum hall effect. *Physical Review Letters*, 63:1731, 1989.

[106] L. Saminadayar, D.C. Glattli, Y. Jin, and B. Etienne. Observation of the e/3 fractionally charged Laughlin quasiparticle. *Physical Review Letters*, 79:2526, 1997.

[107] R. de Picciotto, M. Reznikov, M. Heiblum, V. Umansky, G. Bunin, and D. Mahalu. Direct observation of a fractional charge. *Nature*, 389:162, 1997.

[108] I.J. Maasilta and V.J. Goldman. Line shape of resonant tunneling between fractional quantum Hall edges. *Physical Review B*, 55:4081, 1997.

[109] R. Williams. *Modern GaAs processing methods.* Artech House, 1990.

[110] W.Y. Han, Y. Lu, H.S. Lee, M.W. Cole, L.M. Casas, A. DeAnni, K.A. Jones, and L.W. Yang. Shallow ohmic contacts to both n- and p-GaAs. *J. Appl. Phys.*, 74:754, 1993.

[111] C.L. Chen, L.J. Mahoney, M.C. Finn, R.C. Brooks, A. Chu, and J.G. Mavroides. Low resistance Pd/Ge/Au and Ge/Pd/Au ohmic contacts to n-type GaAs. *Appl. Phys. Lett.*, 48:535, 1986.

[112] E.D. Marshall, B. Zhang, L.C. Wang, P.F. Jiao, W.X. Chen, T. Sawada, S.S. Lau, K.L. Kavanagh, and T.F. Kuech. Nonalloyed ohmic contacts to n-GaAs by solid-phase epitaxy of Ge. *J. Appl. Phys.*, 62:942, 1987.

[113] N.K. Patel, J.H. Burroughes, M.J. Tribble, E.H. Linfield, A.C. Churchill, D.A. Ritchie, and G.A.C. Jones. Independent contacting to electron layers in a double quantum well system using Pd-Ge shallow ohmic contacts. *Appl. Phys. Lett.*, 65:851, 1994.